Master's Thesis

Stratospheric injection of sulfur - Injection of accumulation mode H_2SO_4 compared to injection of SO_2

Author:

Henning Franke

Hamburg, April 22, 2020

Meteorological Institute

University of Hamburg

First supervisor: Prof. Dr. Stefan Bühler, Meteorological Institute, University of Hamburg

Second supervisor: Dr. Ulrike Niemeier, Max Planck Institute for Meteorology

Topic:

Stratospheric injection of sulfur - Injection of sulfuric acid compared to injection of sulfur dioxide

Abstract

Stratospheric Aerosol Modification (SAM) is one way of solar radiation management (SRM) and has been increasingly discussed as a potential measure against global warming. So far, most studies exploring SAM have focused on injections of sulfur dioxide (SO_2) since in volcanic eruptions this strategy has a well studied and observed natural analogue. However, multiple studies found that for SO_2 injections the efficiency of the achieved negative radiative forcing per injected mass unit of sulfur – the so-called forcing efficiency – decreases significantly with increasing injection rates. This problem is mainly related to the fact, that for increasing SO_2 injection rates also the resulting sulfate particle size increases on average. To overcome this limitation it has been recently proposed to inject sulfuric acid (H_2SO_4) instead of SO_2. It is expected that for this strategy the coagulation of sulfate aerosols would be reduced and, therefore, the resulting sulfate aerosol size distribution would have significantly more particles in the optimal size range for backscattering of incoming short wave radiation (ISR), especially for high injection rates.

To test this hypothesis and to determine the differences between injections of SO_2 and H_2SO_4, within this study the injection of both injection species has been simulated for injection rates of 5, 10, and 25 $\mathrm{Tg(S)\,yr^{-1}}$ for ten years each. In order to achieve robust results, for each injection species and rate three different injection strategies have been tested. For all simulations the general circulation model (GCM) MAECHAM5 was used, which was coupled interactively to the modal aerosol microphysical model HAM. HAM calculates all necessary aerosol microphysical processes.

The simulations show that an injection of H_2SO_4 significantly enhances the forcing efficiency compared to an injection of SO_2 for all three injection strategies and for all three injection rates. This can be traced back to the size distribution of the sulfate aerosols, which has overall smaller particles for all H_2SO_4 injections compared to their respective SO_2 injections as well as significantly more particles in the optimal size range for backscattering of ISR. For all H_2SO_4 injections the radiative forcing efficiency stays constant with increasing injection rate while for SO_2 injections it decreases with increasing injection rate. This is explained by the fact that for injections of H_2SO_4 the relative size distribution stays constant with increasing injection rate. Furthermore, it was found that modifications of the quasi-biennial oscillation (QBO) and the Brewer-Dobson Circulation (BDC) caused by the aerosol-induced stratospheric warming are independent of the injection species. However, these dynamic responses have been found to depend strongly on the injection rate and strategy.

Zusammenfassung

Das künstliche Einbringen von Sulfataerosolen in die untere Stratosphäre (SAM, von engl. *Stratospheric Aerosol Modification*) ist eine Methode des Strahlungsmanagements, die derzeit verstärkt als eine mögliche Maßnahme gegen den Klimawandel diskutiert wird. Bisher lag der Fokus der meisten Studien, die sich mit SAM beschäftigt haben, auf einer Injektion von Schwefeldioxid (SO_2), da diese Methode in Form von Vulkanausbrüchen ein bekanntes und gut beobachtetes natürliches Gegenstück hat. Diese Studien haben jedoch gezeigt, dass die Effizienz des durch die Sulfataerosole verursachten Strahlungsantriebs für eine Injektion von SO_2 mit zunehmender Injektionsrate drastisch sinkt. Dies liegt daran, dass die resultierenden Sulfatpartikel mit zunehmender Injektionsrate im Mittel immer größer werden. Aus diesem Grund wurde zuletzt vermehrt eine direkte Injektion von Schwefelsäure (H_2SO_4) als Alternative zu einer Injektion von SO_2 diskutiert. Es wird erwartet, dass diese Strategie die Koagulation von Sulfataerosolen deutlich reduziert und daher deutlich mehr Sulfatpartikel eine Größe haben werden, die für die Rückstreuung von einfallender kurzwelliger Strahlung (ISR, von engl. *incoming short wave radiation*) besonders geeignet ist. Dies gilt insbesondere für hohe Injektionsraten.

Um diese Hypothese zu testen und um die Unterschiede zwischen einer Injektion von SO_2 und einer Injektion von H_2SO_4 zu bestimmen, wurden in dieser Arbeit sowohl die Injektion von SO_2 als auch die Injektion von H_2SO_4 jeweils mit einer Injektionsrate von 5, 10, und 25 $\mathrm{Tg(S)\,yr^{-1}}$ über einen Zeitraum von zehn Jahren simuliert. Um verlässliche und robuste Ergebnisse zu erhalten, wurden für jede Injektionsrate sowohl für die Injektion von SO_2 als auch für die Injektion von H_2SO_4 drei verschiedene Injektionsstrategien getestet. Alle Simulationen wurden mit dem globalen Zirkulationsmodell (GCM, von engl. *global circulation model*) MAECHAM5 durchgeführt, welches interaktiv mit dem modalen Aerosolmikrophysik-Modell HAM gekoppelt ist. Dabei werden von HAM alle notwendigen mikrophysikalischen Prozesse berechnet.

Die Simulationen zeigen, dass eine Injektion von H_2SO_4 die Effizienz des Strahlungsantriebs im Vergleich zu einer Injektion von SO_2 für alle drei getesteten Injektionsraten und für alle drei getesteten Injektionsstrategien deutlich erhöht. Dies kann darauf zurückgeführt werden, dass die Sulfatpartikel für eine Injektion von H_2SO_4 insgesamt deutlich kleiner bleiben als für die entsprechende Injektion von SO_2. Außerdem haben für eine Injektion von H_2SO_4 deutlich mehr Partikel eine Größe, die optimal für eine effiziente Rückstreuung von ISR ist. Darüberhinaus bleibt die Effizienz des Strahlungsantriebs für alle Injektionen von H_2SO_4 mit zunehmender Injektionsrate

konstant, wohingegen sie für eine Injektion von SO_2 mit zunehmender Injektionsrate sinkt. Dies lässt sich damit erklären, dass die relative Größenverteilung der Sulfataerosole unabhängig von der Injektionsrate ist. Weiterhin zeigt diese Studie, dass sowohl die Modifizierung der quasi-zweijährigen Schwingung (QBO, von engl. *quasi-biennial oscillation*) als auch die Modifizierung der sogenannten Brewer-Dobson-Zirkulation (BDC, von engl. *Brewer-Dobson circulation*) unabhängig davon ist, ob SO_2 oder H_2SO_4 injiziert wurde. Die Modifizierung dieser Prozesse wird durch die von den Sulfataerosolen verursachte Erwärmung der unteren Stratosphäre ausgelöst und hängt vielmehr stark von der Injektionsrate und der Injektionsstrategie ab.

Contents

List of Figures

List of Tables

List of Acronyms

AMIP Atmospheric Model Intercomparison Project

AOD aerosol optical depth

BDC Brewer-Dobson Circulation

CCM chemistry-circulation model

CCS Carbon Capture and Storage

CDR Carbon Dioxide Removal

CE climate engineering

CMIP6 Coupled Model Intercomparison Project (Phase 6)

DMS dimethyl-sulfide

ESM Earth system model

EP flux Eliassen-Palm flux

SFC Earth's surface

GCM general circulation model

GeoMIP6 Geoengineering Model Intercomparison Project Phase 6

GHG greenhouse gases

IR infrared

IPCC Intergovernmental Panel on Climate Change

ISR incoming short wave radiation

LW longwave

NIR near-infrared

OCS carbonyl-sulfide

ODS ozone depleting substances

OLR outgoing longwave radiation

QBO quasi-biennial oscillation

SAM Stratospheric Aerosol Modification

SIC sea ice concentration

SMC secondary meridional circulation

SRM solar radiation management

SST sea surface temperature

SW shortwave

TEM transformed Eulerian mean

TOA top of the atmosphere

1 Introduction

Since the concentrations of atmospheric greenhouse gases (GHG) continue to increase and since it is still not conceivable when significant emission reductions start to take place, the achievement of the 2 °C warming goal from the 2015 Paris agreement is currently more than questionable. Quite the contrary, the global GHG emissions still increase making 2018 the year with the highest global CO_2 emissions on record (United Nations Environment Programme, 2019). Consequently, the available GHG emission budget to achieve the 2 °C warming goal decreases dramatically as well as the likelihood that simply decreasing anthropogenic GHG emissions would be sufficient to prevent exceeding this goal (DFG SPP 1689, 2018). As a consequence, already the fifth assessment report of the Intergovernmental Panel on Climate Change (IPCC) assumes negative emissions of carbon dioxide (CO_2) in most of its scenarios to limit global warming to 2 °C (IPCC, 2014).

Nevertheless, according to Haszeldine et al. (2018) most methods of negative emissions of CO_2 like Carbon Capture and Storage (CCS) or Carbon Dioxide Removal (CDR) are technically not feasible on a large scale at the moment and it is yet not clear when they will be. Therefore, besides negative emissions of CO_2 also the idea of SRM increasingly gains attention as a measure against anthropogenic global warming. The basic idea of SRM is to reflect parts of the incoming solar shortwave (SW) radiation back into space by enhancing the albedo of the Earth system which would reduce the net ISR at Earth's surface. The resulting surface cooling would then at least partly compensate for the surface warming due to anthropogenic GHG. Without strong emission reduction SRM technologies would have to be implemented continuously over a very long time range due to the millenial atmospheric residence time of CO_2. Consequently, they are highly questionable as a permanent and only measure against global warming, a concern which was for example presented by Pierrehumbert (2019). Nevertheless, SRM technologies could act as an important bridge technology until net negative emissions of CO_2 are reached globally. An according possible SRM scenario was for example presented in Tilmes et al. (2016).

One method of SRM which is currently widely discussed is the continuous injection of sulfur into the stratosphere, an idea which was first proposed by Budyko (1977) and which is referred to as SAM. Especially after Crutzen (2006) suggested more investigation into SAM as a potential measure against global warming, research into this method has intensified. Currently, the most studied method of SAM is the artificial injection of sulfur dioxide (SO_2) into the lower stratosphere. On this method

multiple studies with numerical models of different complexity have been performed, for example Heckendorn et al. (2009), Jones et al. (2010), Niemeier et al. (2011), Niemeier and Timmreck (2015), Laakso et al. (2016), or Tilmes et al. (2017).

An artificial injection of SO_2 basically mimics the processes taking place after a large stratospheric volcanic eruption, which builds a well studied and observed natural analogue. Consequently, following the stratospheric sulfur cycle, which is for instance outlined in Hartmann (2016) or in Feinberg et al. (2019), the artificially injected gaseous SO_2 oxidizes to gaseous sulfuric acid (H_2SO_4). This process is rather slow and has an *e*-folding time of approximately one month. Within the lower stratosphere the vapor pressure of H_2SO_4 is in principle above its saturation pressure. Therefore, the H_2SO_4 rapidly nucleates to small sulfate aerosols or condensates onto larger pre-existing background aerosols. Due to coagulation between sulfate aerosols of different size, the aerosols further grow. Ultimately, these aerosols form an artificial stratospheric aerosol layer with a size distribution depending on the injection rate and the injection strategy. This artificial aerosol layer then exerts a negative radiative forcing onto the Earth system by the backscattering of ISR, which would counteract the warming because of increasing atmospheric GHG concentrations.

However, it has been shown for instance by Heckendorn et al. (2009), English et al. (2012), or Niemeier and Timmreck (2015) that the forcing efficiency – which is the achieved radiative forcing per injected unit mass of sulfur – decreases significantly with increasing injection rates of SO_2. Following Niemeier and Timmreck (2015) this limitation arises because of the ongoing simultaneous availability of fine and coarse sulfate particles. During a continuous injection of SO_2, gaseous H_2SO_4 and freshly nucleated small particles are always available within the injection area as well as large background sulfate particles, which are distributed globally. Since the coagulation coefficient depends on the ratio of the radii between fine and coarse particles, favoring coagulation between particles with a large radii difference (Seinfeld and Pandis, 1998), most of the freshly nucleated small sulfate particles directly coagulate onto the larger background particles. An increase of the injection rate now enhances the availability of freshly nucleated small sulfate aerosols. However, most of these additional small particles also coagulate onto larger background particles rapidly, which, ultimately, leads to increasingly large sulfate particles for higher injection rates. Since larger sulfate particles sediment faster, the average stratospheric lifetime of the aerosol population decreases when increasing the injection rate (Heckendorn et al., 2009). Furthermore, the backscattering properties of the sulfate particles worsen as their radius becomes larger than $\sim 0.3\,\mu m$, which is the radius of the maximum mass specific up-scattering of solar radiation according to Dykema et al. (2016). Consequently, with increasing injection rate the radiative forcing efficiency of stratospheric SO_2 in-

jections decreases exponentially (Niemeier and Timmreck, 2015). Furthermore, this limitation of stratospheric SO_2 injections is of general nature, which means that it is independent of the injection strategy. Accordingly, it has been found for multiple injection locations, including equatorial point-like injections, extratropical point-like injections, and injections into a belt along the equator, for different injection heights, as well as for continuous and pulsed injections (Niemeier et al., 2011; Niemeier and Timmreck, 2015; Tilmes et al., 2017).

In order to overcome this limitation of SO_2 injections, other SAM approaches have been explored with the goal to avoid the loss in radiative forcing efficiency for increasing injection rates. One of these approaches is to directly inject gaseous H_2SO_4 instead of SO_2, a method which was for the first time suggested by Pierce et al. (2010). They showed that an injection of gaseous H_2SO_4 into an expanding aircraft plume could rapidly lead to the formation of an aerosol population with most of its particles in accumulation mode. A study by Benduhn et al. (2016) basically confirms these results. Since the freshly formed sulfate particles would all be roughly of the same size, it is expected that coagulation would be significantly reduced and, therefore, the sulfate particles would stay on average smaller. Additionally, sedimentation would be reduced, which would enhance the stratospheric lifetime of the sulfate particles. Due to their on average smaller size, also the backscattering ability of the sulfate particles is expected to be enhanced compared to an SO_2 injection case, which would ultimately also enhance the forcing efficiency significantly.

First studies by Pierce et al. (2010) and Vattioni et al. (2019) basically support the hypothesis that an injection of H_2SO_4 instead of SO_2 could lead to a significantly enhanced radiative forcing efficiency. Using a zonal mean 2-dimensional sectional aerosol model, Pierce et al. (2010) found that for the same sulfur injection rate a $50-60\,\%$ higher negative radiative forcing could be achieved. In experiments with a 3-dimensional version of the same model Vattioni et al. (2019) found the negative radiative forcing to be enhanced by $30-40\,\%$. Simulations by Niemeier et al. (2011) and English et al. (2012) basically support these results with different model setups by showing a clearly higher forcing efficiency for an injection of H_2SO_4 compared to a respective injection of SO_2.

Apart from these few studies the radiative and microphysical characteristics of an injection of H_2SO_4 compared to an injection of SO_2 have basically not been tested with a state-of-the-art GCM or an Earth system model (ESM). Especially the impact of the injection strategy on the aerosol population as well as its behavior for high injection rates above $10\,\mathrm{Tg(S)\,yr^{-1}}$ are currently poorly understood for an injection of H_2SO_4. Additionally, H_2SO_4 injections have never been investigated in a structured multi-model context.

The possibility of a different dynamical impact of an injection of H_2SO_4 compared to an injection of SO_2 has also not been investigated so far. For injections of SO_2, for example Heckendorn et al. (2009) and Ferraro et al. (2011) as well as many other studies observed a significant warming of the lower tropical stratosphere, which is caused by the absorption of parts of the outgoing longwave radiation (OLR) and the incoming near-infrared (NIR) radiation by the sulfate particles of the the artificial aerosol layer. This stratospheric warming then causes an acceleration of the tropical upwelling branch of the BDC, which was shown for instance by Aquila et al. (2014) and Niemeier and Schmidt (2017) for injections of SO_2. Additionally, Aquila et al. (2014) found that an injection of 2.5 Tg SO_2 in a height between 22 km and 25 km causes a prolonged westerly phase of the QBO. An injection of 5.0 Tg SO_2 into the same height range causes the QBO to be even locked in its westerly phase continuously. They attribute these modifications of the QBO to a disruption of the thermal wind balance, which is caused by the aerosol-induced stratospheric warming, and to the increased tropical upwelling, which results out of the observed acceleration of the BDC. Niemeier and Schmidt (2017) and Richter et al. (2017) basically confirmed these results with other models. Niemeier and Schmidt (2017) further investigated the impact of the observed dynamical changes onto the artificial stratospheric aerosol layer and its radiative forcing. They discovered that the breakdown of the QBO reduces the meridional transport of sulfate particles towards the extratropics. Therefore, the particles are confined to the tropics and grow on average larger, which decreases their SW backscattering potential and, ultimately, reduces the radiative forcing efficiency of the SO_2 injection (Visioni et al., 2017). Whether – and if so, how – these dynamical feedback processes might change when injecting H_2SO_4 instead of SO_2 has not been investigated so far.

Therefore, this study presents a comprehensive comparison of an injection of SO_2 and an injection of H_2SO_4 as two potential methods of SAM. In order to determine the potential differences between both injection methods, a set of 19 numerical simulations with the 3-dimensional GCM MAECHAM5, coupled interactively to the aerosol microphysical model HAM, were performed. MAECHAM5 is the middle atmosphere version of the GCM ECHAM5 (Roeckner et al., 2006; Giorgetta et al., 2006) and has a high vertical resolution, which allows the internal generation of the QBO. HAM (Stier et al., 2005) is a modal aerosol module, which simulates the evolution of the aerosol size distribution by calculating all necessary aerosol microphysical processes. Due to the internal generation of the QBO, MAECHAM5-HAM allows the simulation of the full dynamical feedback onto the sulfate aerosol size distribution, which is crucial with regards to the resulting aerosol radiative forcing.

This study is a contribution to the Geoengineering Model Intercomparison Project Phase 6 (GeoMIP6) testbed experiment *accumH2SO4*, which addresses the lack of a structured multi-model study of an artificial injection of H_2SO_4 by defining a transparent set of experiments for a direct comparison of H_2SO_4 injections and SO_2 injections (Kravitz et al., 2015; Weisenstein and Keith, 2018).

In order to give an overview of the stratospheric transport processes which determine the global distribution of the sulfate aerosols, Section 2 presents a basic description of the stratospheric circulation system including the BDC and the QBO. Furthermore, Section 2 contains a comprehensive explanation of the dynamical impact of the stratospheric warming caused by artificial sulfate aerosols. In Section 3 the setup of the model MAECHAM5-HAM as well as the performed simulations are described. The results of these simulations are presented and discussed in two sections: The impact of the injection rate and the injection strategy onto the aerosol microphysical and radiative properties of a sulfur injection is studied in Section 4, while in Section 5 the modification of the stratospheric temperature and transport processes as well as the dynamical feedback are investigated. Thereby, the SO_2 injection scenarios are always compared to their respective H_2SO_4 injection scenarios. This study ends with a discussion of the advantages and disadvantages of both injection species in Section 6 and a conclusion in Section 7.

2 Background: Stratospheric Transport of Sulfate Aerosols

The size distribution of artificial stratospheric sulfate aerosols is mainly determined by aerosol microphysical processes. However, for their spatial distribution large-scale dynamical transport processes are much more important than aerosol microphysical processes. These dynamical processes cause a zonal, meridional, and vertical transport of the sulfate aerosols away from their injection locations. While the vertical and meridional transport of sulfate aerosols within the stratosphere is dominated by the slow BDC and isentropic mixing, its zonal transport within the tropical stratosphere is dominated by the equatorial jets of the QBO.

2.1 The Brewer-Dobson circulation (BDC)

The BDC is a slow global-scale transport regime, which causes a mean advective mass transport from the tropics towards the poles within the stratosphere. It can be characterized as a single hemispheric cell with rising air in the tropics, which is then transported towards the poles in the middle stratosphere before it descends again at the poles. The characteristics of the BDC strongly depend on the season with a clearly stronger BDC in the winter hemisphere.
Despite it has no clear formal definition, the BDC is commonly described by the transformed Eulerian mean (TEM) equations, which can be derived from the zonal-mean zonal momentum and thermodynamic energy equations (Andrews and McIntyre, 1976). For a quasi-geostrophic motion on a midlatitude β-plane, Andrews et al. (1987) formulate the TEM equations as follows:

$$\frac{\partial \overline{u}}{\partial t} - f_0 \overline{v}^* = \frac{1}{\rho_0} \nabla \cdot \vec{F} + \overline{X} \tag{2.1}$$

$$\frac{\partial \overline{\Theta}}{\partial t} + \overline{w}^* \frac{\partial \Theta_0}{\partial z} = \frac{\overline{Q}}{c_\mathrm{p}} \,. \tag{2.2}$$

Equation 2.1 and Equation 2.2 are linked by the TEM form of the continuity equation:

$$\frac{\partial \overline{v}^*}{\partial y} + \frac{1}{\rho_0} \frac{\partial (\rho_0 \overline{w}^*)}{\partial z} = 0 \,. \tag{2.3}$$

Within the TEM framework given by Equations 2.1, 2.2, and 2.3, $\overline{u}$ represents the

zonal mean zonal wind speed, f_0 represents the Coriolis parameter of the respective β-plane, ρ_0 represents the density of the air, and $\overline{X}$ represents the zonal mean drag due to small-scale eddies. Further on, $\overline{\Theta}$ represents the zonal mean potential temperature, $\partial\Theta_0/\partial z$ represents the mean vertical gradient of the potential temperature, $\overline{Q}$ represents the zonal mean diabatic heating, and c_p represents the isobaric specific heat capacity. The forcing of the zonal mean circulation by eddy heat and eddy momentum fluxes is entirely described by the single term $\nabla \cdot \vec{F}$, which is the divergence of the so-called Eliassen-Palm flux (EP flux) $\vec{F}$.

The BDC itself is featured by the set of residual velocities $(\overline{v}^*, \overline{w}^*)$, which is also referred to as the residual circulation. Equation 2.1 clearly shows that in steady state conditions the BDC is driven by the dissipation of upward propagating waves, for example planetary-scale Rossby waves (Holton, 2004; Butchart, 2014). Since the wave activity is stronger in the winter hemisphere, also the BDC and its induced vertical and poleward transport of artificial sulfate particles is stronger in the winter hemisphere (Shepherd, 2000; Niemeier and Schmidt, 2017). Figure 12.8 of Holton (2004) illustrates the BDC and its transport viewed from the TEM perspective.

However, while the BDC is the main reason for the vertical transport of tracers like artificial sulfate particles in the tropics and the polar regions, it plays only a minor role for meridional transport of those tracers within the lower midlatitude stratosphere of the winter hemisphere (Butchart, 2014). The transport within this region – also called the midlatitude „surf zone“ (McIntyre and Palmer, 1984) – is dominated by rapid isentropic, quasi-horizontal transport and mixing, which is caused by the breaking of planetary waves itself (Butchart, 2014). The mixing within the surf zone creates sharp gradients of potential vorticity at its edges in the subtropics and along the winter polar vortex (Trepte and Hitchman, 1992; McIntyre et al., 1995). These gradients of potential vorticity form a transport barrier, which strongly inhibits the meridional transport of tracers out of the tropics and into the polar regions in heights between 21 km to 28 km (50 hPa to 15 hPa). Consequently, the rising branch of the BDC is rather isolated from the midlatitudes by the subtropical transport barrier, which is why it forms a natural reservoir for tracers (Trepte and Hitchman, 1992), such as artificial sulfate particles injected inside the tropics. Therefore, the rising branch of the BDC is also often referred to as the „tropical pipe“ (Plumb, 1996).

The stratospheric transport of artificial sulfate aerosols out of the tropical pipe towards the extratropics happens via two transport branches. The first transport branch is below the transport barrier. According to Niemeier and Schmidt (2017) it is the main transport branch for the majority of artificial sulfate aerosols, especially for large ones. The second transport branch is above the transport barrier. Within this

transport branch only small sulfate particles can be transported out of the tropics (Niemeier and Schmidt, 2017).
A schematic sketch of the circulation and transport patterns described in this subsection is presented in Figure 1 of Haynes and Shuckburgh (2000).

2.2 The quasi-biennial oscillation (QBO)

The QBO is a zonally symmetric oscillation of the zonal wind in the tropical stratosphere, which has an average period of approximately 28 months. It is characterized by an alternating downwelling of westerly and easterly winds from the upper stratosphere, above 5 hPa, into the tropopause region, where these wind patterns are rapidly attenuated due to friction (Baldwin et al., 2001; Holton, 2004). Consequently, the QBO winds cause a strong zonal transport of artificial sulfate aerosols in the tropical stratosphere, of which the direction depends on the QBO phase.
The first fundamental explanation of the QBO was developed by Lindzen and Holton (1968) and Holton and Lindzen (1972). According to them the QBO is basically caused by an alternating filtering of upward propagating eastward traveling equatorial Kelvin waves and westward traveling mixed Rossby-gravity waves by the lower stratospheric zonal mean flow. This alternating filtering results in an alternating dissipation of equatorial Kelvin waves and mixed Rossby-gravity waves in the upper stratosphere. Accordingly, the upper stratospheric mean flow is driven by an alternating deposition of westerly and easterly momentum, which results in an oscillation between westerly and easterly winds. Since the critical line for dissipation, which is $\overline{u} = 0\,\mathrm{m\,s^{-1}}$, moves downward due to the ongoing deposition of momentum, also the zonal wind patterns in the upper stratosphere start to propagate downward. The result of this process is the observed QBO pattern of an oscillation between downwelling westerly and easterly winds. Some more detailed explanations of the wave-mean flow interactions resulting in the QBO can be found in Baldwin et al. (2001) and Holton (2004).
Besides determining the direction of the zonal transport of artificial sulfate aerosols within the tropical stratosphere, the phase of the QBO also impacts the strength of their vertical and meridional transport, mainly by inducing secondary meridional circulation (SMC) (Plumb and Bell, 1982; Baldwin et al., 2001; Punge et al., 2009). The SMC results out of the Coriolis force, which causes an equatorward motion during westerly QBO winds and a poleward motion during easterly QBO winds. As a consequence of continuity, during QBO phases of easterly shear (westerlies in the lower stratosphere, easterlies in the upper stratosphere) the SMC shows rising motions in the tropics, while during QBO phases of westerly shear (easterlies in the

lower stratosphere, westerlies in the upper stratosphere) it shows sinking motions in the tropics (Plumb and Bell, 1982). These vertical motions within the tropics are compensated by opposite vertical motions in the subtropics. Within the tropical pipe, the vertical transport of the SMC superimposes on the general tropical upwelling of the BDC. This leads to stronger upwelling during QBO phases of easterly shear and weaker upwelling during QBO phases of westerly shear. A schematic diagram of the SMC is given in Figure 1 of Punge et al. (2009).

Also the location of the critical line for the dissipation of waves and, therefore, the location of the surf zone depends on the phase of the QBO (Shuckburgh et al., 2001; Punge et al., 2009). Thereby, the phase of the QBO also impacts the meridional transport of artificial sulfate aerosols due to isentropic mixing. Furthermore, the phase of the QBO might also have an impact on the propagation and dissipation of extratropical waves: Following Holton and Tan (1980), during easterly QBO phases planetary waves tend to dissipate more poleward in the northern hemisphere, which might cause a strong disturbance of the polar vortex (Holton-Tan mechanism). Since the polar vortex forms a poleward transport barrier for artificial sulfate aerosols, the QBO might also be able to impact the aerosol distribution in polar regions.

2.3 Impact of aerosol-induced heating on the stratospheric circulation

Sulfate aerosols have absorption bands in the infrared (IR) part of the electromagnetic wave spectrum and, therefore, absorb parts of the OLR as well as parts of the incoming NIR radiation. The absorption of IR radiation results in a heating of the lower stratosphere, which was shown for instance by Heckendorn et al. (2009) and Ferraro et al. (2011) for an injection of SO_2. The accompanied aerosol-induced stratospheric temperature anomaly modifies stratospheric dynamics in two ways: It causes a strengthening of the tropical upwelling of the BDC and it modifies the thermal wind balance.

The strengthening of the tropical upwelling can be explained using Equation 2.2. Under the assumption that during an ongoing implementation of SAM the stratospheric temperature field would reach a new steady state at some time, Equation 2.2 then simplifies to

$$\overline{w}^* \frac{\partial \Theta_0}{\partial z} = \frac{\overline{Q}}{c_\mathrm{p}} \,. \tag{2.4}$$

In the absence of significant changes of the stratospheric stratification $\partial\Theta_0/\partial z$, an

increase of diabatic heating $\overline{Q}$ consequently causes an increase of the residual vertical velocity $\overline{w}^*$, considered the very stable stratification of the stratosphere ($\partial\Theta_0/\partial z > 0\,\mathrm{K\,m^{-1}}$). Due to continuity (see Equation 2.3) this increase of tropical upwelling extends well above the heated aerosol layer and speeds up the whole BDC. Accordingly, an increase of $\overline{w}^*$ and the BDC has been found in multiple studies of SAM, for example in Niemeier et al. (2011), Aquila et al. (2014), Niemeier and Schmidt (2017), Richter et al. (2017), or Tilmes et al. (2018), as well as in studies of large volcanic eruptions, for example in Niemeier et al. (2009) or Aquila et al. (2012).
The second consequence of an aerosol-induced stratospheric heating is the disruption of the thermal wind balance. This is accompanied by a modification of the QBO winds, which are approximately in thermal wind balance with the stratospheric temperature field within the tropics. The thermal wind balance links the vertical wind shear to the meridional temperature gradient and formulates as

$$\frac{\partial\overline{u}}{\partial z} = -\frac{R}{H\beta y}\frac{\partial\overline{T}}{\partial y} \tag{2.5}$$

for an equatorial β-plane (Holton, 2004). In Equation 2.5 $\overline{u}$ denotes the zonal mean wind speed and $\overline{T}$ denotes the zonal mean temperature. Furthermore, Equation 2.5 contains three constants: The gas constant for dry air R, the scale height H, and the meridional gradient of the Coriolis parameter β at the equator. Assuming equatorial symmetry of the zonal mean temperature $\overline{T}$, one can set $\partial\overline{T}/\partial y = 0\,\mathrm{K\,m^{-1}}$ at the equator ($y = 0\,\mathrm{m}$) and apply the rule of L'Hospital (Holton, 2004). As a result, the thermal wind balance at the equator can be written as

$$\frac{\partial\overline{u}}{\partial z} = -\frac{R}{H\beta}\frac{\partial^2 T}{\partial y^2}\,. \tag{2.6}$$

According to Baldwin et al. (2001) Equation 2.6 can be further approximated for QBO variations centered at the equator with a meridional scale L:

$$\frac{\partial\overline{u}}{\partial z} \sim \frac{R}{H\beta}\frac{T}{L^2}\,. \tag{2.7}$$

Following Equation 2.7, an aerosol-induced positive temperature anomaly in the lower stratosphere results in an increased westerly shear within the heated aerosol layer. This results in an additional westerly component of the zonal wind above the heated aerosol layer, which prolongs the westerly phase of the QBO in the lower stratosphere (Aquila et al., 2014). For high injection rates Aquila et al. (2014) and Niemeier and

Schmidt (2017) found the QBO to be even locked in a constant westerly phase in the lower stratosphere.

These disturbances of the QBO are supported by an increased residual vertical advection of zonal momentum ($-\overline{w}^* \, \partial\overline{u}/\partial z$) by the BDC. Since the residual vertical velocity $\overline{w}^*$ increases due to the aerosol-induced heating of the lower stratosphere, also the upward advection of the now predominantly westerly momentum in the lower stratosphere increases. According to Aquila et al. (2014) the resulting stronger eastward forcing in the shear zone might (over-)compensate the westward forcing applied by the dissipation of gravity waves, which in the absence of SAM causes the downward propagation of the QBO. Therefore, depending on the strength of the stratospheric heating anomaly, the downwelling of the QBO easterly winds is significantly slowed down or even completely stopped. Accordingly, also the SMC, which accompanies the QBO, would be locked in the corresponding state in which it strengthens the BDC and the tropical upwelling.

As a result of the modification of the BDC and the QBO, also the transport patterns of the sulfate aerosols are modified. For injections of SO_2, Niemeier and Schmidt (2017) found that the modified transport patterns lead to a stronger tropical confinement of the aerosol layer. This can be explained by the strengthening of the BDC and the SMC, which causes a stronger equatorward transport in the lower stratosphere resulting in a reduced transport towards the extratropics. Furthermore, the increased tropical upwelling within the tropical pipe causes a higher vertical extent of the aerosol layer within the tropics. Niemeier and Schmidt (2017) also showed that meridional shifts of the surf zone might cause interhemispheric differences in the sulfate aerosol distribution. An overview of potential dynamical feedback mechanisms can be found in Visioni et al. (2017).

3 Setup of the Model and the Simulations

The simulations of this study were performed with the 3-dimensional GCM MAECHAM5, which was interactively coupled to the aerosol microphysical model HAM. The coupled model system MAECHAM5-HAM has been used in multiple SAM studies before, for example Niemeier et al. (2011), Niemeier and Timmreck (2015) or Laakso et al. (2016). Apart from the horizontal and vertical resolution, the model settings used in those studies are identical to the ones used in this study. The setup of MAECHAM5-HAM within this study is exactly the same as in Niemeier and Schmidt (2017).

3.1 General circulation model MAECHAM5

The GCM MAECHAM5 is the middle atmosphere version of the GCM ECHAM5 (Roeckner et al., 2003; Giorgetta et al., 2006; Roeckner et al., 2006). ECHAM5 is a spectral GCM, which simulates the evolution of atmospheric dynamics by numerically solving prognostic equations for temperature, surface pressure, vorticity, and divergence in terms of spherical harmonics. The different phases of water as well as tracers are transported within the model using a flux form semi-Lagrangian transport scheme (Lin and Rood, 1996). Details on ECHAM5 can be found in Roeckner et al. (2003).

Compared to ECHAM5, its middle atmosphere version MAECHAM5 has a larger vertical domain which extends from the surface up to 0.01 hPa while being resolved by 90 sigma-p levels. Additionally, MAECHAM5 also accounts for the momentum flux deposition of unresolved gravity waves originating from the troposphere via a parametrization. Therefore, MAECHAM5 internally generates a QBO in the tropical stratosphere, which, does not have to be prescribed to the model externally (Giorgetta et al., 2006).

For this study, MAECHAM5 was used with a spectral truncation at wave number 42 (T42) resulting in a horizontal grid with 64×128 grid boxes, which corresponds to a size of $2.8125° \times 2.8125°$ per grid box. The time step used within all simulations was 600 s in order to ensure compliance with the Courant-Friedrichs-Lewy criterion throughout the whole simulation.

3.2 Aerosol microphysical model HAM

HAM (Hamburg Aerosol Model) is a modal aerosol microphysical model, which is based on the microphysical core M7 developed by Vignati et al. (2004). It describes the size distribution of the whole aerosol population by seven log-normal modes; three insoluble and four soluble ones. However, since H_2SO_4 dissolves in water easily, within HAM the sulfate aerosol size distribution $n(\ln r)$ is entirely described by a superposition of the four soluble log-normal modes i, which are the nucleation mode (NS-SO_4), the Aitken mode (KS-SO_4), the accumulation mode (AS-SO_4), and the coarse mode (CS-SO_4):

$$n(\ln r) = \sum_{i=1}^{N=4} \frac{N_\mathrm{i}}{\sqrt{2\pi}\ln\sigma_\mathrm{i}} \exp\left(-\frac{(\ln r - \ln \overline{r}_\mathrm{i})^2}{2\ln^2\sigma_\mathrm{i}}\right). \tag{3.1}$$

In Equation 3.1, N_i represents the total sulfate aerosol number of mode i, σ_i represents the standard deviation of mode i, and $\overline{r}_\mathrm{i}$ represents the number median radius of the sulfate aerosols in mode i. Consequently, each mode of the sulfate aerosol spectrum can be fully described by these three parameters, which are the so-called first three moments of the respective mode. Since in HAM the standard deviation σ_i of each mode i is set to a constant value, this reduces to just two parameters: The sulfate aerosol number N_i and the number median radius $\overline{r}_\mathrm{i}$ of the sulfate aerosols in the respective mode i (Stier et al., 2005).

Assuming the sulfate aerosols are of spherical shape and have a constant density ρ, according to Niemeier (personal communication, 2019) the number median radius $\overline{r}_\mathrm{i}$ of the sulfate aerosols in mode i can be derived from its total sulfate aerosol number N_i and its total sulfate aerosol mass M_i by

$$\overline{r}_\mathrm{i} = \sqrt[3]{\frac{3}{4\,\pi}\,\frac{M_\mathrm{i}}{N_\mathrm{i}}\,\frac{1}{\rho}}\;\frac{1}{\exp\left(1.5\ln^2\sigma_\mathrm{i}\right)}. \tag{3.2}$$

Consequently, the evolution of the whole sulfate aerosol size distribution can be fully simulated by calculating the evolution of the total sulfate aerosol number N_i and the total sulfate aerosol mass M_i of each mode i.

The respective changes of the total sulfate aerosol number and mass of all four modes at a given location due do aerosol microphysical processes are calculated by HAM. Aerosol microphysical processes included in HAM are the sulfate aerosol formation via nucleation, accumulation, condensation, and coagulation as well as the sulfate aerosol depletion via sedimentation and deposition (Stier et al., 2005; Niemeier and Timmreck, 2015). The modification of the sulfate aerosol number and the sulfate

aerosol mass of a given mode also modifies its number median radius following Equation 3.2. Therefore, after each timestep HAM performs a reallocation of the sulfate aerosol number and mass. This means that particles with a larger radius than the upper size limit of a given mode i are transferred to the next larger mode $i + 1$ in order to stay within the modal size ranges (Vignati et al., 2004). An overview of the size ranges for the particle radius of all four soluble modes is given in Table 3.1.

Apart from aerosol microphysical processes, the total sulfate aerosol number and mass of all four modes at a given location can be also changed by large-scale dynamical transport processes. This type of changes is calculated by MAECHAM5 by including the total sulfate aerosol number and the total sulfate aerosol mass of all four modes as passive tracers. Consequently, MAECHAM5-HAM is able to prognosticate the entire evolution of the sulfate aerosol size distribution due to aerosol microphysical processes and dynamical transport processes (Stier et al., 2005).

Since HAM was initially designed for tropospheric aerosol studies, its default setup is not representative, and hence not applicable for studying stratospheric sulfate aerosols. Therefore, in this study HAM is used in its SAM setup described in Niemeier and Timmreck (2015), which is in accordance with box-model studies from Kokkola et al. (2009). In this setup the standard deviation of the nucleation mode, the Aitken mode, and the accumulation mode is kept at its respective default value of $\sigma = 1.59$. The standard deviation of the coarse mode is reduced from its default value of $\sigma = 2.0$ to $\sigma = 1.2$ in order to produce size distributions which fit to those produced by the more accurate sectional aerosol model of Heckendorn et al. (2009). Additionally, some further minor changes have been applied to the microphysical core of HAM in order to use it for SAM studies, which can be found in Niemeier et al. (2009) and Niemeier and Timmreck (2015).

The sulfur chemistry scheme used in this setup of HAM is a simple stratospheric sulfur chemistry which is applied at and above the tropopause (Timmreck, 2001; Hommel and Graf, 2011). It has been used in several previous studies, for example in Niemeier et al. (2009), Niemeier and Timmreck (2015), or Niemeier and Schmidt (2017), where also more details on it can be found. This scheme uses prescribed monthly oxidant fields of OH, NO_2, and O_3 and prescribed photolysis rates of OCS, H_2SO_4, SO_2, SO_3, and O_3 (Stier et al., 2005). Therefore, the impact of SAM onto stratospheric ozone can not be simulated within MAECHAM5-HAM and results of earlier studies, which found that ozone depletion will be enhanced due to SAM (Heckendorn et al., 2009; Tilmes et al., 2018; Vattioni et al., 2019), can't be reproduced. This also includes possible ozone feedback mechanisms.

Apart from the injected SO_2 or H_2SO_4 only some natural sulfur emissions are taken into account. These include natural dimethyl-sulfide (DMS) and carbonyl-sulfide

Table 3.1: Radius size ranges of the four soluble modes of HAM.

NS-SO_4	$0.0005\,\mu m < r \leq 0.005\,\mu m$
KS-SO_4	$0.005\,\mu m < r \leq 0.05\,\mu m$
AS-SO_4	$0.05\,\mu m < r \leq 0.2\,\mu m$
CS-SO_4	$0.2\,\mu m < r$

(OCS) emission, with OCS concentrations being prescribed at the surface and transported throughout the model. Natural sulfur emissions from biomass burning and wildfires as well as from continuous and explosive volcanic eruptions are not taken into account.

Due to its coarse horizontal resolution, MAECHAM5-HAM is not able to simulate the rapid initial formation of AS-SO_4 particles within an aircraft plume in a H_2SO_4 injection case (Weisenstein and Keith, 2018). This problem has to be modeled by a plume dispersion model, which was done by Pierce et al. (2010) and Benduhn et al. (2016). They showed that the resulting aerosol size distribution could mainly contain particles with a radius between $0.095 - 0.15\,\mu m$ when the plume has expanded sufficiently (Weisenstein and Keith, 2018). Subsequently, the resulting aerosol size distribution of the plume dispersion model can be injected into the GCM with a coupled aerosol microphysical model to simulate the global dispersion as well as the radiative forcing of the sulfate aerosols. Therefore, within this study the H_2SO_4 injection cases were modeled as a direct injection of an AS-SO_4 population with a mode radius of $0.075\,\mu m$ and a standard deviation of 1.59. These values are the default values for a primary AS-SO_4 emission within HAM. The mode radius of $0.075\,\mu m$ is slightly below the values suggested by Pierce et al. (2010) and Benduhn et al. (2016). Nevertheless, since there is still considerable uncertainty in the mode radius that the AS-SO_4 potentially will have, the used value of $0.075\,\mu m$ is reasonable and represents the lower edge within the range of potential mode radii.

To enable a direct injection of AS-SO_4, HAM had to be modified. In contrast to injections of a molecular gas like SO_2, where just the total mass of injected SO_2 in a certain period has to be prescribed, for an injection of AS-SO_4 also the total number of injected particles in this period has to be prescribed. Given the number median radius of the injected AS-SO_4, which is $\overline{r} = 0.075\,\mu m$, and the standard deviation of the accumulation mode, which is $\sigma = 1.59$, the total number injection rate $\dot{N}$ of AS-SO_4 particles can be calculated out of the total mass injection rate $\dot{M}$ of the injected AS-SO_4 as

$$\dot{N} = \frac{3}{4\,\pi}\,\frac{\dot{M}}{\rho}\,\frac{1}{\sqrt[3]{\overline{r}\exp\left(1.5\ln^2\sigma\right)}}\,, \tag{3.3}$$

which is simply a rearrangement of Equation 3.2. The density of the aerosol was prescribed to $\rho = 1841\,\mathrm{kg\,m^{-3}}$, which is the density of H_2SO_4 used in HAM.
A detailed overview of the microphysics of HAM can be found in Vignati et al. (2004).

3.3 Coupling of MAECHAM5 and HAM

The GCM MAECHAM5 and the aerosol microphysical model HAM are coupled interactively to the 3-dimensional model system MAECHAM5-HAM. The coupling between both models is performed via multiple interfaces, for example via radiation, advection, atmospheric water, or rain. Therefore, it enables the simulation of dynamical feedback processes of SAM.
Via the coupling of HAM onto the radiation scheme of MAECHAM5, the radiative properties of the stratospheric sulfate aerosol layer are recognized in the radiation scheme of MAECHAM5. That is important to simulate dynamical feedback processes. Due to the absorption of OLR and incoming solar NIR radiation, sulfate aerosols cause a heating of the lower stratosphere, which modifies dynamical transport processes within the stratosphere (Aquila et al., 2014; Niemeier and Schmidt, 2017). Consequently, the stratospheric sulfate aerosol layer is able to modify the stratospheric circulation within the coupled MAECHAM5-HAM.
The coupling of HAM onto the radiation scheme of MAECHAM5 also allows for an accurate calculation of the SW as well as the longwave (LW) radiative forcing exerted by the sulfate aerosol layer. The aerosol radiative forcing is calculated by a so-called double-radiation call. This means that the sulfate aerosol forcing is calculated as the difference between the radiative forcing obtained in a simulation with radiative coupling of HAM on MAECHAM5 and the radiative forcing obtained in a simulation without a radiative coupling between of HAM on MAECHAM5.
The coupling of HAM onto MAECHAM5 via the advection scheme of MAECHAM5 allows for an interactive transport of artificial sulfate aerosols. Since this transport of artificial sulfate aerosols may change their local availability, it also modifies local microphysical processes. Therefore, also local sulfate aerosol size distributions are influenced by the dynamic transport of the sulfate aerosols.

3.4 Performance of MAECHAM5-HAM

Since SAM has never been performed in reality so far, a direct evaluation of SAM results of MAECHAM5-HAM against potential measurements is not possible. However, MAECHAM5-HAM has been evaluated against several measurements after the eruption of the tropical volcano Mt. Pinatubo in June 1991 by Niemeier et al. (2009)

and Toohey et al. (2011) to ensure a realistic simulation of the stratospheric sulfate aerosol layer. Both studies used a volcanic setup of HAM, which is slightly different to the SAM setup of HAM as it has no coarse mode and a smaller standard deviation in the accumulation mode ($\sigma = 1.2$ instead of $\sigma = 1.59$). This is due to the fact that the sulfur injection differs significantly between a short and strong volcanic eruption and a SAM injection, which is continuous and weak. Niemeier et al. (2009) and Toohey et al. (2011) found that the modeled evolution of aerosol properties as well as the modeled evolution of dynamical and radiative features after the eruption shows a rather good agreement with related measurement data from Lidar and satellite measurements. For the particle size of the sulfate aerosols, the top of the atmosphere (TOA) radiation, and the timing and location of the aerosol optical depth (AOD) peak value the model results match the measurements overall well and MAECHAM5-HAM has not shown a systematic bias for these parameters.

However, Niemeier et al. (2009) found that the poleward transport of the AOD is overestimated by $10\,\% - 20\,\%$ in MAECHAM5-HAM compared to satellite measurements. This overestimation of aerosol transport out of the tropical eruption region, consequently, leads to an underestimation of tropical aerosol concentrations six months after the eruption (Niemeier et al., 2009). Nevertheless, despite the slight overestimation of the poleward transport, the studies by Niemeier et al. (2009) and Toohey et al. (2011) have shown that MAECHAM5-HAM delivers reliable results in simulating volcanic eruptions which match the observations overall well. Therefore, also for simulations of SAM one could expect reliable results by MAECHAM5-HAM, despite the slightly different HAM setup used by Niemeier et al. (2009) and Toohey et al. (2011) compared to the one used in this study.

Nevertheless, when interpreting the results of MAECHAM5-HAM, one should consider its modal setup carefully since it may limit their significance as well as their comparability. HAM resolves the size distribution of soluble sulfate aerosols by a superposition of four log-normal modes (see Eq. 3.1). Besides this modal approach, the sulfate aerosol size distribution can also be resolved by a discretization into several distinct size bins, which is done in so-called sectional aerosol microphysical models. Compared to detailed sectional aerosol microphysical models modal aerosol microphysical models like HAM show an overall worse performance in resolving the size distribution accurately. This may result in significant differences of the calculated stratospheric aerosol mass, which has been shown for example by Weisenstein et al. (2007), who compared modal and sectional models for binary sulfuric acid-water aerosols in a global 2-dimensional model. They found that the simulated aerosol mass of the modal model can be different from the one simulated by a detailed 150-bin sectional model by up to $40\,\%$ at a height of $30\,\mathrm{km}$. They account this large

difference mainly to differences in the calculated sedimentation velocity resulting out of the different resolutions of the aerosol size distribution. Since the overall strength of sedimentation especially depends on the size of large sulfate particles, they argue that σ of the largest log-normal mode is a crucial parameter for modelling a correct stratospheric sulfate mass within a modal model.

The results of Weisenstein et al. (2007) have been basically confirmed for HAM in a study by Kokkola et al. (2009), in which they compared HAM with three sectional aerosol models in the framework of ECHAM5. For stratospheric conditions they also found that the usage of HAM results in a too low stratospheric sulfate mass compared to the sectional models. In order to at least partly mitigate the unrealistically strong sedimentation, σ of CS-SO_4 was reduced from $\sigma = 2$ to $\sigma = 1.2$ within this study. However, the simulated stratospheric sulfate mass within this study may be too low. Also the low horizontal resolution of MAECHAM5 of T42 tends to result in a rather low stratospheric sulfate mass. As shown by Niemeier et al. (2020), an increase of the horizontal resolution within MAECHAM5 from T42 to T63 – keeping all else equal – results in a significantly larger stratospheric sulfate mass as well as in a stronger tropical confinement of the sulfate aerosols. This may be a consequence of weaker numerical diffusion when using a higher horizontal resolution. Consequently, when comparing the results of this study to the results of studies, which use models with a different horizontal and vertical resolution, it should be considered that numerical diffusion can partly account for possible differences.

3.5 Setup of performed simulations

In this study, in total 18 different numerical simulations of SAM experiments have been performed in order to compare a stratospheric injection of SO2 to a stratospheric injection of H2SO4, modeled as an injection of an AM-SO_4 population (see Section 3.2). The experimental setup of these simulations is in accordance with the proposal of the GeoMIP6 testbed experiment *accumH2SO4* (Weisenstein and Keith, 2018).

Within this study, three different injection strategies have been tested for both injection species: An injection into one single grid box centered at 1.4° N, 180° E, from now on referred to as *point*, a simulatenous injection into two grid boxes centered at 29.3° N, 180° E and 29.3° S, 180° E, from now on referred to as *2point*, and a injection into a zonally symmetric belt from 30° N to 30° S along the equator, from now on referred to as *region*. Figure 3.1 shows the injection locations of the three different injection strategies. While the 2point and region injections are mandatory injection strategies within *accumH2SO4*, the point injection strategy has been chosen addi-

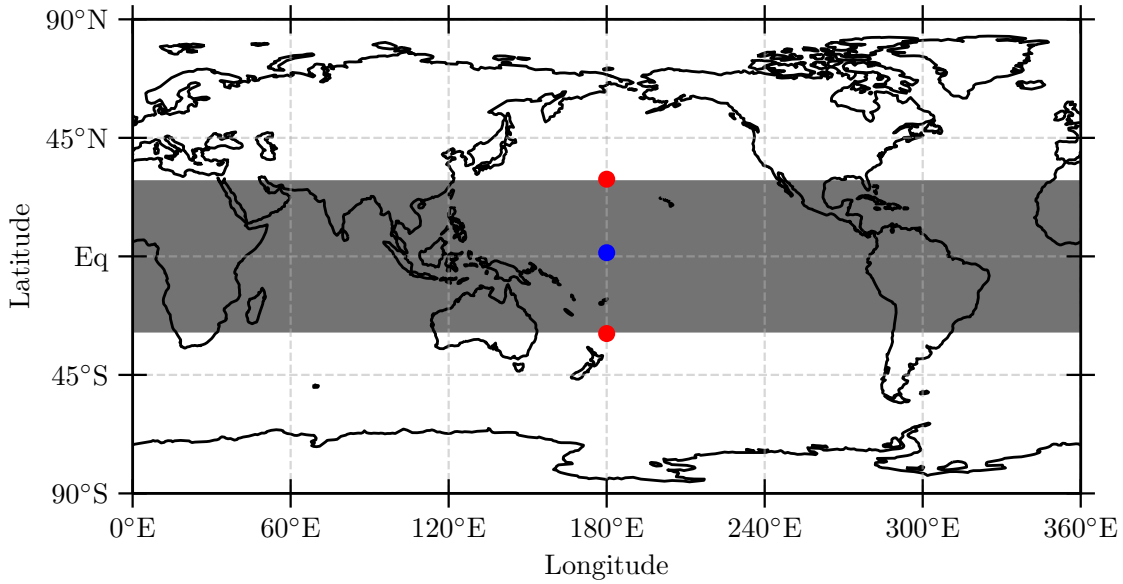

Figure 3.1: Injection locations of the different injection strategies. The blue point marks the injection location of the point injections (point-so2 and point-so4), which is a single grid box centered at 1.4° N 180° E. The red points mark the injection locations of the 2point injections (2point-so2 and 2point-so4), which are two grid boxes centered at 29.3° N 180° E and 29.3° S 180° E. The greyish bar marks the injection location of the region injections (region-so2 and region-so4), which is a belt along the equator ranging from 30° N 180° E to 30° S 180° E.

tionally in this study to enable the comparison with earlier studies, which have often focused on equatorial point-like injections of SO_2.

For all injection strategies, the SO_2 and the H_2SO_4 were injected continuously with a constant injection rate. They were injected into three adjacent model layers which are centered at 68.02 hPa, 62.32 hPa and 57.14 hPa. This corresponds to an injection height of approximately 18 km to 20 km according to the 1976 U.S. standard atmosphere (National Geophysical Data Center, 1992).

For both investigated injection species and all tested injection strategies, simulations with three different injection rates of 5, 10, and 25 $\mathrm{Tg(S)\,yr^{-1}}$ have been performed. The denomination of the SAM experiments within this study follows the scheme (*injection strategy*)-(*injection species*)-(*injection rate*). An overview of all performed simulations, their setup, and their denomination can be found in Table 3.2.

Besides the SAM simulations, also one control simulation without any SAM was performed, which is termed *contr-000*. *Contr-000* serves as a reference and represents the state of the atmosphere without artificial SAM. Therefore, all anomalies presented in this studies are relative to *contr-000*. Furthermore, all simulations including *contr-000* were performed for a period of ten years. However, it takes a few years until the

artificial stratospheric sulfate layer has reached equilibrium. Therefore, the results presented in this study have been averaged only over the last six years of the respective simulation.

Also the boundary conditions of all performed simulations within this study have been set in accordance with the proposal of *accumH2SO4* (Weisenstein and Keith, 2018). The greenhouse gas concentrations are taken from the SSP5-8.5 scenario of ScenarioMIP (O'Neill et al., 2016) for the year 2040, resulting in a CO_2 concentration of $c\,(CO_2) = 494.57\,\text{ppm}$, a CH_4 concentration of $c\,(CH_4) = 2.19\,\text{ppm}$, and a NO_2 concentration of $c\,(NO_2) = 0.35\,\text{ppm}$. The concentrations of ozone depleting substances (ODS) have also been prescribed to 2040 ScenarioMIP levels, resulting in a CFC-11 concentration of $c\,(\text{CFC-11}) = 165.83\,\text{ppt}$ and a CFC-12 concentration of $c\,(\text{CFC-12}) = 408.97\,\text{ppt}$.

Within the simulations of this study MAECHAM5-HAM was neither coupled to an ocean model nor a landbiosphere model. Therefore, only the atmospheric response to SAM is simulated within the simulations of this study, while the response of the ocean and the vegetation to SAM is not simulated. The lack of an ocean model further implies that the sea surface temperature (SST) and the sea ice concentration (SIC) had to be prescribed to MAECHAM5 as boundary conditions and were fixed throughout the simulations. According to the proposal of *accumH2SO4*, in all simulations the SST and the SIC were set to monthly climatological values of the period 1988 to 2007 out of the SST data set from the Atmospheric Model Intercomparison Project (AMIP). In order to start all simulations with a balanced and consistent state of the atmosphere which has adjusted to the described boundary conditions, all simulations including *contr-000* have been initialized with the output of a 10-year spin up simulation, which was performed without any SAM.

Table 3.2: Setup of all performed simulations. The X in the simulation name denotes the injection rate.

Experiment	**Injection species**	**Injection rate ($\mathbf{Tg(S)\,yr^{-1}}$)**	**Injection location**
contr-000	-	-	-
point-so2-X	SO_2	5, 10, 25	Grid box centered at 1.4° N 180° E
2point-so2-X	SO_2	5, 10, 25	Grid box centered at 29.3° N 180° E and grid box centered at 29.3° S 180° E
region-so2-X	SO_2	5, 10, 25	30° N to 30° S, all longitudes
point-so4-X	H_2SO_4 as AS-SO_4	5, 10, 25	Grid box centered at 1.4° N 180° E
2point-so4-X	H_2SO_4 as AS-SO_4	5, 10, 25	Grid box centered at 29.3° N 180° E and grid box centered at 29.3° S 180° E
region-so4-X	H_2SO_4 as AS-SO_4	5, 10, 25	30° N to 30° S, all longitudes

4 Comparison of Aerosol Microphysical and Radiative Properties

Within this section the radiative forcing exerted by the artificial stratospheric aerosol layer as well as its causes are compared for an injection of SO_2 and an injection of H_2SO_4, modeled as an injection of an AS-SO_4 population. The total radiative forcing exerted by stratospheric sulfate aerosols depends mainly on two things: Their size distribution and their vertically integrated stratospheric mass, which is often referred to as the sulfate burden M. However, also the sulfate burden itself depends on the sulfate aerosol size distribution significantly via sedimentation.
The sulfate modes which are able to backscatter incoming SW radiation efficiently within HAM are AS-SO_4 and CS-SO_4, while NS-SO_4 and KS-SO_4 particles are too small for efficient backscattering of solar radiation (Dykema et al., 2016). Additionally, the stratospheric mass of NS-SO_4 and KS-SO_4 is neglectable compared to the stratospheric mass of SO_2, AS-SO_4, and CS-SO_4. Therefore, within this study the term *sulfate burden* refers to the sum of the radiative active AS-SO_4 burden and CS-SO_4 burden. The sum of the AS-SO_4 burden, the CS-SO_4 burden, and the SO_2 burden is termed the *sulfur burden*. An overview of the burden of all considered stratospheric sulfur species for all SAM experiments performed in this study is given in Table 4.1.
The impact of the injection species – SO_2 or H_2SO_4 – onto the stratospheric sulfate burden as well as the net radiative forcing exerted by the aerosols is examined in Section 4.1. In Section 4.2 the aerosol microphysical and radiative properties of an injection of SO_2 and an injection of H_2SO_4 are compared with respect to an increasing injection rate, while in Section 4.3 they are compared with respect to a varying injection strategy.

4.1 Impact of injection species

Stratospheric sulfur basically exist in the form of gaseous SO_2 and in the form of sulfate aerosols of different sizes. Since SO_2 does not backscatter incoming SW radiation, it is desirable to keep the SO_2 fraction of artificial stratospheric sulfur as small as possible during a performance of SAM. However, when injecting SO_2 a constant fraction of the stratospheric sulfur remains in the form of SO_2 for all three injection strategies as visible in Figure 4.1. This fraction is independent of the injection rate: For the point injections, approximately 15 % of the stratospheric sulfur remains in

Table 4.1: Global artificial burden of different sulfur species in Tg(S) for all SAM experiments. Values in brackets represent the respective burden relative to the global artificial sulfur burden, which is denoted by its chemical symbol S and corresponds to 100 %.

Experiment	SO_2	AS-SO_4	CS-SO_4	SO_4	S
point-so2-5	0.6 (16.2 %)	0.5 (13.5 %)	2.6 (70.3 %)	3.1 (83.8 %)	3.7
point-so2-10	1.1 (14.9 %)	0.5 (6.7 %)	5.8 (78.4 %)	6.3 (85.1 %)	7.4
point-so2-25	3.0 (15.9 %)	0.5 (2.7 %)	15.3 (81.4 %)	15.8 (84.1 %)	18.8
point-so4-5	0.0 (0.0 %)	0.7 (13.7 %)	4.3 (86.3 %)	5.1 (100.0 %)	5.1
point-so4-10	0.0 (0.0 %)	0.9 (8.0 %)	10.4 (82.0 %)	11.3 (100.0 %)	11.3
point-so4-25	0.0 (0.0 %)	1.1 (3.1 %)	34.7 (96.9 %)	35.8 (100.0 %)	35.8
2point-so2-5	0.8 (21.6 %)	0.4 (10.8 %)	2.5 (67.6 %)	2.9 (78.4 %)	3.7
2point-so2-10	1.6 (21.9 %)	0.5 (6.8 %)	5.2 (71.3 %)	5.7 (78.1 %)	7.3
2point-so2-25	4.1 (22.9 %)	0.5 (2.8 %)	13.3 (74.3 %)	13.8 (77.1 %)	17.9
2point-so4-5	0.0 (0.0 %)	0.9 (21.4 %)	3.3 (78.6 %)	4.2 (100.0 %)	4.2
2point-so4-10	0.0 (0.0 %)	1.1 (12.2 %)	7.9 (87.8 %)	9.0 (100.0 %)	9.0
2point-so4-25	0.0 (0.0 %)	1.2 (4.6 %)	24.7 (95.4 %)	25.9 (100.0 %)	25.9
region-so2-5	0.7 (20.6 %)	0.2 (5.9 %)	2.5 (73.5 %)	2.7 (79.4 %)	3.4
region-so2-10	1.3 (20.0 %)	0.3 (4.6 %)	4.9 (85.4 %)	5.2 (80.0 %)	6.5
region-so2-25	3.4 (22.3 %)	0.2 (1.3 %)	12.1 (76.4 %)	12.3 (77.7 %)	15.7
region-so4-5	0.0 (0.0 %)	1.6 (34.8 %)	3.0 (65.2 %)	4.6 (100.0 %)	4.6
region-so4-10	0.0 (0.0 %)	2.1 (21.1 %)	7.8 (78.9 %)	9.9 (100.0 %)	9.9
region-so4-25	0.0 (0.0 %)	3.2 (11.1 %)	25.7 (88.9 %)	28.9 (100.0 %)	28.9

the form of SO_2, while for the other two injection strategies it is slightly above 20 %. In contrast, when injecting H_2SO_4 no artificial SO_2 is added to the stratosphere and consequently all artificial stratospheric sulfur exists in the form of radiative active sulfate, independent of injection rate and strategy (Tab. 4.1).

The absolute global artificial sulfate burden M_{SO4} is also higher for an injection of H_2SO_4 than for an injection of SO_2 (Fig. 4.2 a). It holds true for all three tested injection rates and all three tested injection strategies. For an injection rate of 5 Tg(S) yr^{-1} the global sulfate burden is approximately 1.5 times higher for an injection of H_2SO_4 than for an injection of SO_2. For an injection rate of 25 Tg(S) yr^{-1} it is even up to approximately 2.4 times larger.

The significantly lower global sulfate burden, which results out of an injection of SO_2, can only be partly attributed to the remaining of some sulfur in the form of SO_2. The main reason for the significantly lower global sulfate burden are differences in the aerosol size. As indicated by the particle number density in Figure 4.3, the AS-

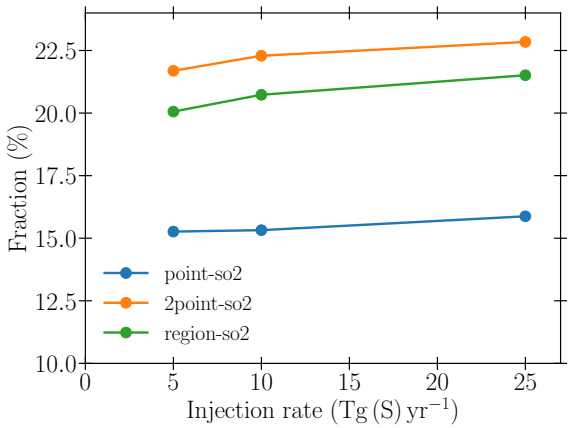

Figure 4.1: Fraction of the global artificial sulfur burden which remains in the form of SO_2 as a function of injection rate. Only experiments with an injection of SO_2 are shown.

SO_4 and CS-SO_4 particles stay on average clearly smaller for an injection of H_2SO_4 than for the corresponding injection of SO_2. Smaller aerosol particles have a lower mass compared to larger ones, which is why they also sediment slower (see Seinfeld and Pandis (1998), eq. 8.42). Accordingly, the sedimentation velocity v_t is clearly smaller, i.e. less negative, when injecting H_2SO_4 instead of SO_2 (Fig. 4.4). Slower sedimentation results in a longer stratospheric lifetime of an aerosol particle and, consequently, in a higher global aerosol burden. This explains the observed differences of the global sulfate burden between an injection of H_2SO_4 and an injection of SO_2.

The on average smaller sulfate particle size, which results out of an injection of H_2SO_4 compared to an injection of SO_2, is a general feature of an injection of H_2SO_4, independent of the injection rate and the injection strategy. It can basically be traced back to differences in the strength of coagulation. When injecting SO_2, the injected SO_2 slowly oxidizes to H_2SO_4, which rapidly forms NS-SO_4 and KS-SO_4 via nucleation. Accordingly, for an injection of SO_2 the aerosol size distribution contains many NS-SO_4 and KS-SO_4 particles, independent of injection strategy and injection rate (Fig. 4.3). Since the NS-SO_4 and KS-SO_4 particles are significantly smaller than the larger AS-SO_4 and CS-SO_4 particles, coagulation between these particles is very strong. As a result, large sulfate particles grow continuously, which is further supported by condensation of gaseous H_2SO_4 formed by the oxidation of SO_2 (Niemeier and Timmreck, 2015). In contrast, a direct injection of H_2SO_4 results in the rapid initial formation of AS-SO_4 particles within the aircraft plume, which is why it was modeled as a direct injection of AS-SO_4 particles (see Section 3.2). However, NS-SO_4 and KS-SO_4 particles have no artificial sources, which is why their particle number is very low for all injections of H_2SO_4, independent of the injection strategy and the injection rate (Fig. 4.3). Therefore, most sulfate particles have approximately the same size, and particle growth by coagulation is weak. Accordingly, the initial

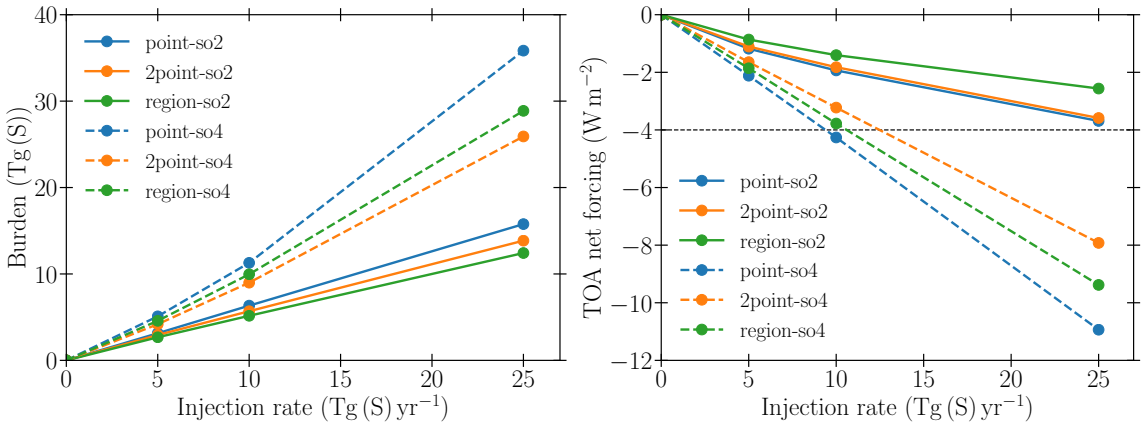

(a) M_{SO4} **(b)** ΔR_{TOA}

Figure 4.2: Global artificial sulfate burden M_{SO4} **(a)** and global mean TOA all-sky net forcing ΔR_{TOA} exerted by artificial sulfate aerosols **(b)** as a function of injection rate. Within **(b)** the dashed black line marks $\Delta R_{TOA} = -4\,\mathrm{W\,m^{-2}}$, which would be the negative forcing necessary to reduce the ScenarioMIP Tier1 high forcing scenario SSP5-8.5 to the corresponding Tier1 medium forcing scenario SSP2-4.5 (O'Neill et al., 2016).

AS-SO_4 particles hardly grow in size, which is why they are on average smaller than for an injection of SO_2.

As a direct consequence of the significantly higher global sulfate burden, also the radiative forcing is significantly stronger for an injection of H_2SO_4 than for the corresponding injection of SO_2 for all tested injection strategies and rates. This is clearly indicated by the global mean TOA all-sky net forcing ΔR_{TOA} exerted by the artificial stratospheric sulfate aerosols (Fig. 4.2 b). Consequently, counteracting a given GHG radiative forcing by an injection of SO_2 requires the injection of a significantly larger mass of sulfur than the injection of H_2SO_4 when using the same injection strategy. This gets very obvious for the GeoMIP6 experiment *G6sulfur* (Kravitz et al., 2015), which proposes to reduce the ScenarioMIP Tier1 high forcing scenario SSP5-8.5 to the corresponding Tier1 medium forcing scenario SSP2-4.5 by applying SAM. This would imply to counteract a forcing of $4.0\,\mathrm{W\,m^{-2}}$ (O'Neill et al., 2016). To counteract a forcing of $4.0\,\mathrm{W\,m^{-2}}$ by an injection of SO_2, the injection rate has to be clearly larger than $25\,\mathrm{Tg(S)\,yr^{-1}}$ for all tested injection strategies (Fig. 4.2 b). For an injection of H_2SO_4 the injection rate has to be only slightly above $10\,\mathrm{Tg(S)\,yr^{-1}}$, i.e. at maximum $12.5\,\mathrm{Tg(S)\,yr^{-1}}$ for the 2point injection. This corresponds to a reduction of the injection rate by clearly more than 50 %.

The maximum ΔR_{TOA} achieved in the performed experiments is -10.94 $\mathrm{W\,m^{-2}}$ for a point injection of $25\,\mathrm{Tg(S)\,yr^{-1}}$ in the form of H_2SO_4. The injection rate, which would be necessary to achieve the same ΔR_{TOA} by a point injection of SO_2, can be calculated using the exponential function given in Eq. 1 of Niemeier and Timmreck (2015).

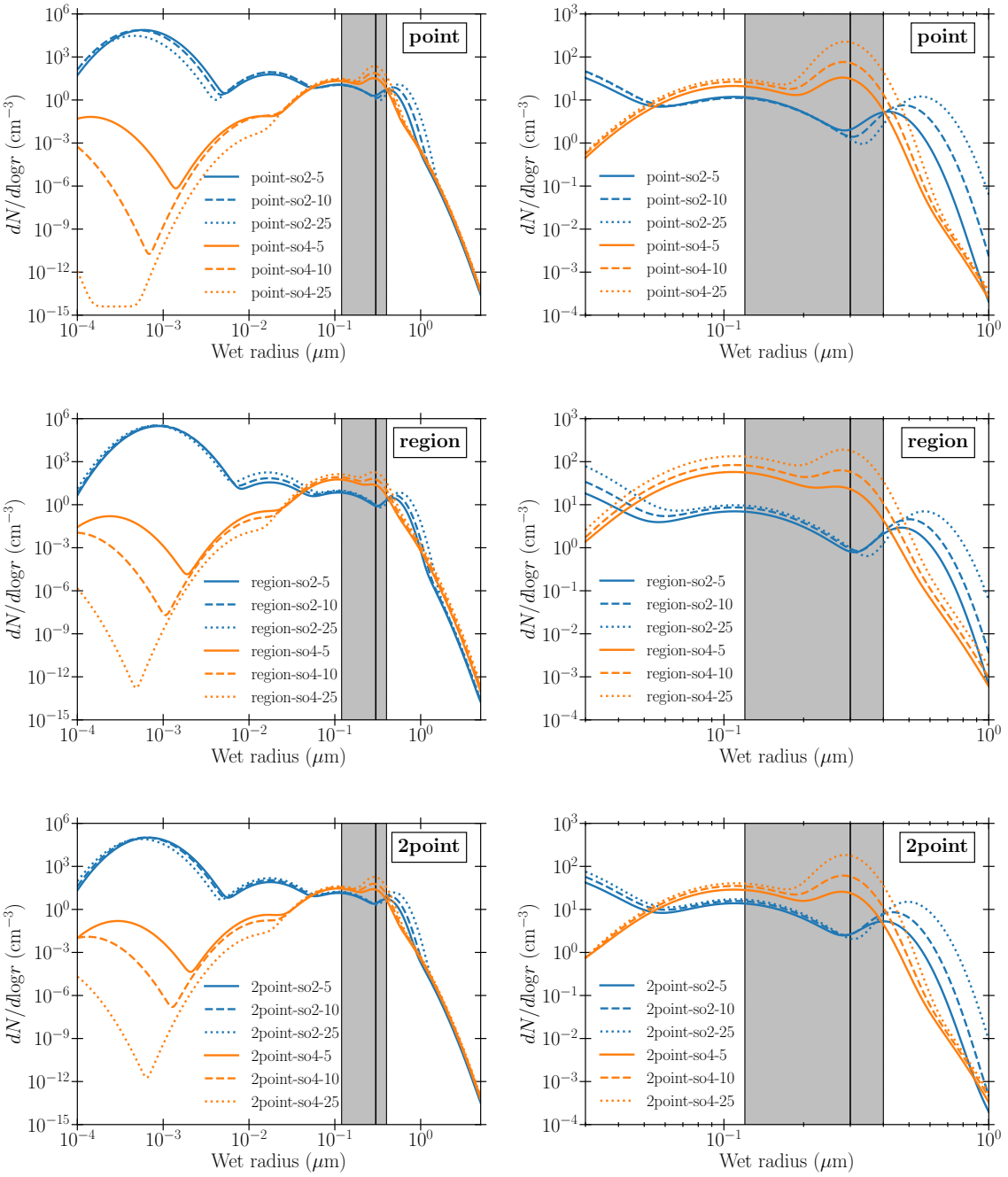

Figure 4.3: Global mean sulfate aerosol size distributions at 62.32 hPa, which is the central level of the injection layer, for the point injections **(top)**, the region injections **(center)**, and the 2point injections **(bottom)**. Subfigures in the right panel are a closeup of the corresponding subfigures in the left panel, which focus on AS-SO_4 and CS-SO_4. The grey bar marks the size range in which the backscattering efficiency of an aerosol particle with a respective wet radius is at least 70 % (i.e. 0.12 µm – 0.40 µm) of its maximum value following Dykema et al. (2016). The maximum value is achieved for aerosols with a wet radius of 0.30 µmm (Dykema et al., 2016), which is marked by a thick solid black line.

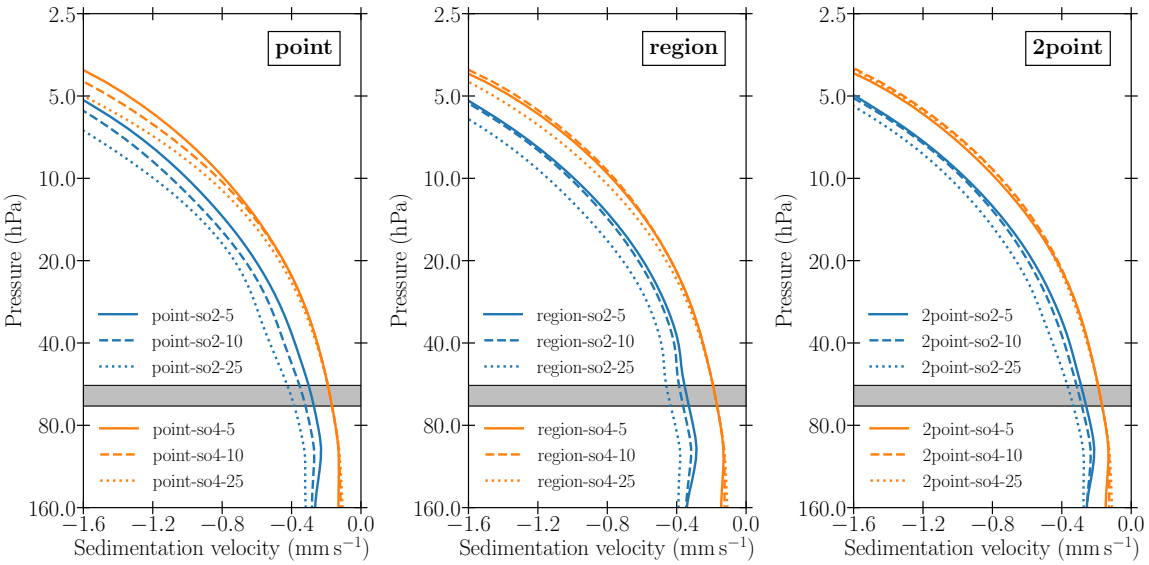

Figure 4.4: Vertical profile of global mean sedimentation velocity v_t of CS-SO_4 particles for all tested injection strategies and all tested injection rates. The grey bar marks the injection layer.

In their model setup, $\Delta R_{TOA} = -10.94\,W\,m^{-2}$ corresponds to a point injection of $182\,Tg(S)\,yr^{-1}$ in the form of SO_2, which is a more than seven-fold increase of the injection rate. An overview of the absolute numeric values of ΔR_{TOA} for all performed experiments is listed in Table 4.2.

Besides the higher global sulfate burden, also the on average smaller sulfate particles itself are a major reason for the significantly stronger ΔR_{TOA} when injecting H_2SO_4 instead of SO_2. This is shown by the sulfate aerosol size distributions in Figure 4.3 as well, which indicate that for an injection of H_2SO_4 the majority of the CS-SO_4 particles has a radius near $\sim 0.3\,\mu m$. According to Dykema et al. (2016), sulfate particles with a radius of $\sim 0.3\,\mu m$ have a maximal backscattering efficiency for incoming SW radiation (black solid line in Fig. 4.3). Particles with a radius between $\sim 0.12\,\mu m$ and $\sim 0.4\,\mu m$ have a backscattering efficiency of at least 70 % of the maximal value (grey bar in Fig. 4.3). However, for an injection of SO_2 the majority of the CS-SO_4 particles has a larger radius than $0.4\,\mu m$, independent of injection rate and injection strategy. Therefore, they are too large for efficient backscattering. Consequently, the backscattering process itself is clearly more efficient for an injection of H_2SO_4 than for an injection of SO_2.

4.2 Impact of injection rate

The impact of an increasing injection rate onto the sulfate aerosol size distribution, onto the global sulfate burden as well as onto the aerosol-induced radiative forcing has been already investigated for an injection of SO_2 in several studies, for example

Table 4.2: Global mean TOA all-sky net forcing ΔR_{TOA} exerted by artificial sulfate aerosols for all SAM experiments. The Y in the experiment name is a placeholder for the injection species. Column 2 and 3 show ΔR_{TOA} in $\mathrm{W\,m^{-2}}$ for the respective injection species.

Experiment	$\boldsymbol{\Delta R_{\mathrm{TOA}}(SO_2)}$ **(W m^{-2})**	$\boldsymbol{\Delta R_{\mathrm{TOA}}(H_2SO_4)}$ **(W m^{-2})**
point-Y-5	-1.18	-2.12
point-Y-10	-1.93	-4.26
point-Y-25	-3.69	-10.94
2point-Y-5	-1.10	-1.65
2point-Y-10	-1.82	-3.22
2point-Y-25	-3.59	-7.92
region-Y-5	-0.86	-1.86
region-Y-10	-1.40	-3.78
region-Y-25	-2.56	-9.38

Heckendorn et al. (2009), Niemeier et al. (2011), English et al. (2012), or Niemeier and Timmreck (2015). It has been found that with increasing injection rate the sulfate particles get on average larger, which reduces their global lifetime as well as their backscattering efficiency. This is due to the fact that for an injection of SO_2 an increase of the injection rate simply increases the availability of NS-SO_4 and KS-SO_4 particles in the vicinity and downwind of the injection area. Consequently, more sulfate mass is able to coagulate onto the large background particles, which makes them to grow on average larger than for lower injection rates. The same holds true for the condensation of gaseous H_2SO_4 onto sulfate aerosols: A higher injection rate enhances the availability of H_2SO_4, which results in stronger condensation onto pre-existing larger particles.

These characteristics of an injection of SO_2 were clearly confirmed within this study. As indicated by the sulfate aerosol size distribution, for an injection of SO_2 an increase of the injection rate results in a significant increase of both the CS-SO_4 radii and the CS-SO_4 number (Fig. 4.3). This is independent of the injection strategy. Concurrently, the particle radii and number of the other three modes are nearly independent of the injection rate (note the logarithmic scaling within Figure 4.3), which indicates that the additional sulfur mass more or less only accumulates in CS-SO_4 particles. Accordingly, for an increasing injection rate also the sedimentation velocity v_{t} clearly decreases – indicating stronger sedimentation – throughout the whole middle stratosphere when injecting SO_2 (Fig. 4.4). This decrease is independent of the injection strategy.

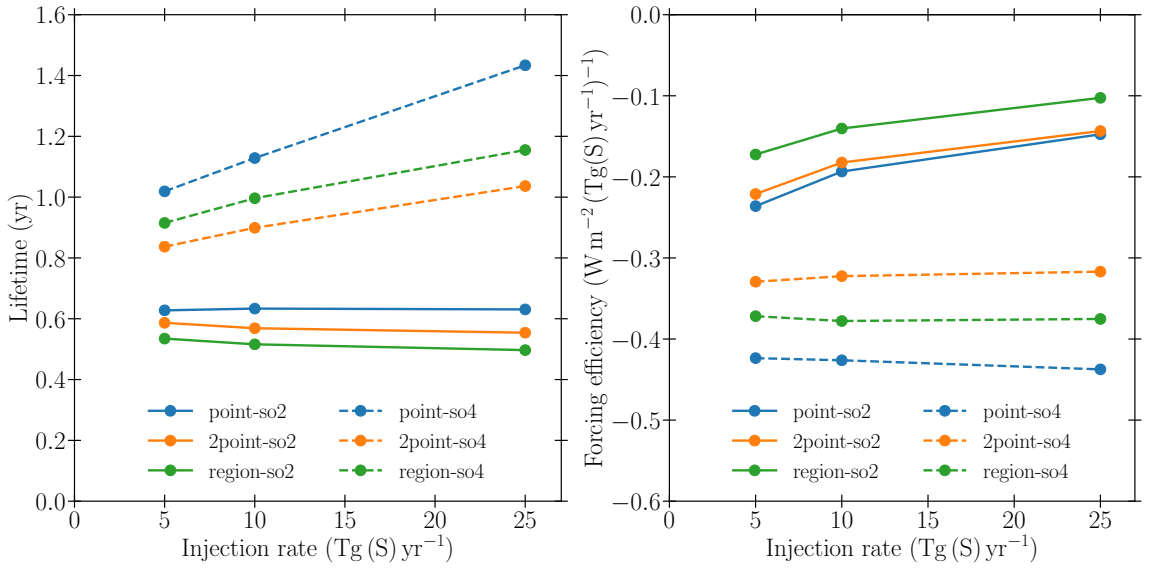

(a) τ_{SO4} **(b)** Γ_{TOA}

Figure 4.5: Global artificial sulfate lifetime τ_{SO4} **(a)** and global mean TOA all-sky net forcing efficiency Γ_{TOA} of the artificial sulfate aerosols **(b)** as a function of injection rate. The forcing efficiency can be interpreted as forcing per injection rate.

However, as shown in Figure 4.5 a, the strengthening of sedimentation due to an increase of the injection rate does not cause a significant reduction of the global stratospheric sulfate lifetime, which would be expectable. When injecting SO_2, the sulfate lifetime stays rather constant with increasing injection rate for all injection strategies. This apparent contradiction is caused by changes in the strength of tropical upwelling due to the aerosol-induced stratospheric heating, which is discussed in detail in Section 5.4.

As already mentioned in Section 4.1, the backscattering efficiency of sulfate particles decreases with increasing particle size when exceeding the optimum particle radius of $\sim 0.3\,\mu m$ (Dykema et al., 2016). For an injection of SO_2 the CS-SO_4 number and radii increase with injection rate, while the AS-SO_4 number and radii stay approximately constant. Consequently, the mass fraction of particles within the size range of most efficient backscattering (i.e. 0.12 µm - 0.4 µm) decreases with increasing injection rate (Fig. 4.3). Accordingly, for an injection of SO_2 also the global mean TOA all-sky net forcing efficiency Γ_{TOA} of the artificial sulfate aerosols – from now on simply termed forcing efficiency – reduces with injection rate (Fig. 4.5 b). The forcing efficiency is the ratio of the TOA all-sky net forcing ΔR_{TOA} to the injection rate $\dot{M}$:

$$\Gamma_{TOA} = \frac{\Delta R_{TOA}}{\dot{M}} \,. \tag{4.1}$$

Note, that within this study a decrease or a reduction of the forcing efficiency Γ_{TOA} means that it is getting closer to $\Gamma_{\mathrm{TOA}} = 0\,\mathrm{W\,m^{-2}\,(Tg(S)\,yr^{-1})^{-1}}$, regardless of sign. As shown by Figure 4.5 b, the decrease of the forcing efficiency with injection rate is further independent of the injection strategy. This is in accordance with the aforementioned studies and causes the exponential-like decay of ΔR_{TOA} with injection rate (Fig. 4.2 b).

In contrast, for an injection of H_2SO_4 the absolute values of the forcing efficiency are significantly higher (i.e. more negative) than for an injection of SO_2 (Fig. 4.5 b). This is a direct consequence of the significantly stronger ΔR_{TOA} achieved for an injection of H_2SO_4. Furthermore, the slope of the forcing efficiency with increasing injection rate is fundamentally different between both injection species. As visible in Figure 4.5 b, the achieved forcing efficiency is nearly independent of injection rate for an injection of H_2SO_4. This is explained by the fact, that for an injection of H_2SO_4 the particle size of the sulfate aerosols does on average not increase with injection rate. Accordingly, for an injection of H_2SO_4 an increase of the injection rate only increases the number of the AS-SO_4 and CS-SO_4 particles but on average not their radii (Fig. 4.3). Therefore, for all injection strategies the relative size distribution of the sulfate aerosols is independent of the injection rate. Since the majority of the CS-SO_4 particles have a size within the size range of most efficient backscattering (i.e. 0.12 µm - 0.4 µm), also the overall backscattering properties are independent of the injection rate for an injection of H_2SO_4. This results in a nearly constant forcing efficiency.

Microphysically, the independence of the average size of AS-SO_4 and CS-SO_4 particles from the injection rate is explained by the fact, that the AS-SO_4 particles, which initially form after an injection of H_2SO_4, have all approximately the same size. They also have nearly the same size as the the pre-existing sulfate particles in the aerosol layer. Therefore, an increase of the injection rate only results in an increase of the amount of same-sized particles, which, however, does not cause a significant increase of coagulation. Hence, the relative sulfate aerosol size distribution stays constant with increasing injection rate.

As an important consequence, ΔR_{TOA} depends on the injection rate approximately linearly for an injection of H_2SO_4 but not for an injection of SO_2. Accordingly, increasing the injection rate by a factor of 5 from $5\,\mathrm{Tg(S)\,yr^{-1}}$ to $25\,\mathrm{Tg(S)\,yr^{-1}}$ yields a strengthening of ΔR_{TOA} by a factor of approximately 5 for the H_2SO_4 injections, but only by a factor of around 3 for the SO_2 injections (Fig. 4.2 b).

When splitting up the forcing efficiency in its SW part ($\Gamma_{\mathrm{TOA,\,SW}}$) and its LW part ($\Gamma_{\mathrm{TOA,\,LW}}$), further differences between an injection of SO_2 and H_2SO_4 are identifiable (Fig. 4.6). As already demonstrated by Niemeier and Timmreck (2015), for an injec-

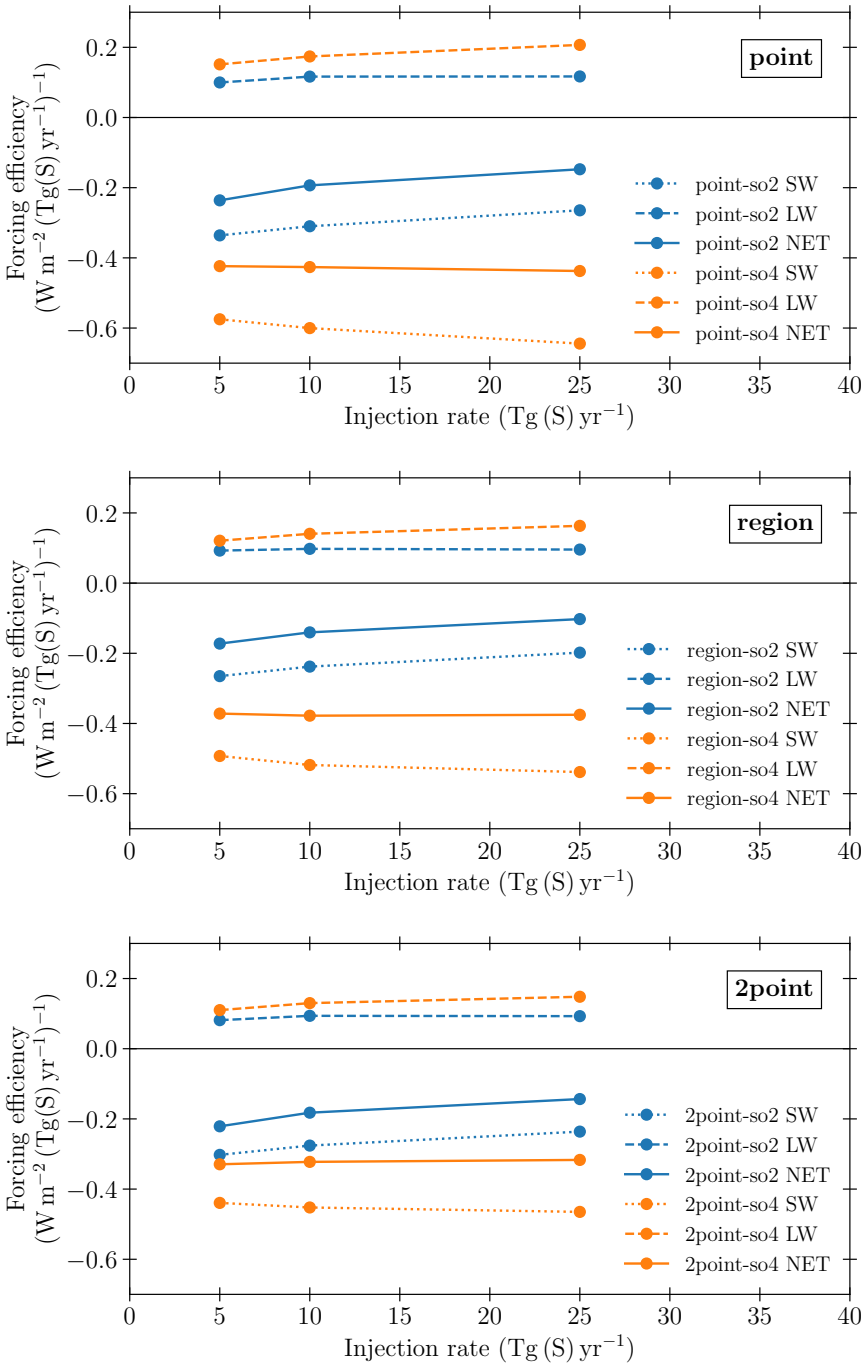

Figure 4.6: Global mean TOA all-sky net forcing efficiency Γ_{TOA} of artificial sulfate aerosols (solid), global mean TOA all-sky SW forcing efficiency $\Gamma_{\mathrm{TOA,SW}}$ of artificial sulfate aerosols (dotted), and global mean TOA all-sky LW forcing efficiency $\Gamma_{\mathrm{TOA,LW}}$ of artificial sulfate aerosols (dashed) as a function of injection rate for the point injections **(top)**, the region injections **(center)**, and the 2point injections **(bottom)**.

tion of SO_2 the reduction of the SW forcing efficiency with injection rate is clearly caused by its SW part due to less efficient backscattering for increasing particle size. In contrast, the LW forcing efficiency is approximately independent of injection rate for an injection of SO_2 and has a value of $\sim 0.1\,\mathrm{W\,m^{-2}\,(Tg(S)\,yr^{-1})^{-1}}$ for all injection strategies. This is a consequence of the fact, that the absorptivity of sulfate for IR radiation is nearly independent of the aerosol size. According to the Lambert-Beer law (Beer, 1852), it does rather depend on the absolute stratospheric sulfate burden. Since the global sulfate burden increases approximately linearly for an injection of SO_2 (Fig. 4.2 a), also the global mean TOA LW forcing $\Delta R_{\mathrm{TOA,\,LW}}$ exerted by artificial sulfate aerosols increases approximately linearly with increasing injection rate. This explains the independence of the LW forcing efficiency from the injection rate.

For an injection of H_2SO_4 the global sulfate burden increases superlinearly with injection rate (Fig. 4.2 a). Consequently, the LW forcing efficiency slightly increases with increasing injection rate as well, for all three injection strategies (Fig. 4.6). Moreover, also the SW forcing efficiency slightly increases with increasing injection rate (i.e. gets more negative). This results out of the fact that for an injection of H_2SO_4 the backscattering properties of the sulfate aerosol population are on average nearly independent of injection rate. Consequently, the global mean TOA SW radiative forcing $\Delta R_{\mathrm{TOA,\,SW}}$ exerted by artificial sulfate aerosols only depends on the total number of sulfate particles. Therefore, the SW forcing scales linearly with the global sulfate burden for an injection of H_2SO_4. Since the global sulfate burden increases superlinearly with injection rate, also the SW forcing gets slightly more efficient with injection rate.

When summed up, the slight increase of both the SW forcing efficiency and the LW forcing efficiency approximately cancel out each other for an injection of H_2SO_4. Therefore, the net forcing efficiency Γ_{TOA} is nearly independent of injection rate for all three injection strategies as already discussed.

While the TOA net forcing is important to describe the forcing exerted onto the whole Earth system, many processes or quantities within the climate system, for example evaporation or the global mean temperature in the reference height of 2 m, depend on the net forcing at Earth's surface (SFC). Figure 4.7 shows the according global mean SFC all-sky net forcing efficiency Γ_{SFC} of artificial sulfate aerosols. It is visible that the SFC net forcing efficiency is higher (i.e. more negative) than the TOA net forcing efficiency (Fig 4.6 b) of the corresponding injection scenario. The difference between the TOA net forcing efficiency and the SFC net forcing efficiency corresponds to the TOA LW forcing efficiency. This is explained by the fact, that the absorption of OLR and incoming NIR radiation takes place within the sulfate aerosol layer, which is located in the lower stratosphere. Therefore, the LW forcing

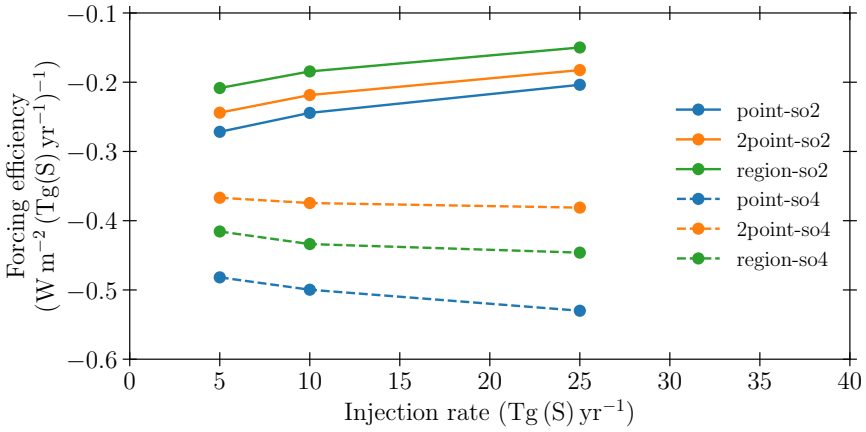

Figure 4.7: Global mean SFC all-sky net forcing efficiency $\Gamma_{\Delta R,\,\mathrm{SFC}}$ of artificial sulfate aerosols as a function of injection rate.

of the sulfate aerosols only impacts the net forcing above the sulfate aerosol layer, i.e. at TOA, significantly. For the global mean SFC all-sky net forcing ΔR_{SFC} the LW part is nearly neglectable. Consequently, the SFC LW forcing efficiency has a value of $\sim$ 0.01 W m^{-2} (Tg(S) yr^{-1})$^{-1}$ for all injection rates and strategies, which is approximately ten times smaller than the respective TOA LW forcing efficiency. Accordingly, the global mean SFC net forcing efficiency can be approximated by its SW part. This has an important implication for an injection of H_2SO_4. Due to the lack of a LW forcing, the SFC net forcing efficiency increases (i.e. gets more negative) with injection rate for all injection strategies (Fig 4.7). In contrast, the TOA net forcing efficiency was found to be approximately independent of injection strategy since increases of the SW and LW forcing efficiencies cancel out each other.

It was shown that for an injection of H_2SO_4 both the TOA SW and the TOA LW forcing scale linearly with the global sulfate burden, which increases superlinearly with injection rate (Fig. 4.2 a). A superlinear increase of the global sulfate burden is equivalent with an increase of the global sulfate lifetime. Accordingly, for an injection of H_2SO_4 an increase of the injection rate from 5 Tg(S) yr^{-1} to 25 Tg(S) yr^{-1} results in an increase of the global sulfate lifetime by 0.41 yr, 0.20 yr, and 0.23 yr for the point, 2point, and region injections, respectively. In the first place, this increase of the global sulfate lifetime with injection rate does not fit to the observed characteristics of the sedimentation velocity v_{t}, which was found to stay constant with injection rate for an injection of H_2SO_4 (Fig. 4.4). Therefore, one would initially expect the global sulfate lifetime to be independent of injection rate as well. However, the reason for this apparent contradiction are again dynamical feedback processes, on which details can be found in Section 5.4.

4.3 Impact of injection strategy

So far, the basic qualitative characteristics of an injection of SO_2 and an injection of H_2SO_4 as well as their differences have been found to be rather independent of the injection strategy. The injection strategy only seems to have an impact on the absolute values of the global artificial sulfate burden and global mean TOA all-sky net forcing. However, this impact can be quite substantial as visible in Figure 4.2. For instance, for an injection of H_2SO_4 with an injection rate of $25\,\mathrm{Tg(S)\,yr^{-1}}$, the global sulfate burden is higher by $\sim 10\,\mathrm{Tg(S)}$ for the point injection than for the 2point injection. This results in an $\sim 3\,\mathrm{W\,m^{-2}}$ or 38.1 % stronger global mean forcing. When injecting SO_2 with an injection rate of $25\,\mathrm{Tg(S)\,yr^{-1}}$, the global mean forcing is even 44.1 % stronger for a point injection than for a region injection. Furthermore, the injection strategy also impacts the meridional distribution of the sulfate aerosols significantly. Therefore, within this section the impact of the injection strategy will be investigated in more detail.

For an injection of SO_2, the huge impact of the injection strategy can be partly attributed to differences in microphysical processes. For example, Niemeier and Timmreck (2015) found that an injection into a zonally extended area causes the sulfate particles to grow on average larger than for a point-like injection into a single grid box. They attribute this feature to the greater availability of NS-SO_4 and KS-SO_4 particles when injecting into an extended area instead of into a single grid box. Since small NS-SO_4 and KS-SO_4 particles mainly occur in the injection area and downwind of it, also significant particle growth by coagulation with the globally dispersed coarse particles mainly occurs in this region. However, when injecting into an extended area also small NS-SO_4 and KS-SO_4 particles are available in a larger region, which leads to stronger coagulation and larger particles (Niemeier and Timmreck, 2015). Also in the simulations of this study, the region injections result in the on average largest sulfate particles for an injection of SO_2, as visible in Figure 4.8. For all injection rates, the number median radius of the CS-SO_4 particles is largest for a region injection of SO_2 compared to the respective point and 2point injections. Consequently, also the sedimentation of the CS-SO_4 particles is strongest for the region injection strategy. This causes the lower global sulfate burden compared to the other injection strategies (Fig. 4.2 a).

Additionally, for an injection of SO_2 the resulting CS-SO_4 particles have worse backscattering properties when injected into a region as compared to the other injection strategies (Fig. 4.8). This explains – together with the lower global sulfate burden – the lower forcing efficiency compared to the other injection strategies (Fig. 4.5 b).

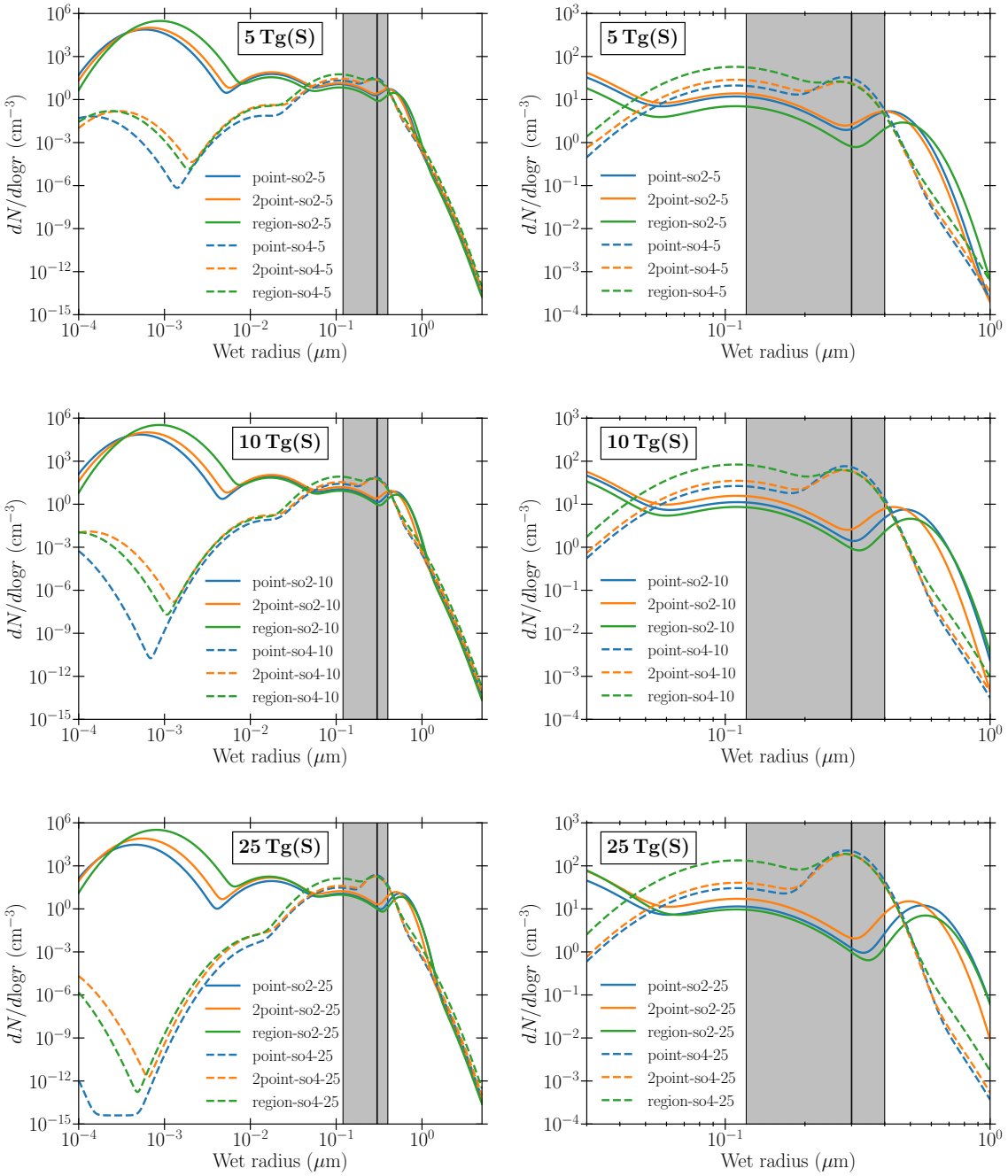

Figure 4.8: Global mean sulfate aerosol size distributions at 62.32 hPa, which is the central level of the injection layer, for an injection rate of 5 Tg(S) yr^{-1} **(top)**, 10 Tg(S) yr^{-1} **(center)**, and 25 Tg(S) yr^{-1} **(bottom)**. Subfigures in the right panel are a closeup of the corresponding subfigures in the left panel, which focus on AS-SO_4 and CS-SO_4 particles. The grey bar marks the size range in which the backscattering efficiency of an aerosol particle with a respective wet radius is at least 70 % (i.e. 0.12 µm – 0.40 µm) of its maximum value following Dykema et al. (2016). The maximum value is achieved for aerosols with a wet radius of 0.30 µm (Dykema et al., 2016), which is marked by a thick solid black line. The data presented in this figure is the same as Figure 4.3, but rearranged.

Compared to the point and the region injections, the 2point injections of SO_2 result in the on average smallest CS-SO_4 particles, which is shown in Figure 4.8. It is clearly visible, that the resulting sulfate aerosol population shows better backscattering properties. Consequently, despite a lower global sulfate burden compared to the point injections, the 2point injections achieve nearly the same global mean forcing for all injection rates, as shown in Figure 4.2. The small CS-SO_4 particle size for the 2point injections of SO_2 is a consequence of the point-like injection strategy, which reduces coagulation significantly compared to the region injections. Furthermore, the injection rate at each of the two injection points is only half as high as for the single injection point in the point injection, which reduces the concentration of small NS-SO_4 and KS-SO_4 particles downwind of the injection area. Therefore, coagulation is weaker compared to the point injection, which results in on average smaller particles. However, the poleward transport and the sedimentation of the sulfate aerosols is stronger for the 2point injections compared to the point injections due to the extratropical injection locations of the 2point injection strategy. Accordingly, the stratospheric sulfate lifetime for the 2point injections is shorter than for the point injections, despite the on average smaller sulfate particles (Fig. 4.5 a). This explains the lower global sulfate burden compared to the point injections.

In contrast to an injection of SO_2, for an injection of H_2SO_4 the average particle size of the AS-SO_4 and CS-SO_4 particles is rather independent of the injection strategy for all tested injection rates (Fig. 4.8). This can again be attributed to the approximately uniform size of the initial AS-SO_4 particles, which form rapidly out of the injected H_2SO_4 within the aircraft plume. The nearly uniform size effectively prevents any significant coagulation for all tested injection strategies. However, when looking at Figure 4.8 in detail, one can see that the point injections result in slightly more CS-SO_4 and less AS-SO_4 particles than the region injections. This can be explained by the higher number concentration of AS-SO_4 within the injection area when injecting at a single point compared to when injecting into an extended area. A higher number concentration of AS-SO_4 increases the collision probability of two particles and, consequently, also the probability of self-coagulation. Nevertheless, compared to an injection of SO_2, the microphysical differences between the injection strategies are neglectable for an injection of H_2SO_4.

As a consequence, the backscattering properties of the sulfate aerosol size distribution are rather independent of the injection strategy for an injection of H_2SO_4. Therefore, the achieved global mean radiative forcing of an injection primarily depends on the global sulfate burden. This gets very obvious in Figure 4.8: For a given injection rate, the point injections of H_2SO_4 result in the highest global sulfate burden as well as the strongest global mean radiative forcing. On the other hand, the 2point injections

result in the lowest global sulfate burden as well as the lowest global mean radiative forcing.

Obviously, for an injection of H_2SO_4, aerosol microphysical processes cannot account for the observed substantial impact of the injection strategy onto the global sulfate burden and the global mean radiative forcing. For an injection of SO_2, aerosol microphysical processes can only partly explain the observed huge differences between the injection strategies. Consequently, the strong dependency of the global sulfate burden and the global mean radiative forcing on the injection strategy can only be explained by differences in the poleward transport of sulfate aerosols. Since sedimentation and aerosol deposition processes are weak within the tropics compared to the extratropics and polar regions, the strength of the poleward transport of sulfate aerosols is crucial for the stratospheric lifetime of sulfate aerosols. It significantly depends on the injection strategy via the position of the injection locations relative to the subtropical transport barriers (Niemeier and Timmreck, 2015; Niemeier and Schmidt, 2017; Tilmes et al., 2017).

The effect of the subtropical transport barriers gets clearly visible in Figure 4.9, which shows the zonally averaged distribution of the sulfate burden (Fig. 4.9 a) and the TOA net radiative forcing (Fig. 4.9 b). The zonally averaged distribution of the sulfate burden shows a clear dependence on the injection strategy, while being nearly independent of injection species and rate. For the point injections, the meridional distribution of sulfate aerosols is characterized by a clear maximum at the equator because the injection point is located directly within the tropical pipe. Since the tropical pipe is bounded by strong subtropical transport barriers, the meridional transport of artificial sulfate aerosols out of the tropical pipe towards the extratropics is strongly inhibited. This causes the strong tropical confinement of the sulfate particles, which is clearly visible in Figure 4.9 a. The tropical confinement is further enhanced by the general tropical upwelling of the BDC, which counteracts sedimentation. As a consequence, for both injection species the point injections result in a low extratropical (i.e. poleward of approximately 30° N and 30° S) sulfate burden (Fig. 4.9 a). However, the tropical confinement is slightly stronger for an injection of H_2SO_4 than for an injection of SO_2. This is caused by dynamical feedback processes, for which details can be found in Section 5.4. The strong tropical confinement of sulfate particles significantly enhances their global stratospheric lifetime (Fig. 4.5 a). Therefore, for both injection species the point injections result in the highest global sulfate burden (Fig. 4.2 a) as well as the highest global mean forcing efficiency (Fig. 4.5 b).

For the region injections, a significant part of the injection area is located outside of the tropical pipe and, hence, poleward of the subtropical transport barriers, which are located at approximately 10° S and 10° N. Therefore, the tropical sulfate burden

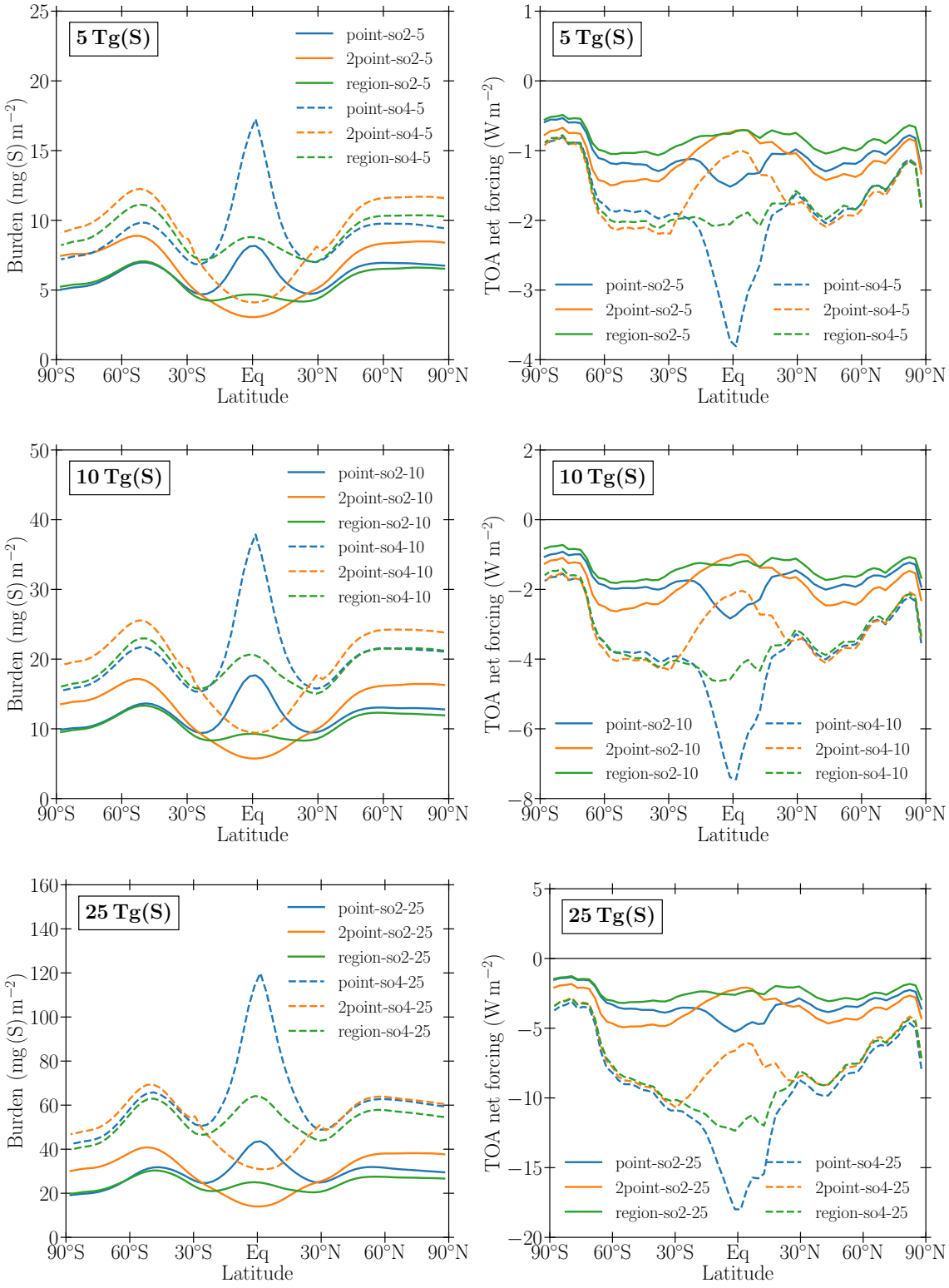

(a) $\overline{M}_{\mathrm{SO4}}$ **(b)** $\Delta\overline{R}_{\mathrm{TOA}}$

Figure 4.9: Zonal mean artificial sulfate burden $\overline{M}_{\mathrm{SO4}}$ **(a)** and zonal mean TOA all-sky net forcing $\Delta\overline{R}_{\mathrm{TOA}}$ exerted by artificial sulfate aerosols **(b)** for an injection rate of $5\,\mathrm{Tg(S)\,yr^{-1}}$ **(top)**, $10\,\mathrm{Tg(S)\,yr^{-1}}$ **(center)**, and $25\,\mathrm{Tg(S)\,yr^{-1}}$ **(bottom)**. Note the different scaling on the y-axes.

is significantly lower for the regional injections than for the point injections. For both injection species the zonally averaged distribution of sulfate aerosols reveals only a slight local maximum at the equator, as visible in Figure 4.9 (a). Furthermore, sulfur which is injected outside the tropical pipe and into the surf zone is transported rapidly towards higher latitudes. Consequently, for the region injections one would expect a higher extratropical sulfate burden than for the point injections. However, this is only the case for an injection of H_2SO_4 with an injection rate of $5\,\mathrm{Tg(S)\,yr^{-1}}$ and $10\,\mathrm{Tg(S)\,yr^{-1}}$. For the region injections of SO_2 the extratropical sulfate burden is rather low and approximately as high as for the respective point injection. This can be attributed to the on average larger particles, which form during a region injection compared to a point injection (Fig. 4.8) and have a shorter stratospheric sulfate lifetime.

To conclude, the global stratospheric sulfate lifetime is clearly reduced due to partly injecting outside of the tropical pipe and the accompanied stronger poleward transport of the sulfate particles (Fig. 4.5 a). Therefore, for both injection species the global sulfate burden as well as the global mean radiative forcing are lower for a region injection than for a respective point injection (Fig. 4.2 a).

Furthermore, for the point as well as the region injections the zonally averaged distribution of sulfate aerosols exhibits a clear local minimum located approximately at 25° S and 25° N (Fig. 4.9 a). This minimum is explained by the strong poleward isentropic mixing within the stratospheric surf zone, which is located at this latitudes.

Within the 2point injection strategy, the injection points are located at 30° N and 30° S and, hence, directly within the surf zone. Therefore, the majority of the injected sulfur is rapidly transported polewards. Consequently, the 2point injections reveal the highest extratropical as well as the lowest tropical sulfate burden of all three tested injection strategies (Fig. 4.9 a). Furthermore, the strong poleward transport of the majority of injected sulfur reduces its global stratospheric lifetime significantly (Fig. 4.5 a). Therefore, for an injection of H_2SO_4 the 2point injections exhibit the shortest global sulfate lifetime of all three injection strategies and, consequently, the lowest global sulfate burden. For an injection of SO_2, the global sulfate lifetime is slightly longer for the 2point injections than for the region injections, despite a stronger poleward transport of the sulfate aerosols. This can be attributed to the smaller sulfate particles, which result out of the point-like injection strategy of the 2point injections.

For all three injection strategies and independent of injection species and rate, the zonally averaged distribution of the sulfate aerosols exhibits a local maximum located at approximately 50° S and 50° N. This local maximum is especially pronounced in the southern hemisphere and is caused by the winter polar vortex, which forms a

meridional transport barrier and prevents a farther poleward transport of the sulfate aerosols. Therefore, the particles accumulate slightly equatorward of the winter polar vortex.

Since the TOA radiative forcing depends strongly on the sulfate burden, also the zonal mean TOA radiative forcing exhibits significant meridional differences (Fig. 4.9 b). Especially within the tropics the exerted radiative forcing strongly depends on the injection strategy. The point injections result in the strongest radiative forcing within the tropics for both injection species as well as for all tested injection rates. This would potentially lead to an overcooling of the tropics compared to the extratropics. The tropical overcooling would be stronger for an injection of H_2SO_4 than for a respective injection of SO_2: For an injection of H_2SO_4 the radiative forcing at the equator is approximately twice as strong as the radiative forcing in the midlatitudes (i.e. 45° S and 45° N), while for an injection of SO_2 it is only about 50 % stronger than at the equator. The stronger tropical overcooling for an injection of H_2SO_4 conforms to the stronger tropical confinement of sulfate particles.

For all three injection rates, the 2point injections clearly exhibit the weakest tropical forcing of all three injection strategies. It is clearly weaker than the extratropical forcing for both injection species, which would lead to a significant tropical undercooling. The region injections exhibit the meridionally most uniform radiative forcing of all three injection strategies. For both injection species, the difference between the tropical and the extratropical forcing is small, which would result in a meridionally uniform cooling. Within the extratropics, the differences of the radiative forcing between all three injection strategies are relatively weak.

However, the local maxima of the sulfate burden at approximately 50° S and 50° N, which are associated with the winter polar vortex, as well as the local minima of the sulfate burden at approximately 30° S and 30° N, which are associated with the strong meridional transport of the surf zone, are not existent in the zonally averaged distribution of the TOA radiative forcing. This can be attributed to the decrease of incoming SW radiation towards the poles, which compensates for the observed differences of the sulfate burden. Consequently, the resulting radiative forcing is meridionally rather uniform between 30° S and 60° S as well as 30° N and 60° N.

5 Comparison of the Stratospheric Warming and the Induced Dynamical Feedback

Radiative heating of the tropical lower stratosphere is a well-known adverse side effect of SAM, which has been observed in multiple studies, for example Heckendorn et al. (2009) or Ferraro et al. (2011). It is caused by the absorption of both OLR and incoming NIR radiation by the stratospheric sulfate aerosols. The accompanied positive temperature anomaly of the lower stratosphere modifies the BDC as well as the QBO (Aquila et al., 2014). The modified transport patterns then may change the distribution of the sulfate aerosols as well as their microphysical properties. This dynamical feedback has been investigated for example by Niemeier and Schmidt (2017). However, so far almost all studies investigating these adverse side effects of SAM have focused on an injection of SO_2. Therefore, within this section, the stratospheric heating and following dynamical changes are compared between an injection of SO_2 and H_2SO_4.

5.1 Modification of the stratospheric temperature

In contrast to scattering, the absorption of radiation is rather independent of the sulfate particle size, since it depends on the molecular structure of the sulfate ion. For that reason, the absorption of OLR and incoming NIR radiation by sulfate particles in a given height can be assumed to depend purely on the sulfate concentration in that height. This can be clearly seen in Figure 5.1, which shows the zonal mean net heating rate $\partial\overline{T}/\partial t$, from now on termed $\overline{T}_{\mathrm{t}}$, and the zonal mean sulfate mass mixing ratio $\overline{m}_{\mathrm{SO4}}$ for the injections with an injection rate of $10\,\mathrm{Tg(S)\,yr^{-1}}$: The heating of the stratosphere due to the absorption of OLR and NIR radiation and the sulfate load clearly coincide with each other with regard to their meridional and vertical extent as well as their strength. Accordingly, a higher sulfate load at a given location clearly results in a stronger heating anomaly at that location. For a higher vertical extent of the sulfate layer, like for point-so4-10, the stratospheric heating anomaly extends higher up. It is clearly discernible, that the heating of the lower stratosphere itself is in principle independent of the injection species. However, since an injection of H_2SO_4 results in a higher sulfate load, the stratospheric heating anomaly is stronger for an injection of H_2SO_4 than for a respective injection of SO_2.

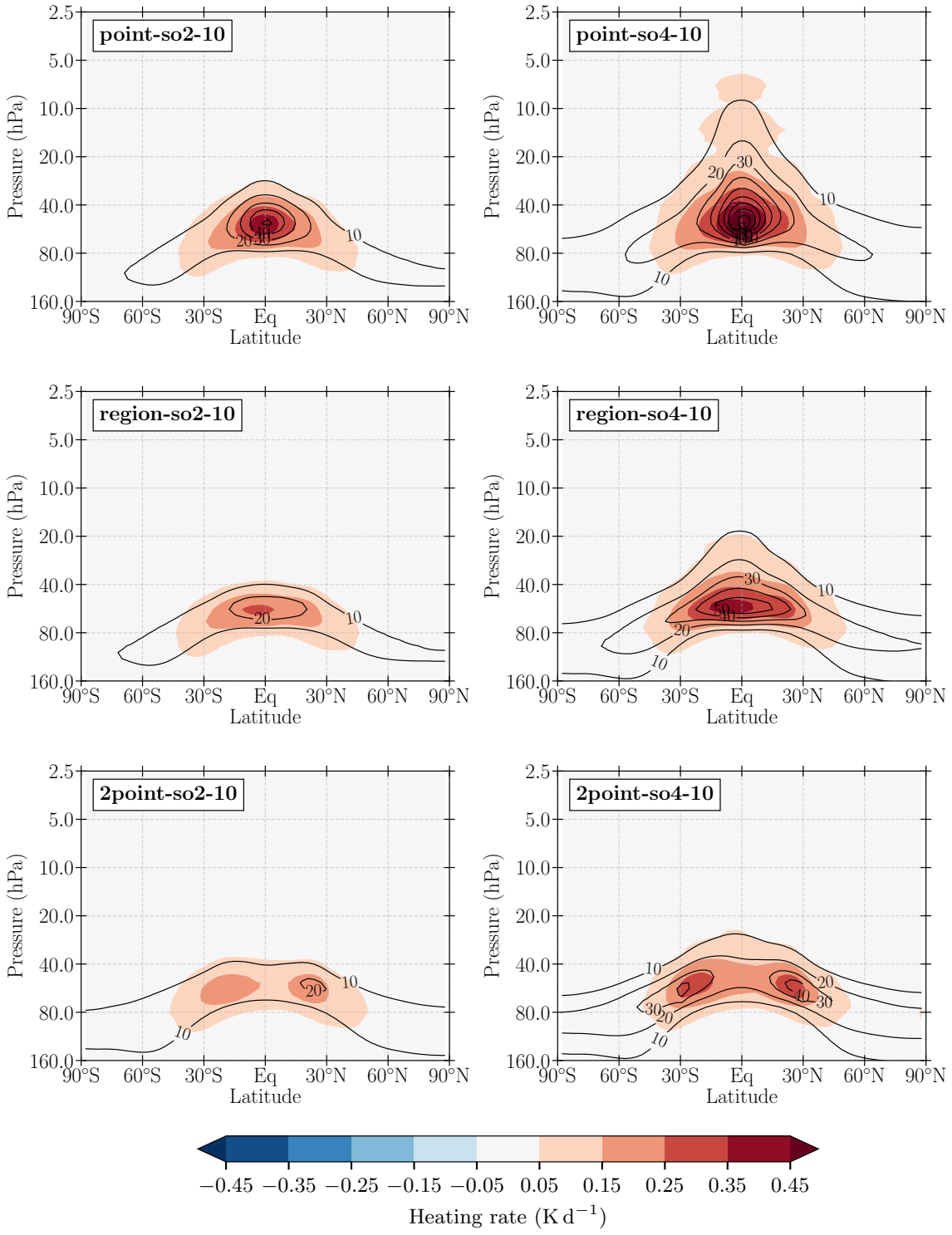

Figure 5.1: Vertical profile of the zonal mean net heating rate $\overline{T}_\mathrm{t}$ for injections with an injection rate of 10 Tg(S) yr^{-1}. Black contour lines indicate the zonal mean sulfate mass mixing ratio $\overline{m}_\mathrm{SO4}$ in µg kg^{-1} with a contour interval of 10 µg kg^{-1}. The respective plots for the injections with an injection rate of 5 Tg(S) yr^{-1} and 25 Tg(S) yr^{-1} can be found in appendix A1.

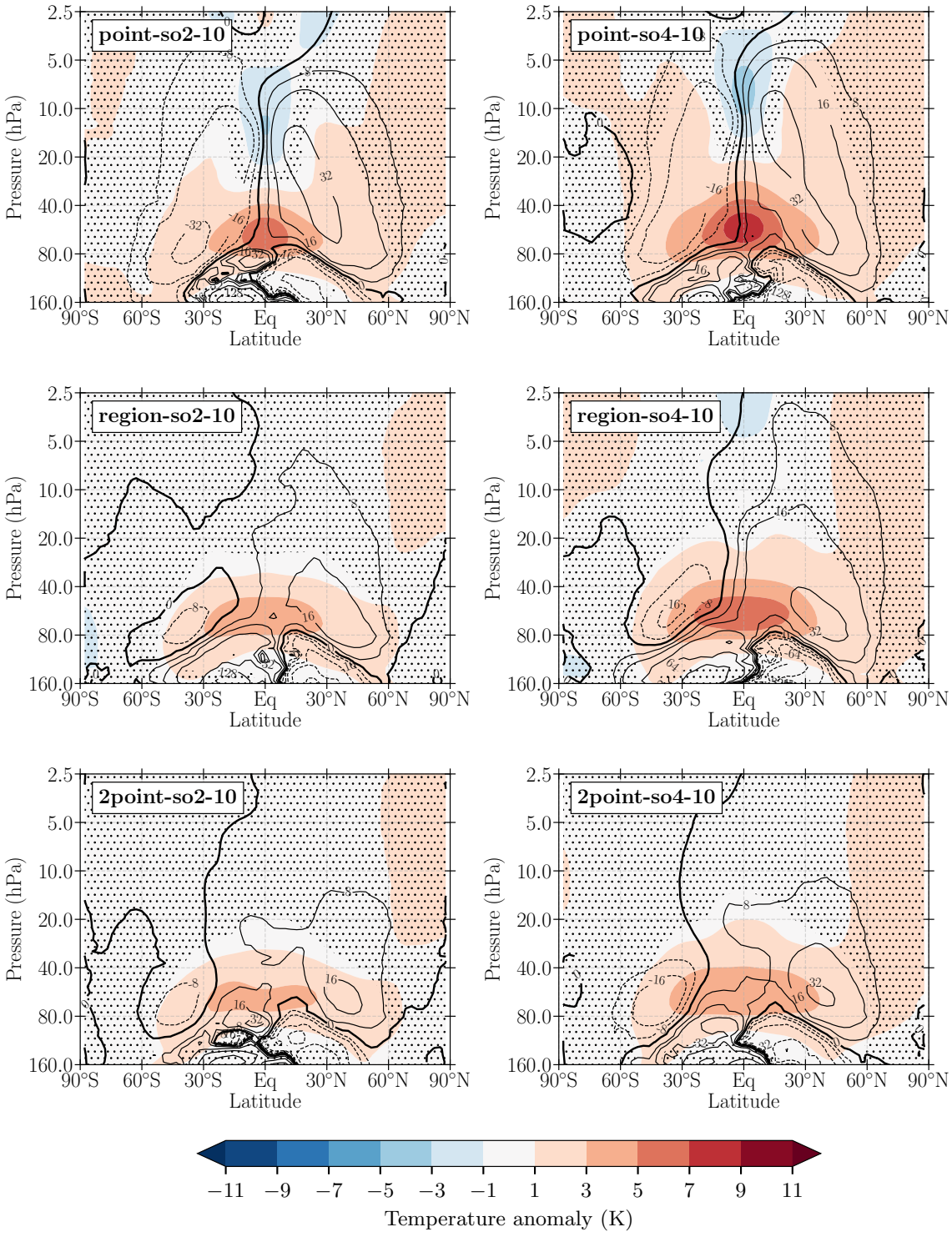

Figure 5.2: Vertical profile of the anomaly of the zonal mean temperature ($\Delta\overline{T}$) for injections with an injection rate of $10\,\mathrm{Tg(S)\,yr^{-1}}$. Stippling indicates areas for which $\Delta\overline{T}$ is not significant at the 95 % level in a student's t-test. Black contour lines show the anomaly of the residual mass stream function ($\Delta\chi^*$) in $\mathrm{kg\,s^{-1}}$ with contour intervals increasing by powers of two. The thick solid line denotes $\Delta\chi^* = 0\,\mathrm{kg\,s^{-1}}$. Solid lines indicate a clockwise circulation anomaly, dashed lines indicate an anticlockwise circulation anomaly. The respective plots for the injections with an injection rate of $5\,\mathrm{Tg(S)\,yr^{-1}}$ and $25\,\mathrm{Tg(S)\,yr^{-1}}$ can be found in appendix A2.

The meridional structure of the stratospheric heating anomaly clearly depends on the injection strategy due to its dependence on the location and concentration of the stratospheric sulfate layer (Sec. 4.3). The point injections result in a strong heating anomaly, which is clearly confined to the tropical lower stratosphere. For the region injections, the strongest heating anomaly is located in the tropical lower stratosphere, as well, but less confined and weaker than for the point injections. For the 2point injections, the strongest heating anomalies are located in the subtropics at approx. 30° N and 30° S.

The aerosol-induced heating causes a warming of the lower stratosphere. Thereby, the location and strength of the lower stratospheric warming basically follows the location and strength of the stratospheric heating anomaly, which is clearly visible in Figure 5.2. Accordingly, also the warming of the lower stratosphere is slightly stronger for an injection of H_2SO_4 than for a respective injection of SO_2, but does in principle not depend on the injection species. When comparing the different injection strategies, the zonal mean temperature anomaly $\Delta\overline{T}$ exhibits the same differences as the zonal mean heating rate. The point injections result in a very strong warming of the lower tropical stratosphere with the highest temperature anomalies directly located at the equator. The region and 2point injections lead to a meridionally more uniform warming of the lower stratosphere between approx. 30° N and 30° S. Based on a student's t-test, the warming of the lower tropical and subtropical stratosphere is significant at the 95 % level for all three injection strategies and for both injection species.

For the injections with an injection rate of $5\,\mathrm{Tg(S)\,yr^{-1}}$ and $25\,\mathrm{Tg(S)\,yr^{-1}}$ the heating and the warming of the lower stratosphere exhibit basically the same characteristics as for the injections with an injection rate of $10\,\mathrm{Tg(S)\,yr^{-1}}$, which were discussed in this section. However, since the strength of the stratospheric heating anomaly strongly depends on the stratospheric sulfate mass mixing ratio, it also significantly depends on the injection rate. Therefore, for both injection species and all injection strategies, an injection with an injection rate of $5\,\mathrm{Tg(S)\,yr^{-1}}$ results in a clearly weaker warming than an injection with an injection rate of $10\,\mathrm{Tg(S)\,yr^{-1}}$. An injection with an injection rate of $25\,\mathrm{Tg(S)\,yr^{-1}}$ results in a significantly stronger warming than an injection with an injection rate of $10\,\mathrm{Tg(S)\,yr^{-1}}$. The respective plots of the zonal mean net heating rate (Fig. 5.1) and the zonal mean temperature anomaly (Fig. 5.2) for the injections with an injection rate of $5\,\mathrm{Tg(S)\,yr^{-1}}$ and $25\,\mathrm{Tg(S)\,yr^{-1}}$ can be found in appendix A1 and A2.

5.2 Modification of the QBO

For an injection rate of 10 $\mathrm{Tg(S)\,yr^{-1}}$, the warming of the lower tropical stratosphere causes a significant modification of the QBO for the point and the region injections, which is clearly visible in Figure 5.3. For both point injections, the QBO is locked in a constant westerly phase in the lower stratosphere after the first year of SAM. On top of the constant westerlies, constant easterlies are prevalent in the upper stratosphere. For point-so4-10, the westerlies extend up to approx. 10 hPa, while for point-so2-10 the westerlies extend only up to approx. 15 hPa. With values of the tropical mean (i.e. 5° N to 5° S) zonal wind $\overline{u}_{\mathrm{trop}}$ of up to approx. 25 $\mathrm{m\,s^{-1}}$, the westerlies are also slightly stronger for point-so4-10 than for point-so2-10, for which the maximum winds only reach approx. 21 $\mathrm{m\,s^{-1}}$. This is in accordance with other studies, for example Aquila et al. (2014), Niemeier and Schmidt (2017), or Richter et al. (2017), who observed a significant prolongation of the QBO westerly phase depending on the injection rate, and – for a sufficiently high injection rate – persistent westerlies within the lower stratosphere.

For both region injections, the period of the QBO is significantly prolonged and westerlies clearly dominate in the lower stratosphere. Furthermore, the modification of the QBO is slightly stronger for an injection of H_2SO_4 than for an injection of SO_2 for the region injections as well. However, in contrast to the point injections of 10 $\mathrm{Tg(S)\,yr^{-1}}$, the QBO is not locked in a permanent westerly phase. This is in agreement with Niemeier and Schmidt (2017), who showed that an injection of SO_2 with an injection rate of 10 $\mathrm{Tg(S)\,yr^{-1}}$ into a belt along the equator between 30° S and 30° N results in a weaker modification of the QBO than an equatorial point injection of SO_2 with the same injection rate.

In contrast to the point and region injections, the QBO is basically not modified for the 2point injections. For both injection species, the periodicity as well as the strength of the QBO winds are not changed significantly compared to contr-000.

The respective Hovmøller diagrams of the QBO for the injections with an injection rate of 5 $\mathrm{Tg(S)\,yr^{-1}}$ and 25 $\mathrm{Tg(S)\,yr^{-1}}$ can be found in appendix A3. For the injections with an injection rate of 5 $\mathrm{Tg(S)\,yr^{-1}}$, the modifications of the QBO are weaker than for the respective injections with an injection rate of 10 $\mathrm{Tg(S)\,yr^{-1}}$. Accordingly, the QBO only breaks down in point-so4-5, where it is locked in a constant westerly phase up to approx. 20 hPa. In the experiments region-so2-5, region-so4-5, and point-so2-5 the period of the QBO is prolonged but the tropical stratospheric winds remain in a QBO-like pattern. In 2point-so2-5 and 2point-so4-5 the QBO is not modified. For the injections with an injection rate of 25 $\mathrm{Tg(S)\,yr^{-1}}$, the modifications of the QBO are stronger than for the respective injections with an injection rate of 10 $\mathrm{Tg(S)\,yr^{-1}}$.

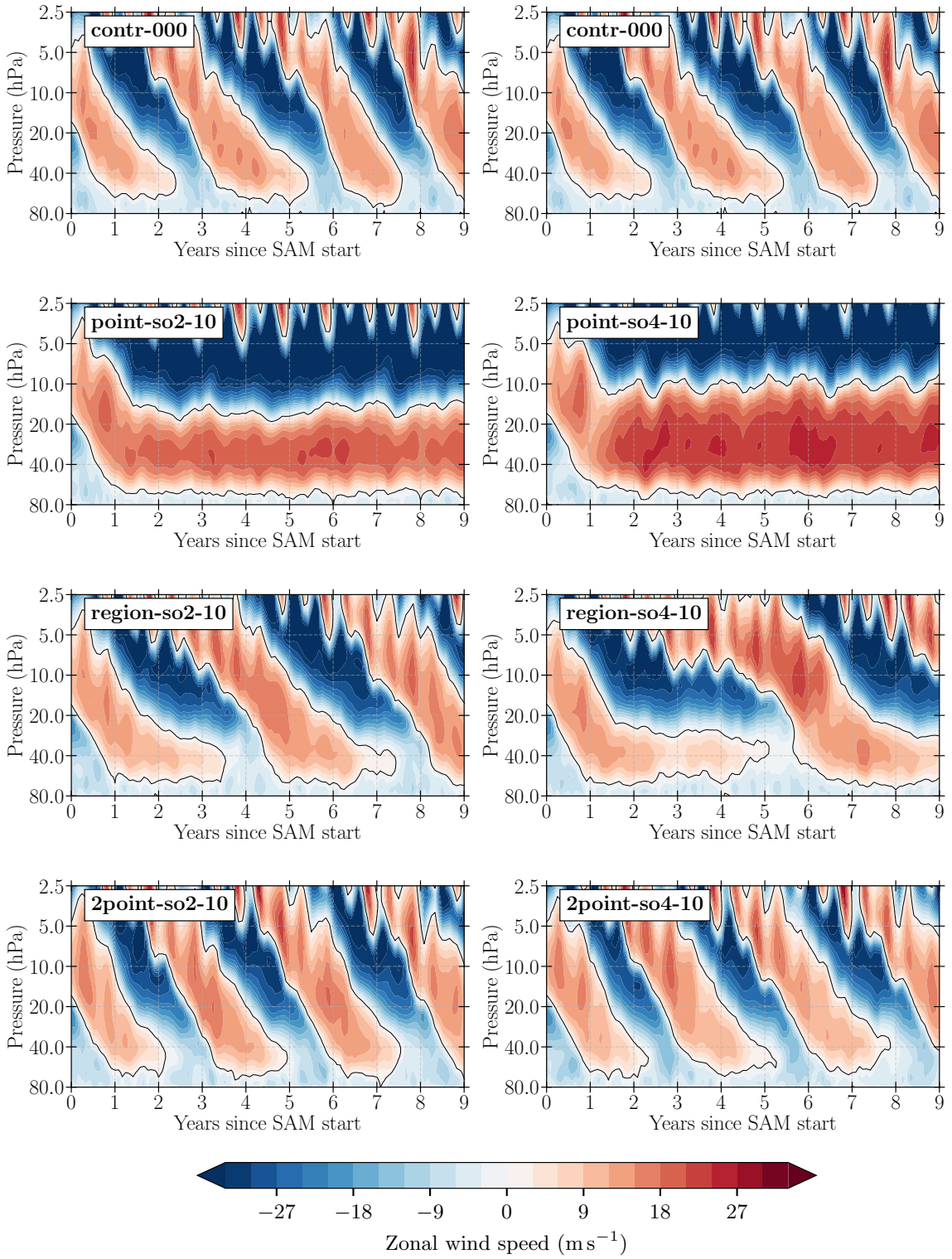

Figure 5.3: Temporal evolution of the tropical (5° N to 5° S) mean zonal wind $\overline{u}_{\text{trop}}$ in the stratosphere during the study period of ten years for injections with an injection rate of $10\,\text{Tg(S)}\,\text{yr}^{-1}$. For comparison, the top row shows $\overline{u}_{\text{trop}}$ of contr-000, which represents an unperturbed QBO. The solid black line marks $\overline{u}_{\text{trop}} = 0\,\text{m}\,\text{s}^{-1}$.

In point-so2-25 and point-so4-25 the QBO is locked in a very strong westerly phase. The QBO further breaks down in region-so2-25 and region-so4-25, which results in constant westerlies within the lower stratosphere as well.
In 2point-so2-25 and 2point-so4-25 the QBO is not modified significantly, but, however, its easterly phase is slightly prolonged in the lower stratosphere, which is accompanied by slightly weaker westerlies in this region. Similar results have been found by Tilmes et al. (2018) for a simultaneous injection of SO_2 at 15° S and 15° N. For injection rates of $12\,\mathrm{Tg(S)\,yr^{-1}}$ as well as $16\,\mathrm{Tg(S)\,yr^{-1}}$, they found slight easterly anomalies of the zonal wind in the lower tropical stratosphere due to a slight prolongation of the QBO easterly phase. Additionally, Richter et al. (2017) showed that for subtropical single-point injections of $6\,\mathrm{Tg(S)\,yr^{-1}}$ at 15° S, 15° N, 30° S, and 30° N the QBO speeds up instead of slowing down.
Furthermore, the modification of the QBO is slightly stronger for an injection of H_2SO_4 than for the corresponding injection of SO_2 for all injection rates. This is explained by the fact that for a given injection strategy and rate the stratospheric warming is stronger for an injection of H_2SO_4 than for an injection of SO_2 (Sec. 5.1). However, the principle response of the QBO to an aerosol-induced warming of the lower tropical stratosphere is independent of the injection species, but does strongly depend on the injection strategy.

5.2.1 Dynamic mechanisms of the modification of the QBO

The dynamic mechanisms which cause the observed modification and breakdown of the QBO have been investigated by Aquila et al. (2014) for an equatorial point injection of SO_2. They assume that for equatorial point injections of SO_2 a disruption of the thermal wind balance in the tropical stratosphere (Eq. 2.6) due to the aerosol-induced warming is the main reason for a modification of the QBO. However, they did not explicitly investigated the meridional gradient of the zonal mean temperature $\partial\overline{T}/\partial y$, from now on termed $\overline{T}_{\mathrm{y}}$, as well as the meridional curvature of the zonal mean temperature $\partial^2\overline{T}/\partial y^2$, from now on termed $\overline{T}_{\mathrm{yy}}$, in order to validate their assumption. This is done for the simulations of this study, whereby the disruption of the thermal wind balance in the tropical stratosphere due to the aerosol-induced warming is clearly confirmed as the main reason for the observed modification of the QBO for all three tested injection strategies.
For the point injections, the strong warming abates the usually positive poleward meridional temperature gradient $\overline{T}_{\mathrm{y}}$ within the lower tropical stratosphere significantly, as shown for point-so4-10 in Figure 5.4 a (top). This is accompanied by a significant negative anomaly of the meridional temperature curvature $\overline{T}_{\mathrm{yy}}$ (Fig. 5.4 b, top). A region of negative $\overline{T}_{\mathrm{yy}}$ anomalies is accompanied by stronger westerly wind shear

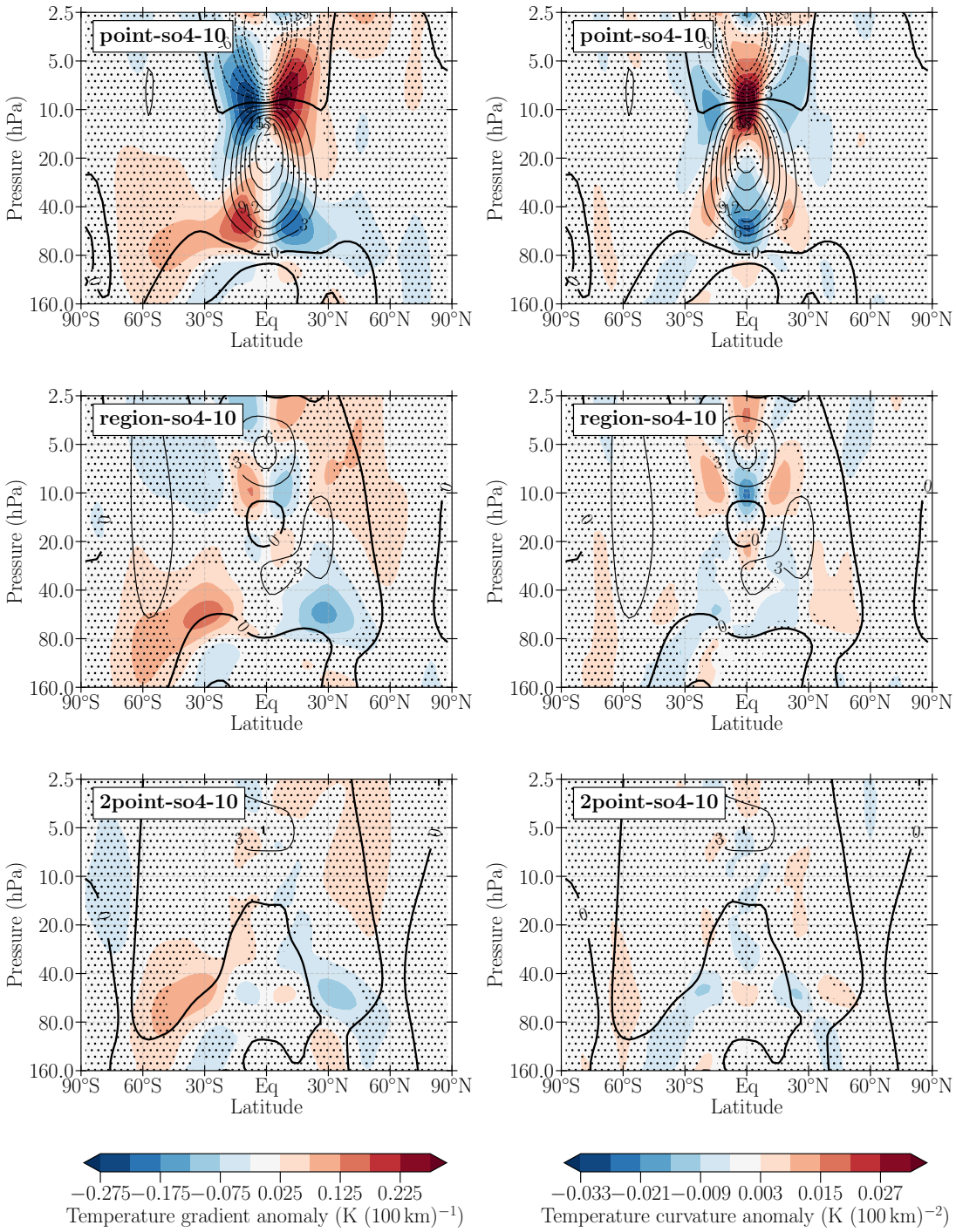

(a) $\Delta\overline{T}_{\mathrm{y}}$ **(b)** $\Delta\overline{T}_{\mathrm{yy}}$

Figure 5.4: Vertical profile of the anomaly of the meridional zonal mean temperature gradient ($\Delta\overline{T}_{\mathrm{y}}$) **(a)**, and the meridional zonal mean temperature curvature ($\Delta\overline{T}_{\mathrm{yy}}$) **(b)**, for injections with an injection rate of 10 Tg(S) yr^{-1}. Note that in **(a)**, a positive $\Delta\overline{T}_{\mathrm{y}}$ in the southern hemisphere is equivalent to a negative $\Delta\overline{T}_{\mathrm{y}}$ in the northern hemisphere, both indicating a weaker poleward gradient. Stippling indicates areas which are not significant at the 95 % level in a student's t-test. Black contour lines show the anomaly of the zonal mean zonal wind speed ($\Delta\overline{u}$) in m s^{-1} with a contour interval of 3 m s^{-1}. The thick solid line denotes $\overline{u} = 0$ m s^{-1}. Solid lines denote a westerly anomaly, dashed lines denote an easterly anomaly. Respective plots for the other injection scenarios can be found in appendix A4.

according to Equation 2.6. For the point injections, the strongest negative anomaly of $\overline{T}_{\mathrm{yy}}$ within the tropics is centered in the injection layer around 60 hPa (Fig. 5.4 b, top). Consequently, the injection layer must be accompanied by constant westerlies on top of it in order to maintain thermal wind balance, which results in the observed constant westerly QBO phase for point-so4-10. Accordingly, the maximum westerly anomaly of the zonal mean zonal wind $\overline{u}$ within the tropics is located directly above the region with westerly shear, where $\overline{T}_{\mathrm{yy}} \approx 0\,\mathrm{K\,km^{-2}}$ (Fig. 5.4 b, top).

Furthermore, the strength of the QBO modification was found to depend clearly on the injection rate and the injection species for the point injections. For the point injection of H_2SO_4 with an injection rate of $25\,\mathrm{Tg(S)\,yr^{-1}}$, i.e. point-so4-25, the modification of the QBO was found to be stronger than for point-so4-10. This is explained by the stronger warming of the lower tropical stratosphere for point-so4-25 (Sec. 5.1), which also results in a stronger and vertically more extended negative anomaly of the tropical (i.e. 5° S to 5° N) mean meridional temperature curvature $\overline{T}_{\mathrm{yy,\,trop}}$ (Fig. 5.5 a, top). Consequently, also the westerly anomaly of the tropical (i.e. 5° S to 5° N) mean zonal wind $\overline{u}_{\mathrm{trop}}$ above the injection layer gets stronger and reaches farther up for point-so4-25 (Fig. 5.5 b, top). On the other hand, for the point injection of H_2SO_4 with an injection rate of $5\,\mathrm{Tg(S)\,yr^{-1}}$, i.e. point-so4-5, the modification of the QBO was found to be weaker This is explained by the weaker warming of the lower stratosphere for point-so4-5. Accordingly, the lower stratospheric anomaly of $\overline{T}_{\mathrm{yy,\,trop}}$ as well as the westerly anomaly of $\overline{u}_{\mathrm{trop}}$ are clearly weaker than for point-so4-10 (Fig. 5.5, top), which explains the weaker modification of the QBO. This is also the explanation for the observed weaker modification of the QBO for a point injection of SO_2 compared to a respective point injection of H_2SO_4. Since the stratospheric warming is weaker for a point injection of SO_2 than for the according point injection of H_2SO_4, the lower stratospheric anomaly of $\overline{T}_{\mathrm{yy,\,trop}}$ and, accordingly, the westerly anomaly of $\overline{u}_{\mathrm{trop}}$ are weaker as well (Fig. 5.5, top).

For the region injections with an injection rate of $10\,\mathrm{Tg(S)\,yr^{-1}}$, i.e. region-so2-10 and region-so4-10, the period of the QBO was found to be clearly prolonged, but it was not locked in a permanent westerly phase like for the point injections of $10\,\mathrm{Tg(S)\,yr^{-1}}$. This is explained by the meridionally more uniform warming of the lower tropical stratosphere for a region injection compared to a point injection, which is visible in Figure 5.2. Therefore, the strongest modifications of $\overline{T}_{\mathrm{y}}$ are located at approximately 30° N and 30° S, while its modifications within the deep tropics are not significant (Fig. 5.4, center). Accordingly, also the negative anomaly of $\overline{T}_{\mathrm{yy}}$ and – following thermal wind balance (Eq. 2.6) – the induced anomaly of westerly shear is weak near the equator. Consequently, the period of the QBO is prolonged in region-so2-10 and region-so4-10, but it is not locked in a permanent westerly phase. This is also

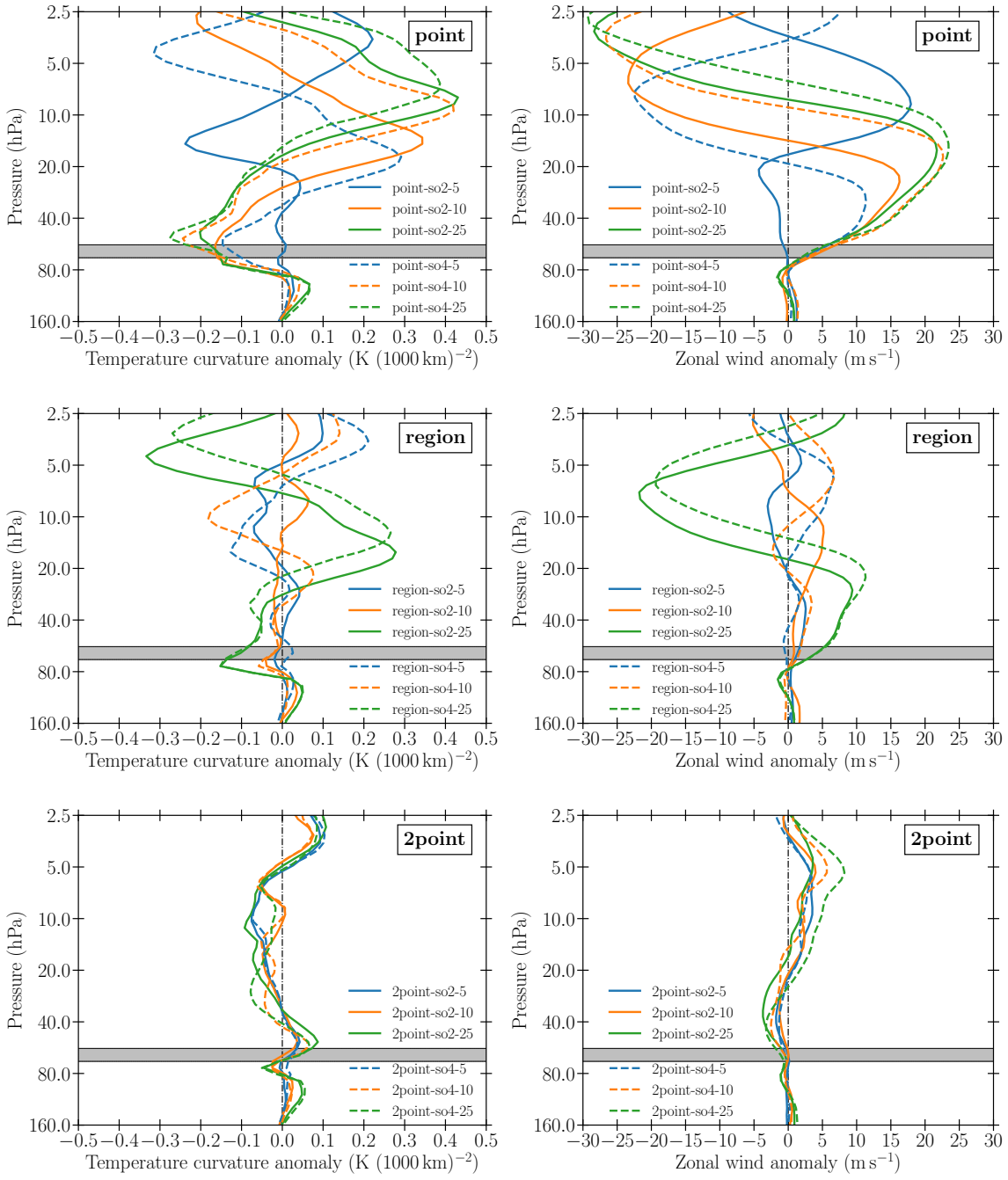

(a) $\Delta\overline{T}_{\mathrm{yy,\,trop}}$ **(b)** $\Delta\overline{u}_{\mathrm{trop}}$

Figure 5.5: Vertical profile of the tropical (i.e. 5° N to 5° S) mean temperature curvature anomaly ($\Delta\overline{T}_{\mathrm{yy,\,trop}}$) **(a)** and the tropical mean zonal wind anomaly ($\Delta\overline{u}_{\mathrm{trop}}$) **(b)** for the point injections **(top)**, the region injections **(center)**, and the 2point injections **(bottom)**. The horizontal grey bar marks the injection layer. The vertical dash-dotted line marks $\Delta\overline{T}_{\mathrm{yy,\,trop}} = 0\,\mathrm{K}\,(100)\,\mathrm{km}^{-2}$ in **(a)** and $\Delta\overline{u}_{\mathrm{trop}} = 0\,\mathrm{m\,s}^{-1}$ in **(b)**.

indicated by the anomaly of $\overline{u}_{\mathrm{trop}}$, which is only slightly positive with values of up to $\overline{u} \approx +3\,\mathrm{m\,s^{-1}}$ between 30 hPa and 40 hPa (Fig. 5.5, center).

For the region injections, the modification of the QBO has been found to depend on the injection rate and the injection species as well, which becomes clearly apparent in Figure 5.5 b (center). For an injection rate of $25\,\mathrm{Tg(S)\,yr^{-1}}$, the observed breakdown of the QBO is indicated by significant westerly anomalies of $\overline{u}_{\mathrm{trop}}$ of approximately $+10\,\mathrm{m\,s^{-1}}$, which are slightly stronger and vertically more extended for an injection of H_2SO_4 than for an injection of SO_2. This is explained by the fact that for region-so2-25 and region-so4-25 the strong modification of $\overline{T}_{\mathrm{y}}$ at approximately 30° S and 30° N reaches far into the deep tropics due to the very strong aerosol-induced warming. Therefore, a significant negative anomaly of $\overline{T}_{\mathrm{yy}}$ emerges at the equator (Fig. 5.5 a, center), which results in the observed breakdown of the QBO. For region-so2-5 and region-so4-5, $\overline{T}_{\mathrm{yy,\,trop}}$ remains nearly unchanged within the tropics (Fig. 5.5 a, center) and, therefore, the westerly anomaly of u_{trop} within the lower tropical stratosphere is only small (Fig. 5.5 b, center). Accordingly, also the period of the QBO has been found to be only weakly prolonged for region-so2-5 and region-so4-5 (Fig. A.7, Fig. A.8).

For the 2point injections with an injection rate of $10\,\mathrm{Tg(S)\,yr^{-1}}$, i.e. 2point-so2-10 and 2point-so4-10, the QBO was not found to be modified significantly and its natural periodicity was found to be basically preserved. This can again – like for the point and region injections – be attributed to the meridional structure of the aerosol-induced stratospheric warming anomaly. Like for the region injections, also for the 2point injections the stratospheric temperature anomaly is meridionally nearly uniform between approximately 30° S and 30° N (Fig. 5.2, bottom). Furthermore, for the 2point injections, the strongest warming of the lower stratosphere is located at approximately 15° S and 15° N. This is in contrast to the other injection scenarios, for which the strongest warming is centered at the equator. Therefore, for 2point-so2-10 and 2point-so4-10, the usually positive poleward meridional temperature gradient in the lower stratosphere is slightly intensified directly within the tropics between approximately 15° S and 15° N compared to contr-000 (Fig. 5.4 a, bottom). Accordingly, $\overline{T}_{\mathrm{yy}}$ has a slightly positive anomaly centered directly at the equator at approximately 50 hPa (Fig. 5.4 b, bottom). This, especially, becomes apparent in Figure 5.5 a (bottom). Following thermal wind balance (Eq. 2.6), the positive anomaly of $\overline{T}_{\mathrm{yy}}$ is accompanied by a weak anomaly of easterly shear within the tropical injection layer, which induces an additional westward component of the zonal mean zonal wind $\overline{u}$ on top of it. This can be clearly seen in Figure 5.5 b (bottom), which shows slight easterly anomalies of $\overline{u}_{\mathrm{trop}}$ above the injection layer for 2point-so4-10.

For the other injection rates, the anomaly of $\overline{T}_{\mathrm{yy,\,trop}}$ is slightly positive above the injection layer for the 2point injections as well (Fig. 5.5 a, bottom), which indicates that this is a generic feature of the 2point injection strategy. However, the magnitude of the anomaly of $\overline{T}_{\mathrm{yy,\,trop}}$ is rather independent of injection rate and species. This is a consequence of the far extratropical injection locations of the 2point injections, which result in a meridionally more or less uniform lower stratospheric temperature anomaly even for high injection rates. Accordingly, also the induced additional westward component of $\overline{u}_{\mathrm{trop}}$ within the lower tropical stratosphere is only slightly stronger for the injections with an injection rate of $25\,\mathrm{Tg(S)\,yr^{-1}}$ than for the ones with an injection rate of $5\,\mathrm{Tg(S)\,yr^{-1}}$ and $10\,\mathrm{Tg(S)\,yr^{-1}}$, as apparent in Figure 5.5 b (bottom). Consequently, the period and strength of the QBO winds remain basically unchanged for the 2point injections with an injection rate of $5\,\mathrm{Tg(S)\,yr^{-1}}$ and $10\,\mathrm{Tg(S)\,yr^{-1}}$ compared to contr-000 (Fig. 5.3, bottom, Fig. A.5, bottom). For the 2point injections with an injection rate of $25\,\mathrm{Tg(S)\,yr^{-1}}$, i.e. 2point-so2-25 and 2point-so4-25, the easterly phase of the QBO within the lower stratosphere is slightly prolonged while the lower stratospheric QBO westerlies are moderately weakened (Fig. A.6, bottom).

5.2.2 Dependency of the QBO response on the injection strategy

The fundamentally different response of the QBO to an aerosol-induced warming of the lower tropical stratosphere for different injection strategies has been clearly linked to the observed temperature anomalies using the tropical thermal wind balance given in Equation 2.6. Thereby, the meridional structure of the aerosol-induced stratospheric temperature anomaly explains the observed QBO response adequately for all three tested injection strategies. Hence, the results of this study explicitly explain the slight prolongation of the QBO easterly phase within the lower stratosphere, which was observed for the 2point injections, as a result of the weaker poleward meridional temperature gradient. This is a clear advancement compared to Tilmes et al. (2018), who did not further investigate the observed QBO modifications for subtropical 2point injections and argued that their short simulation period may be a reason for the observed slight prolongation of the QBO easterly phase within the lower stratosphere. The clear dependency of the QBO modification on the meridional structure of the lower stratospheric temperature anomaly via thermal wind balance may also be useful to explain the significant accelaration of the QBO found by Richter et al. (2017) for extratropical single-point injections at 15° S, 15° N, 30° S, and 30° N. However, due to their different injection strategy compared to those of this study, a clear conclusion of their results based on this study is not possible.

Furthermore, the validity of the approximation of the tropical thermal wind balance given in Equation 2.7 is very limited when comparing the response of the QBO

to different injection strategies. This approximation assumes that the anomaly of the vertical wind shear is directly proportional to the absolute strength of the temperature anomaly. The limited validity of this approximation gets clearly obvious when comparing for example 2point-so4-25 and point-so4-5. For 2point-so4-25, the anomaly of the tropical (i.e. 5° N to 5° S) mean temperature $\overline{T}_{\mathrm{trop}}$ reaches nearly +9 K within the injection layer, while for point-so4-5 it is only approximately +4 K. However, for point-so4-5, the QBO has been found to break down, while for 2point-so4-25 its periodicity remains nearly unchanged. This comparison clearly shows that the modification of the QBO depends on the tropical anomaly of $\overline{T}_{\mathrm{yy}}$, as indicated in Equation 2.6, and not on the tropical anomaly of $\overline{T}$. Therefore, the tropical anomaly of $\overline{T}$ cannot be used as an indicator for the strength of the QBO modification when comparing different injection strategies. This was done for example in Niemeier and Schmidt (2017) to explain the weaker QBO response for an injection into a belt along the equator from 30° S to 30° N compared to a corresponding equatorial point injection. However, within this study it was clearly shown that not the weaker absolute strength of the tropical temperature anomaly but its meridionally more uniform structure is the root cause for the weaker QBO response. Nevertheless, within one specific injection strategy the dependency of the strength of the QBO modification on the injection rate and species can still be approximated by the approximation of the tropical thermal wind balance given in Equation 2.7.

Besides via a disruption of the thermal wind balance, the aerosol-induced warming of the lower tropical stratosphere also modifies the QBO by increasing the tropical upwelling of the BDC (Aquila et al., 2014). A stronger tropical upwelling of the BDC is accompanied by a stronger residual vertical advection of zonal momentum $-\omega^*\overline{u}_{\mathrm{z}}$, which weakens the downwelling of the QBO induced by gravity wave dissipation. Therefore, a stronger tropical upwelling of the BDC prolongs the period of the QBO following Aquila et al. (2014). These results were confirmed by multiple studies, for example Niemeier and Schmidt (2017) or Richter et al. (2017).

However, within this study the tropical mean anomalies of $-\omega^*\overline{u}_{\mathrm{z}}$ are rather small for those injections, for which the QBO was not found to be locked down in a permanent westerly phase (Fig. 5.6). For the 2point injections, this can be attributed to the very small anomaly of the residual vertical velocity ω^* within the tropical pipe due to their extratropical injection locations (see Sec. 5.3). Therefore, also the anomaly of $-\omega^*\overline{u}_{\mathrm{z}}$ is weak within the tropical pipe. This explains why the period of the QBO remains nearly unchanged for the 2point injections even for an injection rate of 25 $\mathrm{Tg(S)\,yr^{-1}}$. For the region injections, the small tropical mean anomalies of $-\omega^*\overline{u}_{\mathrm{z}}$ are a consequence of the data presented in Figure 5.6 being temporal averages. As long as the QBO preserves its oscillating behavior, an increased vertical advection of westerly

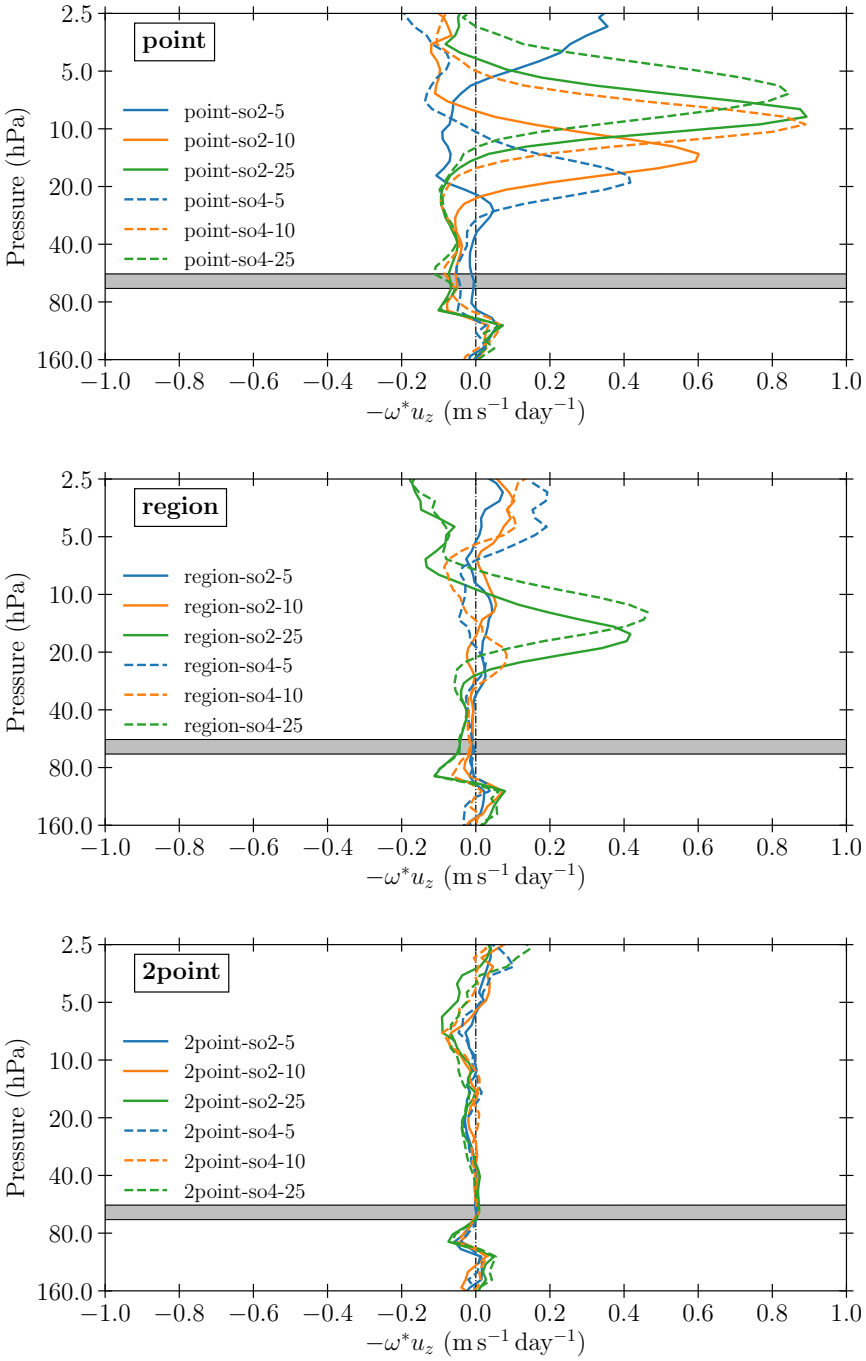

Figure 5.6: Vertical profile of the anomaly of the tropical (i.e. 5° N to 5° S) mean residual vertical advection of zonal momentum ($\Delta(-\omega^*\overline{u}_z)_{\text{trop}}$) for the point injections **(top)**, the region injections **(center)**, and the 2point injections **(bottom)**. The vertical dash-dotted line marks $\Delta(-\omega^*\overline{u}_z)_{\text{trop}} = 0\,\text{m}\,\text{s}^{-1}\,\text{day}^{-1}$.

momentum during a QBO westerly phase is compensated by an increased vertical advection of easterly momentum during a QBO easterly phase within a sufficiently long temporal average, which results in the observed small net anomalies. However, the absolute vertical advection of zonal momentum increases for the region injections, as indicated by positive anomalies of ω^* within the tropical pipe (see Sec. 5.3). For those injections, for which the QBO was found to be locked in a permanent westerly phase, $-\omega^*\overline{u}_z$ has strong positive anomalies in the shear zone between the lower stratospheric westerlies and the upper stratospheric easterlies. The maximum of these positive anomalies is located at the height of $\overline{u}_{\text{trop}} \approx 0\,\text{m}\,\text{s}^{-1}$ (Fig. 5.5 b). The strength of the anomaly of $-\omega^*\overline{u}_z$ clearly corresponds to the strength of the QBO westerly anomaly. Consequently, in the case of a completely disrupted QBO with constant westerlies in the lower tropical stratosphere, the intensified vertical advection of westerly momentum supports these westerlies against the downwelling wave-induced QBO easterlies and enhances their vertical extent.

5.3 Modification of the BDC

Besides modifying the QBO, the aerosol-induced warming of the lower tropical stratosphere also results in an intensification of the tropical upwelling within the tropical pipe, which subsequently accelerates the whole BDC due to continuity. This is clearly visible in Figure 5.7 for the experiments with an injection rate of $10\,\text{Tg(S)}\,\text{yr}^{-1}$. The anomaly of the residual mass stream function χ^* clearly indicates an intensification of the BDC for all three injection strategies and for both injection species. The intensification of the BDC is accompanied by slightly positive anomalies of $\overline{\omega^*}$ within the tropics and subtropics and slightly negative anomalies of $\overline{\omega^*}$ within the mid-latitudes and polar regions. However, there are substantial differences between the different injection strategies regarding the strength and the spatial structure of the intensification of the BDC and the accompanied anomalies of $\overline{\omega^*}$.

For the point injections, the BDC clearly shows the strongest intensification of all three injection scenarios. Within the tropical pipe, $\overline{\omega^*}$ increases statistically significantly by up to $0.62\,\text{mm}\,\text{s}^{-1}$ for point-so4-10 and $0.44\,\text{mm}\,\text{s}^{-1}$ for point-so2-10. Vertically, the positive anomalies of $\overline{\omega^*}$ extend approximately from 50 hPa up to 5 hPa, with the maximum being located in the middle stratosphere approximately between 15 hPa and 10 hPa, which is the region of strongest wind shear. The anomaly of χ^* exhibits a predominantly vertical orientation, which clearly indicates that most of the additional meridional mass transport of the BDC happens via its upper branch above the subtropical transport barriers. The accompanied negative anomalies of $\overline{\omega^*}$

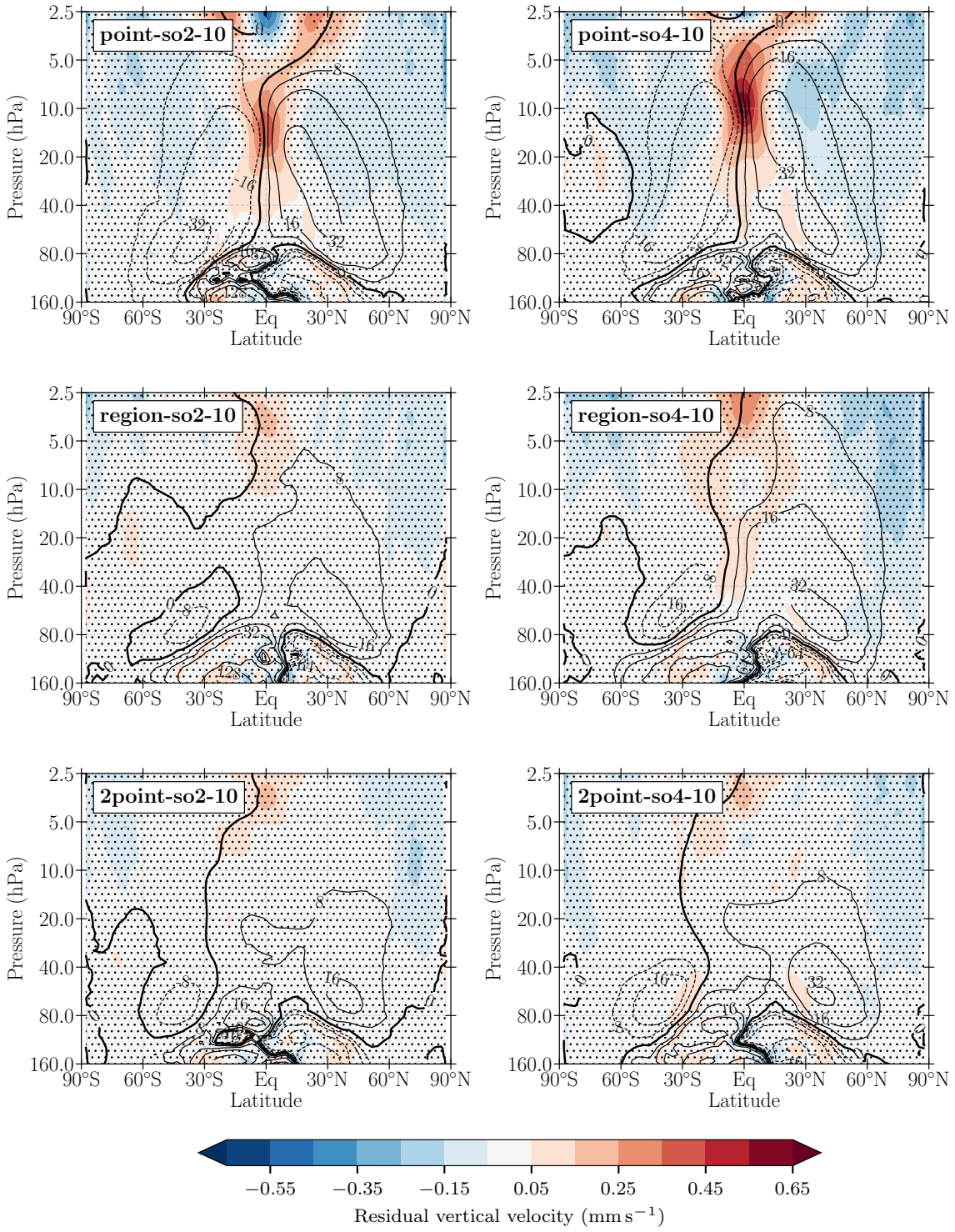

Figure 5.7: Vertical profile of the anomaly of the zonal mean residual vertical velocity ($\Delta\omega^*$) for injections with an injection rate of 10 Tg(S) yr^{-1}. Stippling indicates areas for which $\Delta\omega^*$ is not significant at the 95 % level in a student's t-test. Black contour lines indicate the anomaly of the residual mass stream function ($\Delta\chi^*$) in kg s^{-1} with contour intervals increasing by powers of two. The thick black line denotes $\Delta\chi^* = 0$ kg s^{-1}. Solid lines indicate a clockwise circulation anomaly, dashed lines indicate an anticlockwise circulation anomaly. The respective plots for injections with an injection rate of 5 Tg(S) yr^{-1} and 25 Tg(S) yr^{-1} can be found in appendix A5.

outside of the tropical pipe are mostly not statistically significant at the 95 % level in a student's t-test.

For the region and the 2point injections the modification of the BDC is clearly weaker than for the point injections (Fig. 5.7, center, Fig. 5.7, bottom). Larger connected areas of positive anomalies of $\overline{\omega^*}$ can only be found in the upper tropical stratosphere above $\sim 10\,\mathrm{hPa}$, but are, however, not statistically significant. In the middle and the lower tropical stratosphere, the positive anomalies of $\overline{\omega^*}$ are very small, especially for an injection of SO_2. For an injection of H_2SO_4, small areas of statistically significant positive anomalies of $\overline{\omega^*}$ are apparent: For region-so4-10, $\overline{\omega^*}$ increases statistically significantly by $\sim 0.1\,\mathrm{mm\,s^{-1}}$ between 50 hPa and 20 hPa within the deep tropics. For 2point-so4-10, $\overline{\omega^*}$ increases statistically significantly by $\sim 0.1\,\mathrm{mm\,s^{-1}}$ between 80 hPa and 40 hPa at approximately 30° S and 30° N. The negative anomalies of $\overline{\omega^*}$ outside of the tropics are not statistically significant. Furthermore, the modification of the BDC is mostly restricted to the lower stratosphere below $\sim 40\,\mathrm{hPa}$, as indicated by the anomalies of χ^*. Consequently, most of the additional meridional mass transport of the BDC happens via its lower branch below the subtropical transport barriers. These observations also hold true for the experiments with an injection rate of $5\,\mathrm{Tg(S)\,yr^{-1}}$ and $25\,\mathrm{Tg(S)\,yr^{-1}}$. The respective plots for these experiments can be found in appendix A5.

Obviously, the increase of $\overline{\omega^*}$ within the tropical pipe and the accompanied modification of the whole BDC strongly depends on the injection strategy. This can be explained by splitting up the increase of the tropical upwelling into two parts: A direct and an indirect one. The direct acceleration of the tropical upwelling of the BDC is the thermodynamic response to a warming of the lower stratosphere, which is associated with an implementation of SAM (Aquila et al., 2014; Richter et al., 2017). As described in Section 2.3, in steady-state conditions the diabatic heating anomaly caused by the aerosols must be balanced by an increase of adiabatic cooling (Eq. 2.4). Following Equation 2.4, for a constant stable stratification an increase of adiabatic cooling can only be achieved via an increase of ω^*. Consequently, the resulting increase of $\overline{\omega^*}$ is more or less strongly coupled to the respective regions of the strongest aerosol-induced warming, which are located in the lower stratosphere between 40 hPa and 80 hPa (Fig. 5.2). However, due to continuity it does also extend farther up (Holloway and Neelin, 2007; Garfinkel et al., 2013). This mechanism explains the weak but statistically significant anomalies of $\overline{\omega^*}$ observed in the lower stratosphere at $\sim 40\,\mathrm{hPa}$ (Fig. 5.7). For the point and region injections, the strongest lower stratospheric warming was found to be centered at the equator (Fig. 5.2) and, accordingly, also the strongest increase of $\overline{\omega^*}$ is located in the deep tropics for point-so2-10, point-so4-10, and region-so4-10. For 2point-so4-10, the strongest increase of $\overline{\omega^*}$ within the

lower stratosphere is located at approximately 30° S and 30° N, which coincides with the location of the strongest lower stratospheric warming. Furthermore, this is in accordance with the almost unmodified period of the QBO observed for the 2point injections (Sec. 5.2): Since the anomalies of $\overline{\omega^*}$ are strongest at approximately 30° N and 30° S but weak at the equator, the anomaly of the vertical advection of zonal momentum by $\overline{\omega^*}$ is also weak within the deep tropics. Therefore, the QBO as an equatorial system is not modified significantly and basically maintains its natural period despite sulfur injections. Implicitly, this means that the direct strengthening of the tropical upwelling is the main mechanism which weakens the downward propagation of the QBO and prolongs its period for the point and region injections as explained in Section 5.2.2.

However, the direct thermodynamic acceleration of the tropical upwelling cannot account for the strong increase of $\overline{\omega^*}$ in the middle stratosphere observed in point-so2-10 and point so4-10, since the increase of $\overline{\omega^*}$ is not accompanied by corresponding diabatic heating anomalies (Fig. 5.1 top, Fig. 5.7 top). These anomalies of $\overline{\omega^*}$ are caused by the so-called indirect acceleration of the tropical upwelling, which is a result of a modification of the SMC coupled to the QBO. For point-so2-10 and point-so4-10, the QBO was found to be locked in a permanent phase of strong westerlies (Fig. 5.3). According to Plumb and Bell (1982), a westerly phase of the QBO is accompanied by a SMC consisting of tropical upwelling and subtropical downwelling, both centered in the middle stratosphere at $\sim 15\,\mathrm{hPa}$. Consequently, for point-so2-10 and point-so4-10 the SMC is locked in a state of permanent and strong tropical upwelling. This increases the general tropical upwelling between 50 hPa to 5 hPa significantly, as observed in Figure 5.7.

The indirect acceleration of the tropical upwelling can be observed in all experiments, in which the sulfur injections result in a breakdown of the QBO (Fig. 5.8). For all experiments with a broke-down QBO (i.e. all point injections apart from point-so2-5 as well as region-so2-25 and region-so4-25), the tropical (i.e. 5° N to 5° S) mean residual vertical velocity $\overline{\omega^*}_{\mathrm{trop}}$ exhibits significant positive anomalies in the middle stratosphere of up to $0.8\,\mathrm{mm\,s^{-1}}$ for point-so4-25. Since the strength of the induced permanent westerlies depends on the strength of the lower stratospheric temperature anomaly (Sec. 5.2.1), the indirect acceleration of the tropical upwelling is clearly stronger for higher injection rates as well as for an injection of H_2SO_4 compared to a respective injection of SO_2 (Fig. 5.8).

In contrast, the direct thermodynamic increase of $\overline{\omega^*}_{\mathrm{trop}}$ in the lower stratosphere as a response to the aerosol-induced warming leads to anomalies of only up to $0.1\,\mathrm{mm\,s^{-1}}$. Therefore, the direct thermodynamic acceleration of the tropical upwelling and the indirect acceleration of the tropical upwelling via the SMC coupled to the QBO

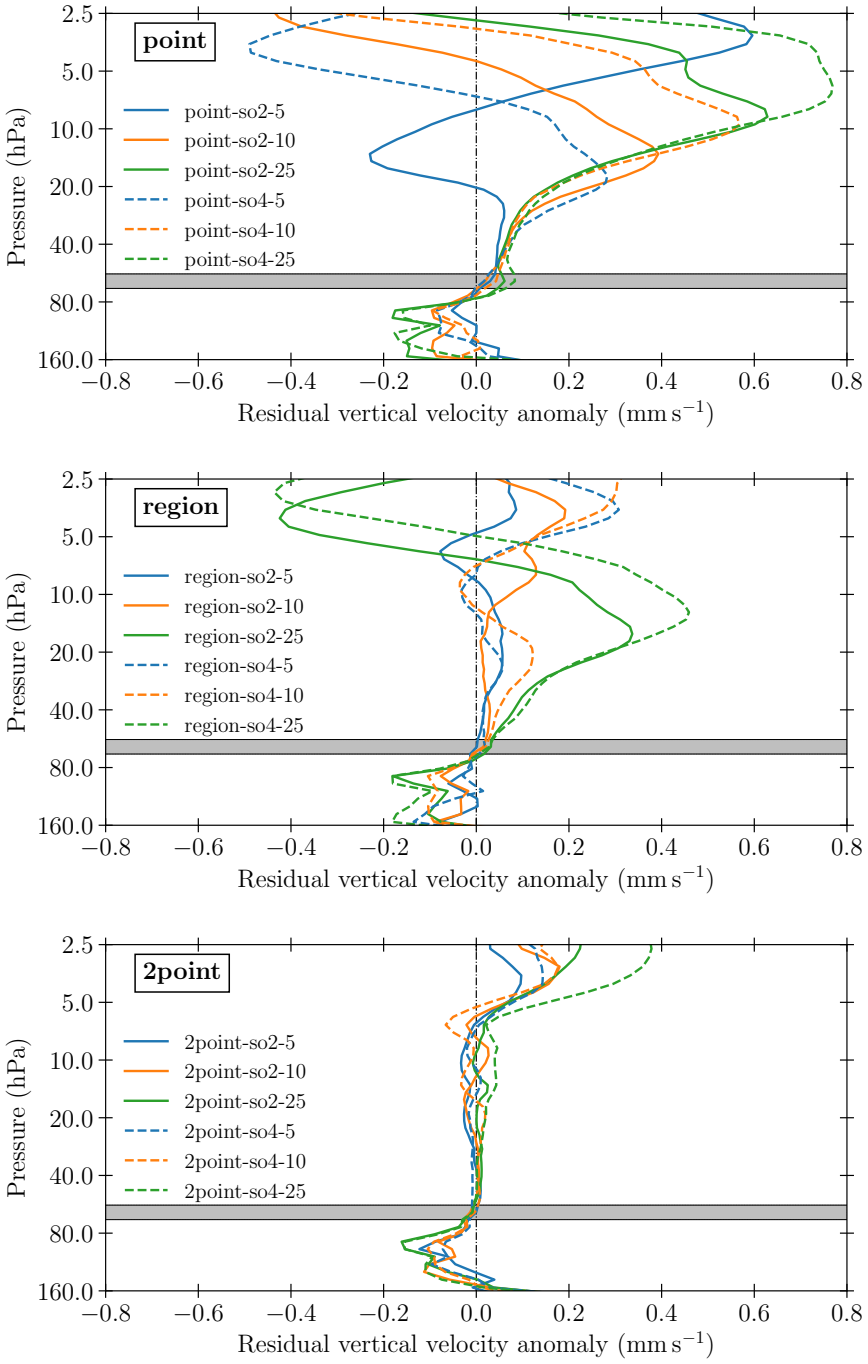

Figure 5.8: Vertical profile of the tropical (i.e. 5° N to 5° S) mean residual vertical velocity anomaly, $\Delta\omega^*_{\text{trop}}$, for the point injections **(top)**, the region injections **(center)**, and the 2point injections **(bottom)**. The horizontal grey bar marks the injection layer. The vertical dashed-dotted line marks $\Delta\omega^*_{\text{trop}} = 0\,\text{mm}\,\text{s}^{-1}$.

are clearly distinguishable from each other. This gets clearly evident for the region injections (Fig. 5.8 b).

Furthermore, also the direct thermodynamic increase of $\overline{\omega^*}$ exhibits a clear dependency on the injection rate and species. For a higher injection rate as well as for an injection of H_2SO_4 instead of an injection of SO_2, the direct increase of $\overline{\omega^*}$ is slightly stronger (Fig. 5.7, Fig. A.12, Fig. A.13). This can be explained using Equation 2.4, which states that a stronger lower stratospheric temperature anomaly also results in a larger anomaly of $\overline{\omega^*}$ given an approximately constant vertical temperature gradient. The direct and indirect acceleration of the tropical upwelling result in a significant increase of $\overline{\omega^*}$ within the tropical pipe. Due to continuity (Eq. 2.3), this increase results in the observed speed up of the whole BDC, which is indicated by the anomalies of the residual mass stream function χ^*. However, the accompanied anomalies of the residual vertical motions are not balanced by an aerosol-induced diabatic heating apart from within the aerosol layer. Following Equation 2.2 and setting $\overline{Q} = 0\,\mathrm{J\,s^{-1}\,kg^{-1}}$, a positive anomaly of $\overline{\omega^*}$ results in a negative adiabatic temperature anomaly and vice versa. This explains the significant negative temperature anomalies in the middle and upper tropical stratosphere, which have been observed especially in the experiments with a broke-down QBO (Fig. 5.2, Fig. A.3, Fig. A.4). In the extratropical and polar stratosphere the increased downwelling of the BDC explains the positive temperature anomalies in these regions. However, these positive anomalies are mostly not statistically significant due to the high natural variability within the respective regions.

5.4 Dynamical feedback on the sulfate distribution

The meridional and vertical transport of artificial sulfate aerosols within the stratosphere is an important parameter with regard to their stratospheric lifetime and, consequently, the achievable radiative forcing during an implementation of SAM. However, due to the modification of the QBO and the BDC caused by the aerosol-induced warming of the lower stratosphere, the stratospheric transport patterns of artificial sulfate aerosols are significantly altered. For instance, Niemeier et al. (2011) or Niemeier and Schmidt (2017) showed for an injection of SO_2 that especially the strengthening of the tropical upwelling significantly increases the stratospheric lifetime of artificial sulfate particles. This dynamical increase of the stratospheric sulfate lifetime is commonly referred to as the dynamical feedback of SAM. The dynamical feedback of SAM has been also found in the experiments performed within this study, as shown in Figure 5.9 for tropical (i.e. 5° N to 5° S) mean conditions. Within the SAM experiments, the increased residual vertical velocity ω^* compensates for a larger

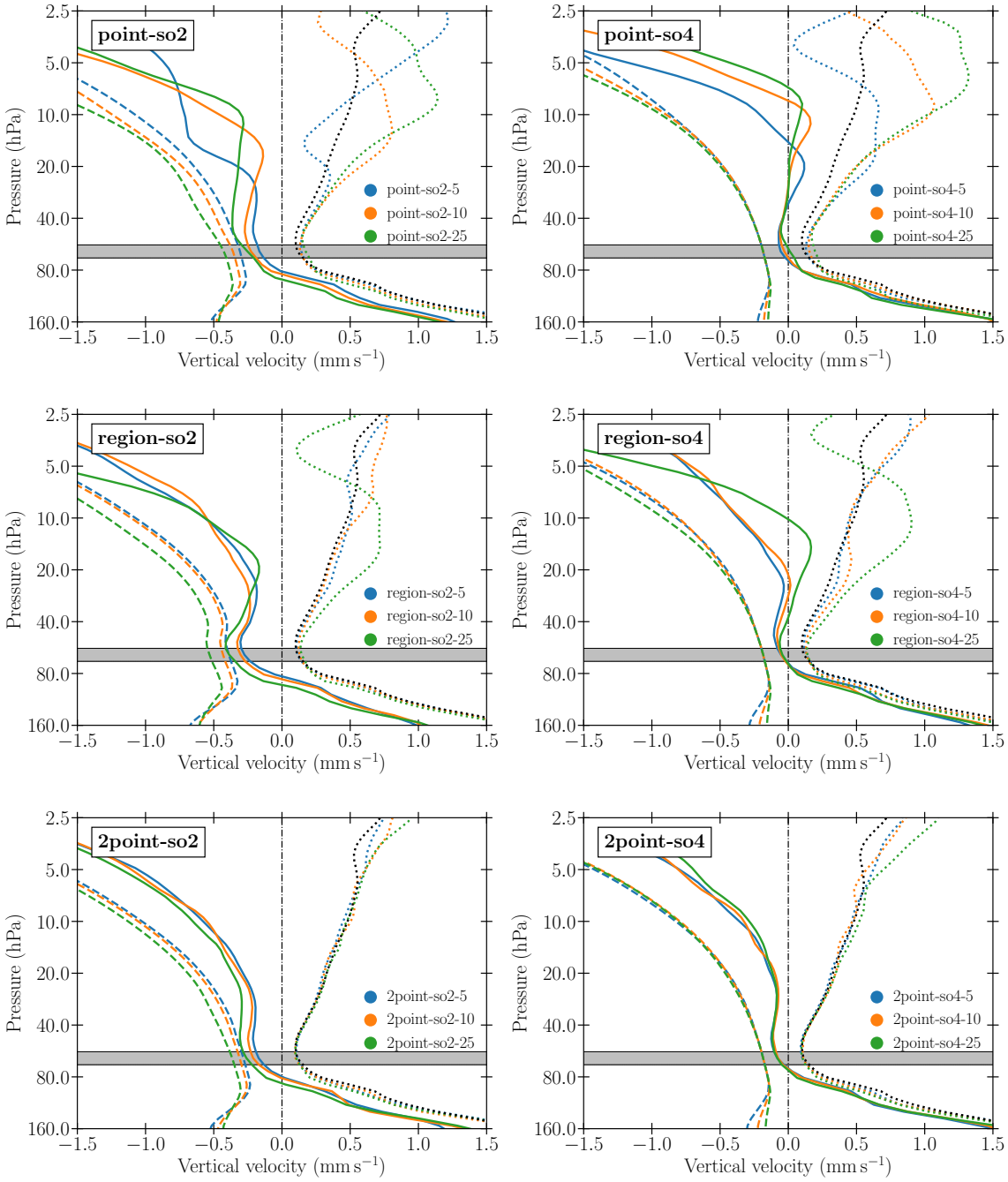

Figure 5.9: Vertical profile of the tropical (i.e. between 5° N and 5° S) mean net vertical velocity ω_{net} of CS-SO_4 particles (solid), the tropical mean sedimentation velocity v_{t} of CS-SO_4 particles (dashed), and the tropical mean residual vertical velocity ω^*_{trop} (dotted) as a function of injection rate. The dotted black line represents ω^*_{trop} of contr-000. The horizontal grey bar marks the injection layer. The vertical dashed-dotted line marks $\omega = 0\,\text{mm}\,\text{s}^{-1}$.

fraction of the sedimentation velocity v_t than within contr-000. Therefore, the net vertical velocity ω_{net} of the sulfate particles, which is the sum of ω^* and v_t, increases, indicating a slower downward movement. This holds true for both injection species, SO_2 as well as H_2SO_4. However, sedimentation is significantly weaker for an injection of H_2SO_4 compared to an injection of SO_2 due to the resulting CS-SO_4 particles staying overall smaller (Sec. 4.1). Therefore, also the net downward movement of the sulfate particles is significantly weaker for an injection of H_2SO_4 than for an injection of SO_2 for all injection strategies. For some point and region injections, ω_{net} is even slightly positive in the middle stratosphere, indicating a net upward movement of the sulfate particles.

For an increasing injection rate, the net vertical movement of the sulfate particles exhibits fundamental differences between an injection of SO_2 and an injection of H_2SO_4. These differences result in a significantly different behavior of the stratospheric lifetime for an increasing injection rate between both injection species (Fig. 5.9). For an injection of SO_2, the sedimentation velocity increases with injection rate for all three injection strategies due to an increasing particle size. In the middle and upper stratosphere above $\sim 25\,\text{hPa}$, this increase of sedimentation is roughly balanced by the increase of ω^* for the point and region injections, resulting in a weak dependency of ω_{net} on the injection rate. In the lower stratosphere between the injection layer and $\sim 25\,\text{hPa}$, ω^* is nearly independent of the injection rate and, therefore, cannot account for the increase of sedimentation. This holds true for the 2point injections throughout the whole stratosphere. Consequently, ω_{net} slightly decreases with injection rate.

For an injection of H_2SO_4, the sedimentation velocity is nearly independent of the injection rate due to an approximately constant particle size, especially within the lower stratosphere. Therefore, the increase of ω^* with increasing injection rate, especially in the middle and upper stratosphere, results in an increase of ω_{net} with injection rate for the point and region injections. For the 2point injections, also ω^* is nearly independent of the injection rate, which causes an approximately constant ω_{net} for all injection rates. Furthermore, ω_{net} gets increasingly positive for higher injection rates throughout more and more layers for the point and region injections. Consequently, for these injection strategies, the sulfate aerosols are lifted increasingly farther up for higher injection rates, which is shown in Figure 5.10 (right panel) for the point injections of H_2SO_4: With increasing injection rate, the height of the sulfate aerosol cloud, which is represented by the zonal mean sulfate mass mixing ratio $\overline{m}_{SO4}$, clearly increases within the tropical pipe and even exceeds the 5 hPa level for point-so4-25. It is clearly visible that $\overline{m}_{SO4}$ coincides with ω_{net}, which gets increasingly positive throughout the tropical pipe for an increasing injection rate. In contrast, for an in-

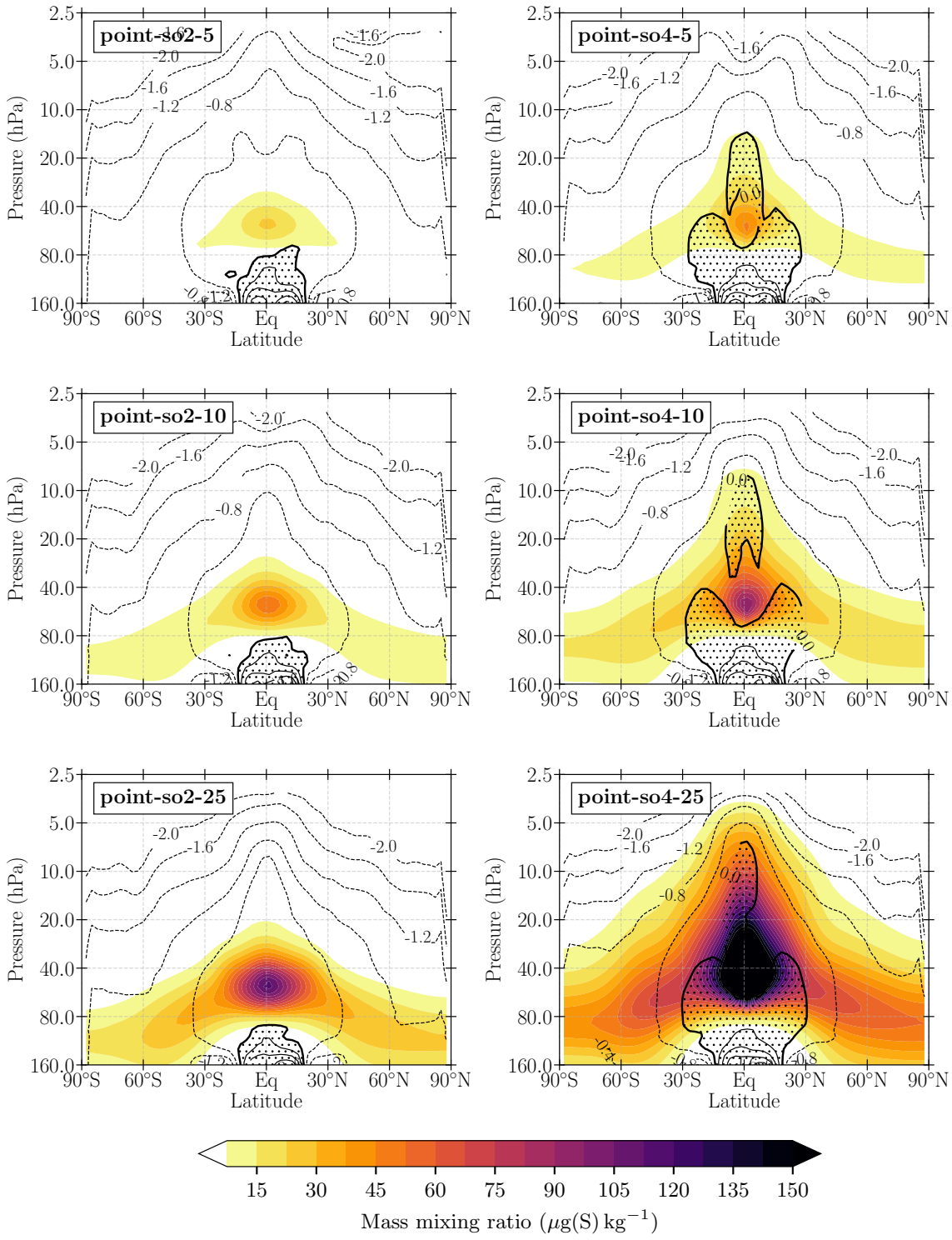

Figure 5.10: Vertical profile of the zonal mean SO_4 mass mixing ratio $\overline{m}_{SO4}$ for the point injections. Black contour lines indicate the zonal mean net vertical velocity $\overline{\omega}_{net}$ of the CS-SO_4 particles in $mm\,s^{-1}$ with a contour interval of $0.4\,mm\,s^{-1}$. Dashed lines indicate a negative $\overline{\omega}_{net}$ (i.e. a net downward movement), while solid lines indicate a positive $\overline{\omega}_{net}$ (i.e. a net upward movement). Regions with a net upward movement are further highlighted by stippling. The respective plots for the region and the 2point injections can be found in appendix A6.

jection of SO_2 ω_{net} is negative throughout the whole tropical pipe for all injection rates. Accordingly, the sulfate aerosols are not transported upward and stay within the injection layer for all injection rates.

This has a significant impact on the stratospheric lifetime of the sulfate aerosols (Fig. 4.5). For an injection of H_2SO_4, the increasing upward transport of the sulfate particles significantly increases their stratospheric lifetime for an increasing injection rate, which holds true for all three injection strategies. This further explains the superlinear increase of the stratospheric sulfate burden M_{SO4} observed for injections of H_2SO_4 (Fig. 4.2). In contrast, for an injection of SO_2 the stratospheric sulfate lifetime stays approximately constant or slightly decreases with increasing injection rate for all three injection strategies, which is explained by the observed independence of ω_{net} on the injection rate. Consequently, the stratospheric sulfate burden increases approximately linearly with injection rate.

Besides increasing the global stratospheric sulfate lifetime, the strengthening of the BDC also results in a stronger tropical confinement of the sulfate aerosols (Niemeier and Schmidt, 2017). The tropical confinement is further increased for higher injection rates. This is clearly indicated by the relative zonal mean sulfate burden for all three injection strategies and both injection species (Fig. 5.11). The relative zonal mean sulfate burden is the quotient of the zonal mean sulfate burden $\overline{M}_{\text{SO4}}$ and the global mean sulfate burden M_{SO4}. In between of 30° N and 30° S the sulfate burden, relatively speaking, slightly increases with increasing injection rate, especially for the H_2SO_4 injections. Poleward of approximately 30° S and 30° N it, relatively speaking, decreases with increasing injection rate. For the point and region injections the tropical confinement of the sulfate aerosols is stronger for an injection of H_2SO_4 than for an injection of SO_2. This is indicated by the equatorial values of the relative zonal mean sulfate burden: For instance, for point-so4-25 it is 176 %, while for point-so2-25 it is only 144 %, and for region-so4-25 it is 125 %, while for region-so2-25 it is only 119 %.

The increasingly stronger tropical confinement is caused by equatorward transport anomalies of the BDC within the lower stratosphere, which get stronger with increasing injection rate. As illustrated by the anomalies of the zonal mean residual mass stream function χ^* for the injections with an injection rate of $10\,\text{Tg(S)}\,\text{yr}^{-1}$ (Fig. 5.7), the transport into the tropical pipe is clearly enhanced at $\sim 80\,\text{hPa}$ and 30° S and 30° N for all three injection strategies and for both injection species. Consequently, the usually poleward meridional transport of sulfate aerosols within the lower branch of the BDC is weakened. This is also the case for the injections with an injection rate of $5\,\text{Tg(S)}\,\text{yr}^{-1}$ and $25\,\text{Tg(S)}\,\text{yr}^{-1}$ (Fig. A.12, Fig. A.13). Furthermore, also the stronger upwelling within the tropical pipe itself strengthens the tropical confinement

of the sulfate particles since it enhances their tropical residence time by transporting them into the middle stratosphere, where the meridional transport is weak due to the subtropical transport barriers.

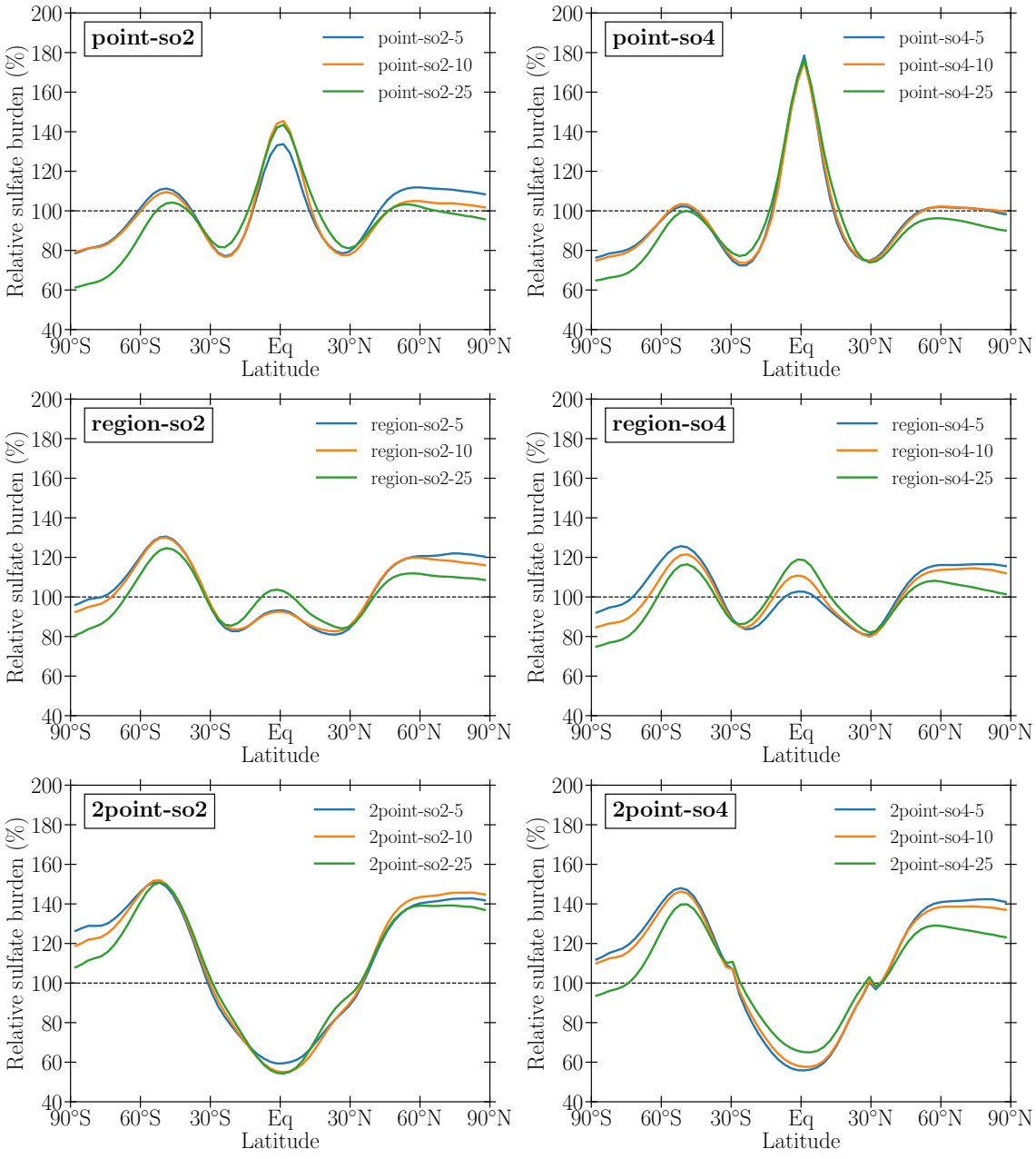

Figure 5.11: Zonal mean stratospheric sulfate burden $\overline{M}_{\mathrm{SO4}}$ relative to the global mean sulfate burden M_{SO4} for different injection rates.

6 Potential, Limits, and Concerns of Different SAM Setups

Within this study, the stratospheric injection of SO_2 and the stratospheric injection of H_2SO_4, which was modeled as the stratospheric injection of AS-SO_4, have been compared comprehensively with regard to their aerosol microphysical and radiative properties. The results of this comparison clearly show that an injection of H_2SO_4 is advantageous compared to an injection of SO_2 from a radiative forcing efficiency standpoint, especially for high injection rates. This basically confirms the results of earlier studies by Pierce et al. (2010), Benduhn et al. (2016), and Vattioni et al. (2019). Due to an on average significantly smaller sulfate particle size, an injection of H_2SO_4 leads to a 43 % to 134 % times higher artificial sulfate burden and a 50 % to 266 % stronger artificial aerosol radiative forcing than a respective injection of SO_2 for all tested injection scenarios. Since in contrast to an injection of SO_2 the average size of the resulting sulfate particles has been further found to be nearly independent of the injection rate for an injection of H_2SO_4, also the radiative forcing efficiency stays constant with injection rate for an injection of H_2SO_4, while it increases for an injection of SO_2.

Therefore, the sulfur mass which would be necessary to counteract a given anthropogenic GHG forcing would be significantly lower when injecting H_2SO_4 instead of SO_2, especially when counteracting high forcings. For instance, counteracting a radiative forcing of $4.0\,\mathrm{W\,m^{-2}}$, as it is proposed in the experiment *G6sulfur* (Kravitz et al., 2015), would require a point injection of $\sim 9\,\mathrm{Tg(S)\,yr^{-1}}$ in the form of H_2SO_4, but $\sim 29\,\mathrm{Tg(S)\,yr^{-1}}$ in the form of SO_2. This corresponds to a stratospheric sulfate burden of approximately 10 Tg(S) and 18.5 Tg(S), respectively. Since the strength of the aerosol-induced warming of the lower stratosphere and the accompanied modification of the QBO and the BDC have been found to clearly depend on the absolute stratospheric sulfate burden, these negative side effects are expected to be also significantly weaker when injecting H_2SO_4 instead of SO_2. Accordingly, in the given example of counteracting a radiative forcing of $4.0\,\mathrm{W\,m^{-2}}$ the injection of H_2SO_4 would result in an anomaly of the tropical (i.e. between 5° N and 5° S) mean temperature T_{trop} of $\sim 8\,\mathrm{K}$ directly above the injection layer. In contrast, the injection of SO_2 would result in an anomaly of T_{trop} of well above 12 K. Following Vattioni et al. (2019), also other potential negative side effects of SAM, which were not considered within this study, would be smaller for an injection of H_2SO_4 than for an injection

of SO_2, when normalized to a given radiative forcing. This includes the depletion of stratospheric methane and ozone as well as the increase of stratospheric water vapor. Therefore, an injection of H_2SO_4 would be potentially preferable over an injection of SO_2, especially in scenarios where the counteraction of strong radiative forcings may be necessary.

Furthermore, the sulfur transportation into the stratosphere would be logistically much more challenging for an injection of SO_2 instead of H_2SO_4 due to the significantly higher injection rates, which would be necessary to counteract a given radiative forcing. In contrast, the transportation of H_2SO_4 inside an airplane would be technically more demanding than the one of SO_2 and is less effective due to the larger mass of a H_2SO_4 molecule compared to a SO_2 molecule. This implies that delivering costs of a H_2SO_4 injection would not be reduced by the same factor as the injected sulfur mass. In the considered example of counteracting a radiative forcing of $4.0\,\mathrm{W\,m^{-2}}$ by SAM, injecting H_2SO_4 instead of SO_2 would reduce the required sulfur mass by approx. 67 %, while the total mass which has to be transported into the stratosphere would only reduce by about 53 %. Therefore, producing H_2SO_4 out of elemental sulfur onboard an aircraft is discussed as a potential alternative, for instance by Smith et al. (2018). However, they found that conversion rates larger than 70 % would be hard to reach and the remainder would be released as SO_2. Consequently, the significantly higher radiative forcing efficiency of a H_2SO_4 injection found in this study may be impossible to reach in reality. However, Smith et al. (2018) found that the production of SO_2 or H_2SO_4 onboard an aircraft could still – all else equal – roughly halve the absolute delivering costs for counteracting a given radiative forcing. Nevertheless, additional research on a safe and efficient technology for providing H_2SO_4 for stratospheric injections is urgently needed.

The results of this study further show that the impact of the dynamical feedback, which results out of the lower stratospheric warming, significantly depends on the injection species when increasing the injection rate. For an injection of H_2SO_4, the dynamical feedback was found to increase the sulfate aerosol lifetime with increasing injection rate, while for an injection of SO_2 the sulfate aerosol lifetime was found to stay almost constant with increasing injection rate. This might be another advantage of an H_2SO_4 injection since it would additionally reduce the amount of injected sulfur, which would be necessary in high forcing scenarios. However, for the point and the region injections the dynamical feedback was also found to result in a clearly stronger tropical confinement for an injection of H_2SO_4 than for an injection of SO_2, even when normalized to a given radiative forcing. Since a meridionally uniform cooling is clearly desirable in order to minimize potentially negative side effects on atmospheric dynamics and potential socio-economic conflict sources resulting from

an over- or undercooling of the tropics, a stronger tropical confinement of the sulfate particles is unfavorable. Therefore, the stronger tropical confinement compared to an injection of SO_2 is a substantial shortcoming of an injection of H_2SO_4. A significantly more uniform radiative forcing is also the reason, why a region injection might be beneficial compared to the point and 2point injections, despite an approx. $0.05\,\mathrm{W\,m^{-2}(Tg(S)\,yr^{-1})^{-1}}$ lower global mean radiative forcing efficiency compared to the point injection.

With regard to a potential adverse modification of the QBO, a 2point injection would be clearly preferable over the point and region injections based on the results of this study. Even for a high injection rate of $25\,\mathrm{Tg(S)\,yr^{-1}}$, the QBO remains nearly unmodified, which was shown to be a direct consequence of the meridional nearly uniform aerosol-induced temperature anomaly. Since the QBO has an impact on the extratropical stratospheric circulation and the polar vortex (Holton and Tan, 1980) as well as on tropospheric winds (Garfinkel and Hartmann, 2011) and precipitation (Seo et al., 2013), its modification by SAM would potentially also modify the surface climate significantly and should, therefore, be avoided.

To conclude, the results of this study may favor an injection of H_2SO_4 over an injection of SO_2, while a clearly preferable injection strategy was not identified. However, an explicit and overarching answer to the question which injection setup might be favorable for a deployment of SAM is not possible. It strongly depends on the desired specific goal of SAM as well as on the individual degree of willingness to accept potential negative side effects of a given injection setup. Therefore, multiple individual answers to this question may exist. A detailed answer would further imply a comprehensive cost risk analysis of each injection setup, which would go beyond the scope of this study.

Additionally, regardless of the injection strategy, the injection species, and the overall injection setup, the implementation of SAM would cause substantial adverse environmental changes. The reduction of ISR would result in less evaporation, which would slow down the hydrological cycle and reduce precipitation significantly. For instance, Schmidt et al. (2012) estimated the global mean precipitation reduction per reduced TOA SW forcing to be approx. $0.035\,\mathrm{mm\,day^{-1}\,(W\,m^{-2})^{-1}}$ within their multi-model ensemble, assuming a linear dependency. Within their study, this would overcompensate the reduced evaporation over many continental areas, indicating increasing dryness. Niemeier et al. (2013) found even larger values for SAM experiments and, furthermore, drastic local changes of precipitation patterns. This would have significant impacts on crop growth, which could potentially risk the food security of millions of people. Furthermore, the reduction of the total ISR in combination with an increased fraction of diffuse radiation may have additional impacts on crops and

natural vegetation, a concern which was for example presented by Robock et al. (2008).

The adverse side effects of SAM such as the aridification of continental areas could be mitigated by choosing an adequate injection strategy. As shown within this study, for example the slowdown and disappearance of the QBO could be prevented by using the 2point injection strategy, while the region injections would prevent a so-called tropical over- or undercooling. Another prominent strategy to reduce adverse side effects to the physical climate system was presented by Kravitz et al. (2017). They used an algorithm for calculating the yearly injection rates at four different injection points (30° S, 15° S, 15° N, and 30° N), which would be necessary to maintain three different climate objectives on a baseline level: The global mean surface air temperature, the interhemispheric surface air temperature gradient, and the equator-to-pole air temperature gradient. After each year, the injection rate at each injection location is adjusted in order to maintain these climate objectives. They showed that this setup would significantly mitigate the aridification of continental area and result in a meridionally more uniform surface cooling compared to equatorial point injections (Kravitz et al., 2019). The QBO was not altered within their experiments as well, which can be explained by thermal wind balance based on the results of this study.

Besides its technical and environmental risks, especially societal and governmental issues have been raised as major concerns against SAM, for example by Robock et al. (2008) and Pierrehumbert (2019). Currently, the civil implementation of SAM is not adequately regulated by international law and liability rules (Saxler et al., 2015). Therefore, a single person, company, or state may be currently able to conduct stratospheric sulfur injections (Niemeier and Tilmes, 2017). However, since an implementation of SAM would always have a global impact on climate, the establishment of international governance of SAM is essential in order to prevent international conflicts or, in a worst case scenario, climate wars. Even if the global community would create the legal bases which would allow for a coordinated implementation of SAM, a global consensus of the desired degree of cooling by SAM has to be achieved. Given the uneven distribution of benefits and negative consequences of global warming as well as SAM, this is more than questionable. For example, it is very likely that one state wants to achieve a lower global mean temperature by the implementation of SAM than another one, which is another major conflict source emerging out of SAM.

Robock et al. (2008) and Pierrehumbert (2019) also mention the risk of a so-called termination shock, which would happen after an abrupt halt of SAM. Since the stratospheric lifetime of sulfate is in the order of one year (Fig. 4.5), the termination of SAM from one day to another would result in a dramatic climate warming within a few years, which would make adaption impossible. Robock et al. (2008) assume, that such

a termination shock could be provoked for example by a technological, societal, or political crisis. Pierrehumbert (2019) further points out that the risk of a termination shock could be a dramatic psychological burden for mankind. Furthermore, the risk that SAM technologies may not stay limited to civil use only once they have been deployed is a major concern presented by Robock et al. (2008).

Finally, the implementation of SAM would potentially also undermine the necessary aggressive mitigation of GHG emissions according to Schneider (2001). Given the fact, that a „business as usual“scenario without significant global warming could be possible when implementing SAM with a sufficient strength, the willingness of mankind to reduce GHG emissions is expected to decrease dramatically. Furthermore, humans may neglect or even ignore the dramatic impacts of increasing atmospheric GHG concentrations in view of SAM – the so-called moral hazard (DFG SPP 1689, 2018) – despite the fact that some of its major consequences like ocean acidification cannot be fixed by SAM.

7 Conclusion and Outlook

Within this study, the stratospheric injection of SO_2 and the stratospheric injection of H_2SO_4, which was modeled as the stratospheric injection of AS-SO_4, have been compared comprehensively with regard to different aspects of SAM. Thereby, aerosol microphysical and radiative properties have been found to depend strongly on the injection species in all tested injection scenarios. Due to an on average smaller sulfate particle size, an injection of H_2SO_4 is radiatively much more efficient than an injection of SO_2 and results in less severe adverse side effects for a given radiative forcing as well. This confirms the results of earlier studies by Pierce et al. (2010), Benduhn et al. (2016), and Vattioni et al. (2019). The aerosol-induced warming of the lower stratosphere and the accompanied modification of the QBO and the BDC are in principle independent of the injection species. These dynamical responses do rather show a strong structural dependence on the injection strategy. Thereby, the meridional structure of the temperature anomalies within the lower tropical stratosphere was found to clearly explain the observed response of the QBO via thermal wind balance. This is a clear advancement compared to earlier studies like Niemeier and Schmidt (2017) or Tilmes et al. (2018), who did not adequately discussed differences in the QBO response between different injection strategies. The strength of the dynamical feedback, which results from the aerosol-induced modification of the QBO and BDC, does again strongly depend on the injection species. This was identified to be a result of the structural different interplay between sedimentation and tropical upwelling.

The results of this study basically coincide with the results of the two other models participating in the GeoMIP6 testbed experiment *accumH2SO4* (Weisenstein and Keith, 2018), which are CESM2(WACCM) (Danabasoglu et al., 2020; Gettelman et al., 2019) and SOCOL-AERv2 (Sheng et al., 2015). Results from these models in principle confirm the aerosol microphysical and radiative advantages of an injection of H_2SO_4 over an injection of SO_2 as well as the observed differences between the region and 2point injection strategies (Weisenstein 2020, personal communication). The stratospheric sulfate burden and the net radiative forcing efficiency roughly agree quantitatively for MAECHAM5-HAM and SOCOL-AERv2. This can be attributed to the fact that SOCOL-AERv2 has the same dynamic core as MAECHAM5-HAM. However, both quantities are significantly larger when simulated with CESM2(WACCM). This can be attributed to the meridional transport of stratospheric tracers, which was found to be significantly stronger in MAECHAM5-HAM than in CESM2(WACCM) (Niemeier 2020, personal communication). Also

compared to satellite measurements after the eruption of the tropical volcano Mt. Pinatubo in June 1991, MAECHAM5-HAM overestimates the poleward meridional transport of sulfate by 10 % – 20 % (Niemeier et al., 2009), which indicates an unrealistically strong transport in MAECHAM5-HAM (see Sec. 3.4). A too strong poleward transport of sulfate reduces its global mean lifetime. The higher horizontal resolution of CESM2(WACCM) ($0.95° \times 1.25°$), which reduces numerical diffusion, may be another reason for its higher global sulfate burden. Furthermore, the residual upwelling within the lower tropical stratosphere is significantly stronger in WACCM than in MAECHAM5-HAM, which further enhances the global mean sulfate lifetime (Niemeier et al., 2020). Therefore, also the strength of the dynamical feedback might be overestimated in the simulations of this study. Since the SST is further prescribed to the same fixed values for all tested injection scenarios, potential differences in the convective wave forcing of the QBO are not adequately taken into account within this study. This adds additional uncertainty to the observed strength of the dynamical feedback.

Vattioni et al. (2019) found that the equilibrium size distribution of the sulfate particles depends significantly on the size of the injected sulfate particles. They showed that an increase of the mode radius of the injected AS-SO_4 population from 0.095 µm to 0.15 µm would result – all else equal – in an increase of the SW radiative forcing by 19.7 % due to more particles being in the optimal size range for backscattering following Dykema et al. (2016). The mode radius of the injected AS-SO_4 particle population in this study was set to 0.075 µm ($\sigma = 1.59$) and is, thereby, clearly smaller than the one used in CESM2(WACCM) and SOCOL-AERv2, which was 0.1 µm ($\sigma = 1.5$). This may be another reason for the observed spread between MAECHAM5-HAM and the other models participating in *accumH2SO4*. It is also clearly smaller than the mode radius suggested by Pierce et al. (2010) and Benduhn et al. (2016), who found that a sulfate particle population with a mode radius between 0.1 µm and 0.15 µm may be produced out of the injected H_2SO_4 after the dispersion of the aircraft plume. Therefore, the resulting sulfate particles for the injections of H_2SO_4 may be potentially too small in this study. The position of the maximum of the sulfate aerosol size distribution directly at the particle size of maximum mass specific backscattering according to Dykema et al. (2016) (i.e. 0.3 µm) may further be rather coincidentally (Fig. 4.3, Fig. 4.8).

Another major shortcoming of this study is the lack of an interactive ozone chemistry within MAECHAM5-HAM. Multiple studies have shown that SAM would cause a substantial depletion of stratospheric ozone via changes of sulfur-related chemical reactions and via modified dynamical processes. For example, Pitari et al. (2014) calculated a global mean reduction of column-integrated ozone of approximately 5 %

for an injection of 4 to 6 $\mathrm{Tg(S)\,yr^{-1}}$ within a multi-model ensemble. They found negative anomalies of up to almost -10 % in the polar regions, but even slightly positive anomalies within the tropics. These SAM-induced changes in stratospheric ozone are accompanied by changes of the radiative heating by the absorption of ISR (Richter et al., 2017). The ozone-induced modification of the stratospheric radiative heating has been found to feedback on stratospheric dynamics (Richter et al., 2017) and the net sulfate aerosol forcing itself (Pitari et al., 2014). Since the ozone concentrations are prescribed offline to MAECHAM5-HAM instead of being calculated interactively, SAM-induced ozone depletion as well as accompanied changes of stratospheric radiative heating are not covered by this study.

MAECHAM5-HAM was further not coupled to an ocean nor a landbiosphere module within this study. The SST and the SIC were prescribed to the same level for all performed simulations, independent of the injection rate. Therefore, the detailed response of the surface climate to an injection of SO_2 and an injection of H_2SO_4 could not be compared within this study. Especially SAM-induced changes in the surface temperature, cloudiness, and precipitation are of great importance for the environment, the agricultural sector, and the society as a whole. SAM-induced changes in the SST and the SIC could have significant adverse impacts on marine ecosystems and fishery. In order to compare an injection of SO_2 and an injection of H_2SO_4 with regard to these important parameters, simulations of injections of both injection species with a fully coupled ESM are clearly desirable for future research. However, this should not obscure the fact that even the most current ESM do not adequately capture important interactions within the climate system (Niemeier and Tilmes, 2017). Therefore, unexpected consequences of SAM would be very likely during its implementation despite detailed model studies. Furthermore, not a single SAM method would be able to reproduce a climate state similar to a natural one with the same global mean temperature. Consequently, a substantial reduction of anthropogenic GHG emissions is still the only responsible way of preventing a drastic global warming.

References

Andrews, D. G., C. B. Leovy, and J. R. Holton, 1987: *Middle Atmosphere Dynamics*. 006th ed., Academic Press, Amsterdam, Boston.

Andrews, D. G., and M. E. McIntyre, 1976: Planetary waves in horizontal and vertical shear: The generalized eliassen-palm relation and the mean zonal acceleration. *Journal of the Atmospheric Sciences*, **33 (11)**, 2031–2048.

Aquila, V., C. I. Garfinkel, P. Newman, L. Oman, and D. Waugh, 2014: Modifications of the quasi-biennial oscillation by a geoengineering perturbation of the stratospheric aerosol layer. *Geophysical Research Letters*, **41 (5)**, 1738–1744, doi: 10.1002/2013GL058818.

Aquila, V., L. D. Oman, R. S. Stolarski, P. R. Colarco, and P. A. Newman, 2012: Dispersion of the volcanic sulfate cloud from a Mount Pinatubo–like eruption. *Journal of Geophysical Research: Atmospheres (1984–2012)*, **117 (D6)**, doi:10.1029/2011JD016968.

Baldwin, M. P., and Coauthors, 2001: The quasi-biennial oscillation. *Reviews of Geophysics*, **39 (2)**, 179–229, doi:10.1029/1999RG000073.

Beer, 1852: Bestimmung der absorption des rothen lichts in farbigen flüssigkeiten. *Annalen der Physik*, **162 (5)**, 78–88, doi:10.1002/andp.18521620505.

Benduhn, F., J. Schallock, and M. G. Lawrence, 2016: Early growth dynamical implications for the steerability of stratospheric solar radiation management via sulfur aerosol particles. *Geophysical Research Letters*, **43 (18)**, 9956–9963, doi: 10.1002/2016GL070701.

Budyko, M. I., 1977: *Climatic Changes*. American Geophysical Union, doi:10.1029/sp010.

Butchart, N., 2014: The brewer-dobson circulation. *Reviews of Geophysics*, **52 (2)**, 157–184, doi:10.1002/2013RG000448.

Crutzen, P. J., 2006: Albedo Enhancement by Stratospheric Sulfur Injections: A Contribution to Resolve a Policy Dilemma? *Climatic Change*, **77 (3)**, 211, doi: {10.1007/s10584-006-9101-y}.

Danabasoglu, G., and Coauthors, 2020: The community earth system model version 2 (cesm2). *Journal of Advances in Modeling Earth Systems*, **12 (2)**, doi:10.1029/2019MS001916.

DFG SPP 1689, 2018: Climate Engineering und unsere Klimaziele - eine überfällige Debatte? ; accessed on 19.11.2019 16:38 h, https://www.spp-climate-engineering.de/index.php/aktuelles.html.

Dykema, J. A., D. W. Keith, and F. N. Keutsch, 2016: Improved aerosol radiative properties as a foundation for solar geoengineering risk assessment. *Geophysical Research Letters*, **43 (14)**, 7758–7766, doi:10.1002/2016GL069258.

English, J. M., O. B. Toon, and M. J. Mills, 2012: Microphysical simulations of sulfur burdens from stratospheric sulfur geoengineering. *Atmospheric Chemistry and Physics*, **12 (10)**, 4775–4793, doi:10.5194/acp-12-4775-2012.

Feinberg, A., T. Sukhodolov, B.-P. Luo, E. Rozanov, L. H. E. Winkel, T. Peter, and A. Stenke, 2019: Improved tropospheric and stratospheric sulfur cycle in the aerosol–chemistry–climate model socol-aerv2. *Geoscientific Model Development*, **12 (9)**, 3863–3887, doi:10.5194/gmd-12-3863-2019.

Ferraro, A. J., E. J. Highwood, and A. J. Charlton-Perez, 2011: Stratospheric heating by potential geoengineering aerosols. *Geophysical Research Letters*, **38 (24)**, doi:10.1029/2011GL049761.

Garfinkel, C. I., and D. L. Hartmann, 2011: The influence of the quasi-biennial oscillation on the troposphere in winter in a hierarchy of models. part i: Simplified dry gcms. *Journal of the Atmospheric Sciences*, **68 (6)**, 1273–1289, doi:10.1175/2011JAS3665.1.

Garfinkel, C. I., D. W. Waugh, L. D. Oman, L. Wang, and M. M. Hurwitz, 2013: Temperature trends in the tropical upper troposphere and lower stratosphere: Connections with sea surface temperatures and implications for water vapor and ozone. *Journal of Geophysical Research: Atmospheres*, **118 (17)**, 9658–9672, doi:10.1002/jgrd.50772.

Gettelman, A., and Coauthors, 2019: The whole atmosphere community climate model version 6 (waccm6). *Journal of Geophysical Research: Atmospheres*, **124 (23)**, 12 380–12 403, doi:10.1029/2019JD030943.

Giorgetta, M. A., E. Manzini, E. Roeckner, M. Esch, and L. Bengtsson, 2006: Climatology and forcing of the quasi-biennial oscillation in the maecham5 model. *Journal of Climate*, **19 (16)**, 3882–3901, doi:10.1175/JCLI3830.1.

Hartmann, D. L., 2016: *Global Physical Climatology*. 2nd ed., Elsevier Science, Stanford.

Haszeldine, R. S., S. Flude, G. Johnson, and V. Scott, 2018: Negative emissions technologies and carbon capture and storage to achieve the paris agreement commitments. *Philosophical Transactions of the Royal Society A: Mathematical, Physical and Engineering Sciences*, **376 (2119)**, 20160 447, doi:10.1098/rsta.2016.0447.

Haynes, P., and E. Shuckburgh, 2000: Effective diffusivity as a diagnostic of atmospheric transport: 1. stratosphere. *Journal of Geophysical Research: Atmospheres*, **105 (D18)**, 22 777–22 794, doi:10.1029/2000JD900093.

Heckendorn, P., D. Weisenstein, S. Fueglistaler, B. P. Luo, E. Rozanov, M. Schraner, L. W. Thomason, and T. Peter, 2009: The impact of geoengineering aerosols on stratospheric temperature and ozone. *Environmental Research Letters*, **4 (4)**, 045 108.

Holloway, C. E., and J. D. Neelin, 2007: The convective cold top and quasi equilibrium. *Journal of the Atmospheric Sciences*, **64 (5)**, 1467–1487, doi:10.1175/JAS3907.1.

Holton, J. R., 2004: *An Introduction to Dynamic Meteorology*. 4th ed., Academic Press, Amsterdam, Boston.

Holton, J. R., and R. S. Lindzen, 1972: An updated theory for the quasi-biennial cycle of the tropical stratosphere. *Journal of the Atmospheric Sciences*, **29 (6)**, 1076–1080, doi:10.1175/1520-0469(1972)029<1076:AUTFTQ>2.0.CO;2.

Holton, J. R., and H.-C. Tan, 1980: The influence of the equatorial quasi-biennial oscillation on the global circulation at 50 mb. *Journal of the Atmospheric Sciences*, **37 (10)**, 2200–2208, doi:10.1175/1520-0469(1980)037<2200:TIOTEQ>2.0.CO;2.

Hommel, R., and H.-F. Graf, 2011: Modelling the size distribution of geoengineered stratospheric aerosols. *Atmospheric Science Letters*, **12 (2)**, 168–175, doi:10.1002/asl.285.

IPCC, 2014: Climate Change 2014: Synthesis Report. Contribution of WOrking Groups I, II and III to the Fifth Assessment Report of the Intergovernmental Panel on Climate Change.

Jones, A., J. Haywood, O. Boucher, B. Kravitz, and A. Robock, 2010: Geoengineering by stratospheric so_2 injection: results from the met office hadgem2 climate model

and comparison with the goddard institute for space studies modele. *Atmospheric Chemistry and Physics*, **10 (13)**, 5999–6006, doi:10.5194/acp-10-5999-2010.

Kokkola, H., R. Hommel, J. Kazil, U. Niemeyer, A.-I. Partanen, J. Feichter, and C. Timmreck, 2009: Aerosol microphysics modules in the framework of the echam5 climate model – intercomparison under stratospheric conditions. *Geoscientific Model Development*, **2**, 97–112.

Kravitz, B., D. G. MacMartin, M. J. Mills, J. H. Richter, S. Tilmes, J.-F. Lamarque, J. J. Tribbia, and F. Vitt, 2017: First simulations of designing stratospheric sulfate aerosol geoengineering to meet multiple simultaneous climate objectives. *Journal of Geophysical Research: Atmospheres*, **122 (23)**, 12,616–12,634, doi:10.1002/2017JD026874.

Kravitz, B., and Coauthors, 2015: The geoengineering model intercomparison project phase 6 (geomip6): Simulation design and preliminary results. *Geoscientific Model Development*, **8**, 3379 – 3392, doi:10.5194/gmd-8-3379-2015.

Kravitz, B., and Coauthors, 2019: Comparing surface and stratospheric impacts of geoengineering with different so2 injection strategies. *Journal of Geophysical Research: Atmospheres*, **124 (14)**, 7900–7918, doi:10.1029/2019JD030329.

Laakso, A., H. Kokkola, A.-I. Partanen, U. Niemeier, C. Timmreck, K. E. J. Lehtinen, H. Hakkarainen, and H. Korhonen, 2016: Radiative and climate impacts of a large volcanic eruption during stratospheric sulfur geoengineering. *Atmospheric Chemistry and Physics*, **16 (1)**, 305–323, doi:10.5194/acp-16-305-2016.

Lin, S.-J., and R. B. Rood, 1996: Multidimensional flux-form semi-lagrangian transport schemes. *Monthly Weather Review*, **124 (9)**, 2046–2070, doi:10.1175/1520-0493(1996)124<2046:MFFSLT>2.0.CO;2.

Lindzen, R. S., and J. R. Holton, 1968: A theory of the quasi-biennial oscillation. *Journal of the Atmospheric Sciences*, **25 (6)**, 1095–1107, doi:10.1175/1520-0469(1968)025<1095:ATOTQB>2.0.CO;2.

McIntyre, M., and T. Palmer, 1984: The 'surf zone' in the stratosphere. *Journal of Atmospheric and Terrestrial Physics*, **46 (9)**, 825 – 849, doi:https://doi.org/10.1016/0021-9169(84)90063-1.

McIntyre, M. E., P. Wadhams, J. A. Dowdeswell, and A. N. Schofield, 1995: The stratospheric polar vortex and sub-vortex : fluid dynamics and midlatitude ozone loss. *Philosophical Transactions of the Royal Society of London. Series A: Physical and Engineering Sciences*, **352 (1699)**, 227–240, doi:10.1098/rsta.1995.0066.

National Geophysical Data Center, 1992: U.S. standard atmosphere (1976). *Planetary and Space Science*, **40**, 553–554, doi:10.1016/0032-0633(92)90203-Z.

Niemeier, U., J. H. Richter, and S. Tilmes, 2020: Differing responses of the qbo to so_2 injections in two global models. *Atmospheric Chemistry and Physics Discussions*, **2020**, 1–21, doi:10.5194/acp-2020-206.

Niemeier, U., and H. Schmidt, 2017: Changing transport processes in the stratosphere by radiative heating of sulfate aerosols. *Atmospheric Chemistry and Physics*, **17 (24)**, 14 871–14 886, doi:10.5194/acp-17-14871-2017.

Niemeier, U., H. Schmidt, K. Alterskjær, and J. E. Kristjánsson, 2013: Solar irradiance reduction via climate engineering: Impact of different techniques on the energy balance and the hydrological cycle. *Journal of Geophysical Research: Atmospheres*, **118 (21)**, 11,905–11,917, doi:10.1002/2013JD020445.

Niemeier, U., H. Schmidt, and C. Timmreck, 2011: The dependency of geoengineered sulfate aerosol on the emission strategy. *Atmospheric Science Letters*, **12 (2)**, 189–194, doi:10.1002/asl.304.

Niemeier, U., and S. Tilmes, 2017: Sulfur injections for a cooler planet. *Science*, **357 (6348)**, 246–248, doi:10.1126/science.aan3317.

Niemeier, U., and C. Timmreck, 2015: What is the limit of climate engineering by stratospheric injection of so_2? *Atmospheric Chemistry and Physics*, **15 (16)**, 9129–9141, doi:10.5194/acp-15-9129-2015.

Niemeier, U., C. Timmreck, H.-F. Graf, S. Kinne, S. Rast, and S. Self, 2009: Initial fate of fine ash and sulfur from large volcanic eruptions. *Atmospheric Chemistry and Physics*, **9 (22)**, 9043–9057, doi:10.5194/acp-9-9043-2009.

O'Neill, B. C., and Coauthors, 2016: The scenario model intercomparison project (ScenarioMIP) for CMIP6. *Geoscientific Model Development*, **9 (9)**, 3461–3482, doi:10.5194/gmd-9-3461-2016.

Pierce, J. R., D. K. Weisenstein, P. Heckendorn, T. Peter, and D. W. Keith, 2010: Efficient formation of stratospheric aerosol for climate engineering by emission of condensible vapor from aircraft. *Geophysical Research Letters*, **37 (18)**, doi:10.1029/2010GL043975.

Pierrehumbert, R., 2019: There is no plan b for dealing with the climate crisis. *Bulletin of the Atomic Scientists*, **75 (5)**, 215–221, doi:10.1080/00963402.2019.1654255.

Pitari, G., and Coauthors, 2014: Stratospheric ozone response to sulfate geoengineering: Results from the geoengineering model intercomparison project (geomip). *Journal of Geophysical Research: Atmospheres*, **119 (5)**, 2629–2653, doi: 10.1002/2013JD020566.

Plumb, R. A., 1996: A "tropical pipe" model of stratospheric transport. *Journal of Geophysical Research: Atmospheres*, **101 (D2)**, 3957–3972, doi:10.1029/95JD03002.

Plumb, R. A., and R. C. Bell, 1982: A model of the quasi-biennial oscillation on an equatorial beta-plane. *Quarterly Journal of the Royal Meteorological Society*, **108 (456)**, 335–352, doi:10.1002/qj.49710845604.

Punge, H. J., P. Konopka, M. A. Giorgetta, and R. Müller, 2009: Effects of the quasi-biennial oscillation on low-latitude transport in the stratosphere derived from trajectory calculations. *Journal of Geophysical Research: Atmospheres*, **114 (D3)**, doi:10.1029/2008JD010518.

Richter, J. H., S. Tilmes, M. J. Mills, J. J. Tribbia, B. Kravitz, D. G. MacMartin, F. Vitt, and J.-F. Lamarque, 2017: Stratospheric dynamical response and ozone feedbacks in the presence of so2 injections. *Journal of Geophysical Research: Atmospheres*, **122 (23)**, 12,557–12,573, doi:10.1002/2017JD026912.

Robock, A., K. Jerch, and M. Bunzl, 2008: 20 reasons why geoengineering may be a bad idea. *Bulletin of the Atomic Scientists*, **64**, 14–59, doi:10.1080/00963402.2008.11461140.

Roeckner, E., and Coauthors, 2003: The atmospheric general circulation model echam5. part i. model description. Tech. rep., MPI for Meteorology.

Roeckner, E., and Coauthors, 2006: Sensitivity of simulated climate to horizontal and vertical resolution in the echam5 atmosphere model. *Journal of Climate*, **19 (16)**, 3771–3791, doi:10.1175/JCLI3824.1.

Saxler, B., J. Siegfried, and A. Proelss, 2015: International liability for transboundary damage arising from stratospheric aerosol injections. *Law, Innovation and Technology*, **7 (1)**, 112–147, doi:10.1080/17579961.2015.1052645.

Schmidt, H., and Coauthors, 2012: Solar irradiance reduction to counteract radiative forcing from a quadrupling of co_2: climate responses simulated by four earth system models. *Earth System Dynamics*, **3 (1)**, 63–78, doi:10.5194/esd-3-63-2012.

Schneider, S. H., 2001: Earth systems engineering and management. *Nature*, **409 (6818)**, 417–420, doi:10.1038/35053203.

Seinfeld, J., and S. Pandis, 1998: *Atmospheric chemistry and physics: from air pollution to climate change*. A Wiley interscience publication, Wiley.

Seo, J., W. Choi, D. Youn, D.-S. R. Park, and J. Y. Kim, 2013: Relationship between the stratospheric quasi-biennial oscillation and the spring rainfall in the western north pacific. *Geophysical Research Letters*, **40 (22)**, 5949–5953, doi:10.1002/2013GL058266.

Sheng, J.-X., D. K. Weisenstein, B.-P. Luo, E. Rozanov, A. Stenke, J. Anet, H. Bingemer, and T. Peter, 2015: Global atmospheric sulfur budget under volcanically quiescent conditions: Aerosol-chemistry-climate model predictions and validation. *Journal of Geophysical Research: Atmospheres*, **120 (1)**, 256–276, doi:10.1002/2014JD021985.

Shepherd, T. G., 2000: The middle atmosphere. *Journal of Atmospheric and Solar-Terrestrial Physics*, **62 (17)**, 1587 – 1601, doi:https://doi.org/10.1016/S1364-6826(00)00114-0.

Shuckburgh, E., W. Norton, A. Iwi, and P. Haynes, 2001: Influence of the quasi-biennial oscillation on isentropic transport and mixing in the tropics and subtropics. *Journal of Geophysical Research: Atmospheres*, **106 (D13)**, 14 327–14 337, doi:10.1029/2000JD900664.

Smith, J. P., J. A. Dykema, and D. W. Keith, 2018: Production of sulfates onboard an aircraft: Implications for the cost and feasibility of stratospheric solar geoengineering. *Earth and Space Science*, **5 (4)**, 150–162, doi:10.1002/2018EA000370.

Stier, P., and Coauthors, 2005: The aerosol-climate model echam5-ham. *Atmospheric Chemistry and Physics*, **5 (4)**, 1125–1156, doi:10.5194/acp-5-1125-2005.

Tilmes, S., J. H. Richter, M. J. Mills, B. Kravitz, D. G. MacMartin, F. Vitt, J. J. Tribbia, and J.-F. Lamarque, 2017: Sensitivity of aerosol distribution and climate response to stratospheric so2 injection locations. *Journal of Geophysical Research: Atmospheres*, **122 (23)**, 12,591–12,615, doi:10.1002/2017JD026888.

Tilmes, S., B. M. Sanderson, and B. C. O'Neill, 2016: Climate impacts of geoengineering in a delayed mitigation scenario. *Geophysical Research Letters*, **43 (15)**, 8222–8229, doi:10.1002/2016GL070122.

Tilmes, S., and Coauthors, 2018: Effects of different stratospheric so2 injection altitudes on stratospheric chemistry and dynamics. *Journal of Geophysical Research: Atmospheres*, **123 (9)**, 4654–4673, doi:10.1002/2017JD028146.

Timmreck, C., 2001: Three-dimensional simulation of stratospheric background aerosol: First results of a multiannual general circulation model simulation. *Journal of Geophysical Research: Atmospheres*, **106 (D22)**, 28 313–28 332, doi:10.1029/2001JD000765.

Toohey, M., K. Krüger, U. Niemeier, and C. Timmreck, 2011: The influence of eruption season on the global aerosol evolution and radiative impact of tropical volcanic eruptions. *Atmospheric Chemistry and Physics*, **11 (23)**, 12 351–12 367, doi:10.5194/acp-11-12351-2011.

Trepte, C. R., and M. H. Hitchman, 1992: Tropical stratospheric circulation deduced from satellite aerosol data. *Nature*, **355 (6361)**, 626–628, doi:10.1038/355626a0.

United Nations Environment Programme, 2019: *Emissions Gap Report 2018*. 107 pp., doi:https://doi.org/10.18356/08bd6547-en.

Vattioni, S., D. Weisenstein, D. Keith, A. Feinberg, T. Peter, and A. Stenke, 2019: Exploring accumulation-mode H_2SO_4 versus SO_2 stratospheric sulfate geoengineering in a sectional aerosol–chemistry–climate model. *Atmospheric Chemistry and Physics*, **19 (7)**, 4877–4897, doi:10.5194/acp-19-4877-2019.

Vignati, E., J. Wilson, and P. Stier, 2004: M7: An efficient size-resolved aerosol microphysics module for large-scale aerosol transport models. *Journal of Geophysical Research: Atmospheres (1984–2012)*, **109 (D22)**, doi:10.1029/2003JD004485.

Visioni, D., G. Pitari, and V. Aquila, 2017: Sulfate geoengineering: a review of the factors controlling the needed injection of sulfur dioxide. *Atmospheric Chemistry and Physics*, **17 (6)**, 3879–3889, doi:10.5194/acp-17-3879-2017.

Weisenstein, D., and D. Keith, 2018: Draft proposal to model emission of accumulation mode h2so4 in chemistry-climate models for a geomip test-bed intercomparison study. ; accessed on 28.11.2019 11:09 h, http://climate.envsci.rutgers.edu/GeoMIP/testbed.html.

Weisenstein, D. K., J. E. Penner, M. Herzog, and X. Liu, 2007: Global 2-d intercomparison of sectional and modal aerosol modules. *Atmospheric Chemistry and Physics*, **7 (9)**, 2339–2355, doi:10.5194/acp-7-2339-2007.

Acknowledgements

First of all, I want to deeply thank my supervisors Dr. Ulrike Niemeier and Prof. Dr. Stefan Bühler for their great support and guidance during all steps of my Master's thesis. Their assistance as well as their technical and scientific input were of essential importance for successfully finishing my thesis. I especially want to thank Dr. Ulrike Niemeier for enabling me to work on this exciting project while at the same time allowing me to focus my work on my special interests. I also greatly appreciated her commitment in enabling me many contacts and opportunities within the SAM community.

I further want to thank Dr. Claudia Timmreck and Clarissa Kroll of the AES-SFC group at the MPI-M for many valuable discussions and their great advice during the preparation of my thesis. Their input and help greatly improved my thesis. I really appreciated being part of the SFC group during the last 14 months.

Furthermore, I want to express my thanks to Dr. Luis Kornblüh and Oliver Lemke, who helped me with technical problems regarding MAECHAM5-HAM and Python, as well as to Dr. Hauke Schmidt for discussing parts of my results with me.

Moreover, I would like to acknowledge all members of the GeoMIP6 accumH2SO4 group for providing the results of their models as well as for many helpful remarks.

Finally, I would like to thank my fellow students and friends Katharina Baier, Finn Burgemeister, Kai-Uwe Eiselt, Lara Hellmich, Daniel Krieger, Tobias Machnitzki, Julia Menken, Jule Radtke, Daniel Sorg, and Moritz Witt for many valuable comments and discussions, great lunch breaks, and many good times.

Appendices

A1: Heating rates

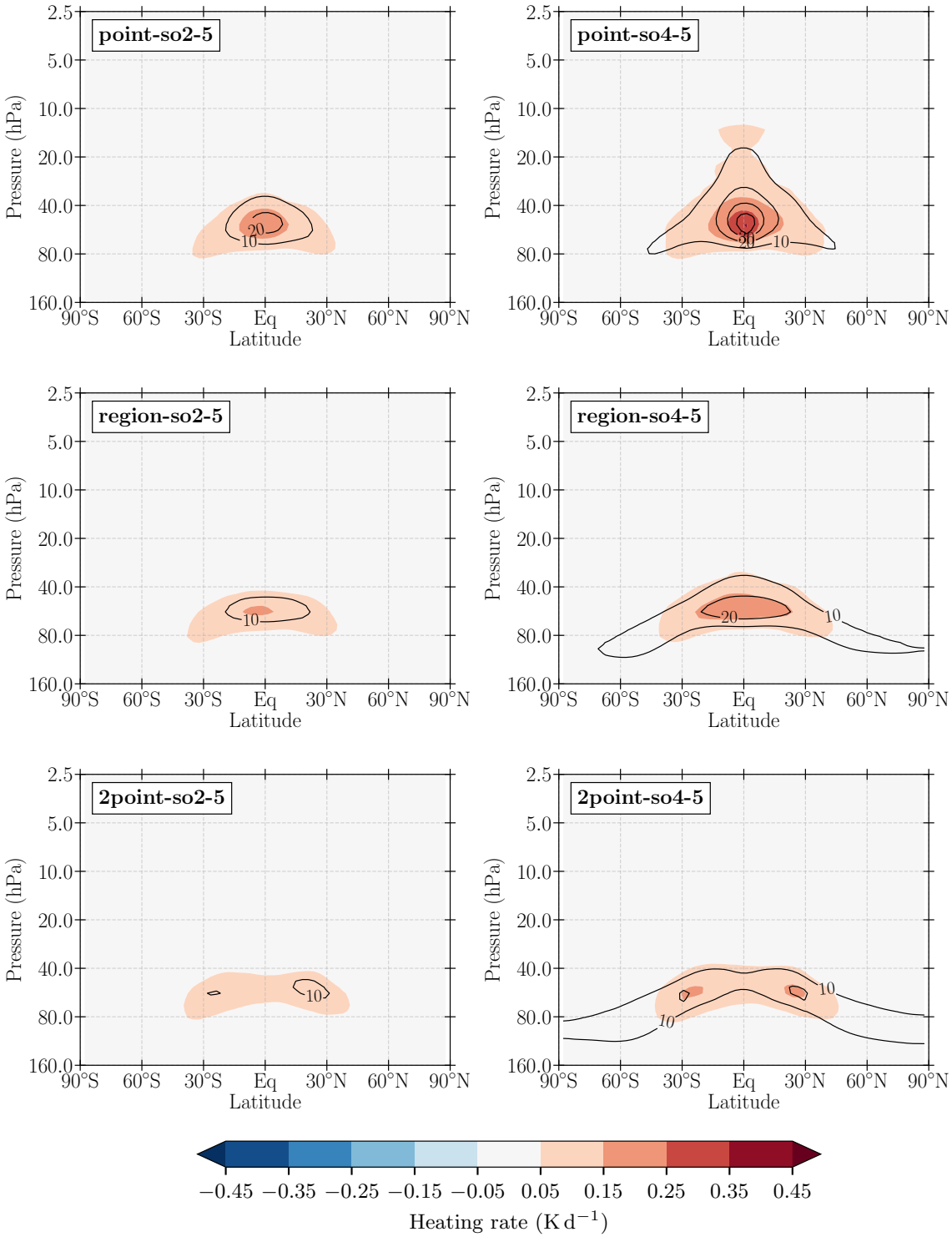

Figure A.1: Like Figure 5.1, but for injections with an injection rate of 5 Tg(S) yr^{-1}.

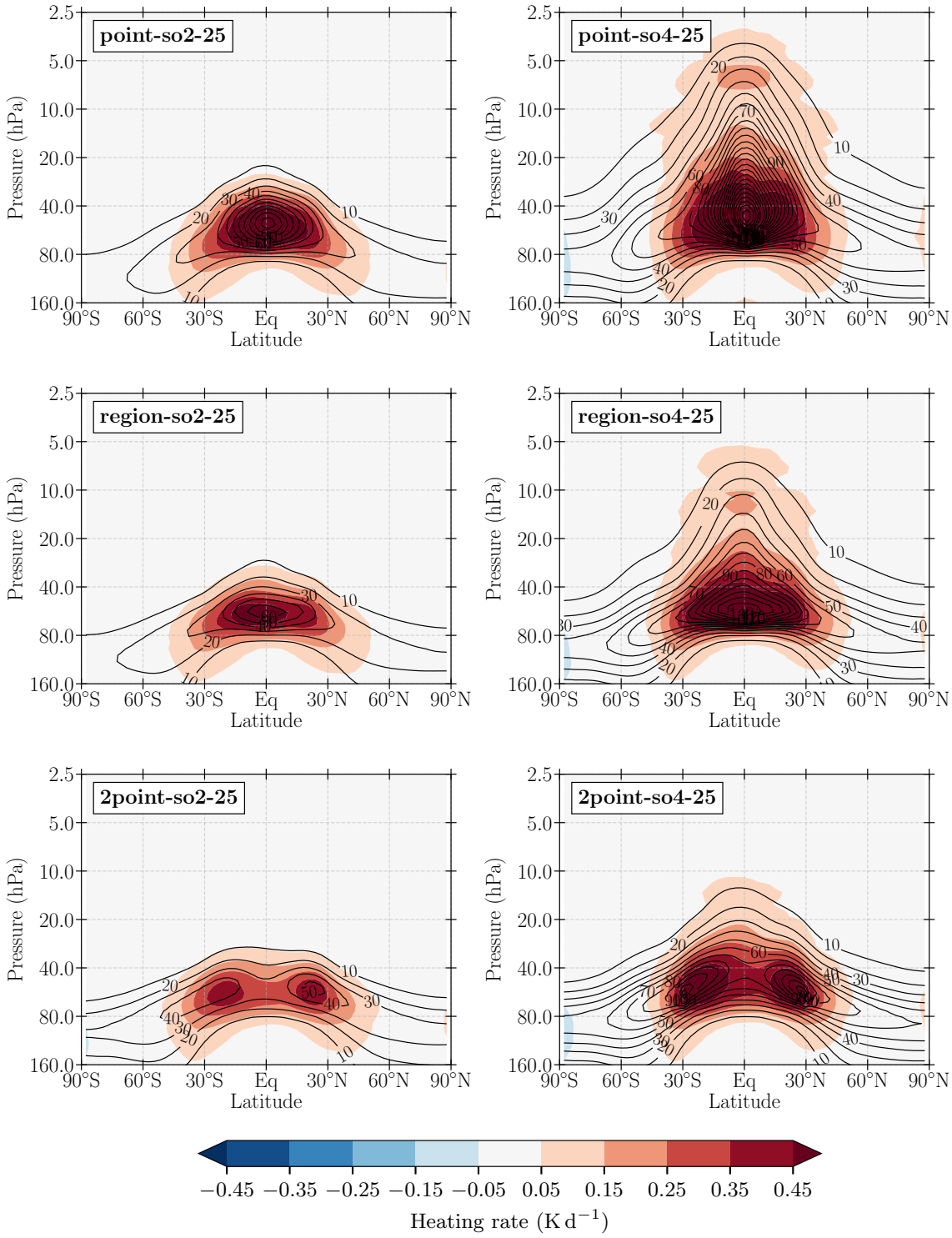

Figure A.2: Like Figure 5.1, but for injections with an injection rate of 25 Tg(S) yr^{-1}.

A2: Temperature anomalies

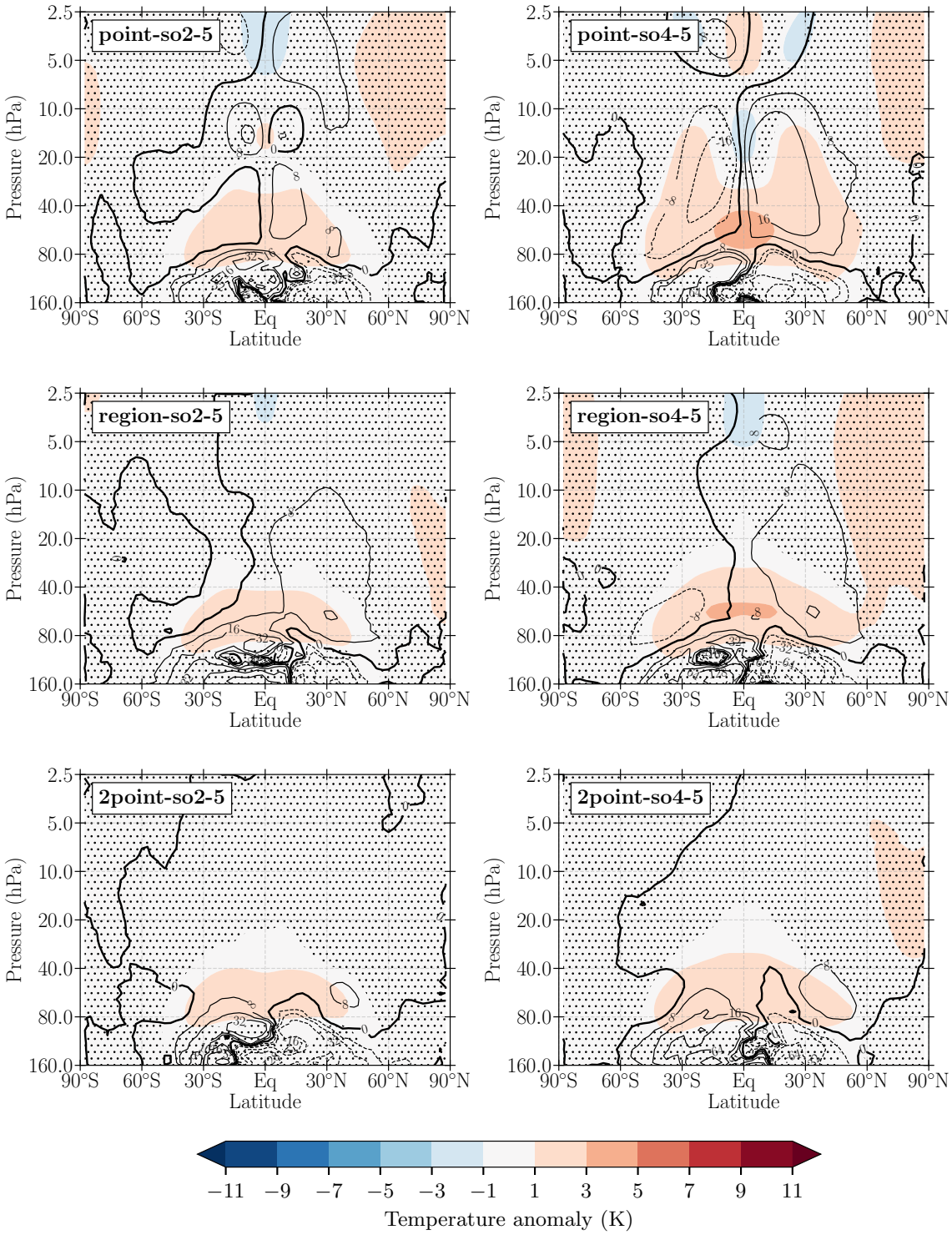

Figure A.3: Like Figure 5.2, but for injections with an injection rate of $5\,\mathrm{Tg(S)\,yr^{-1}}$.

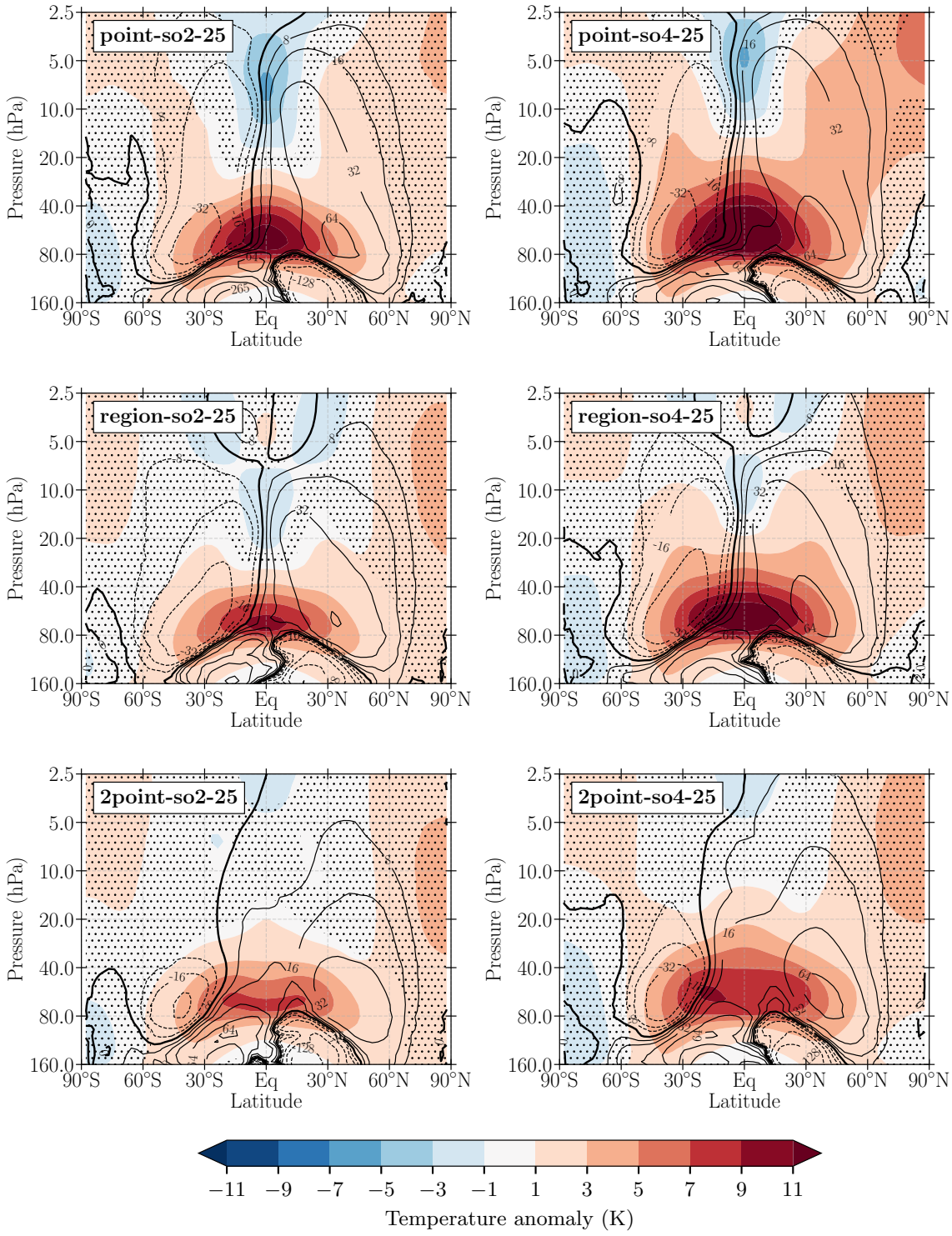

Figure A.4: Like Figure 5.2, but for injections with an injection rate of 25 Tg(S) yr^{-1}.

A3: QBO

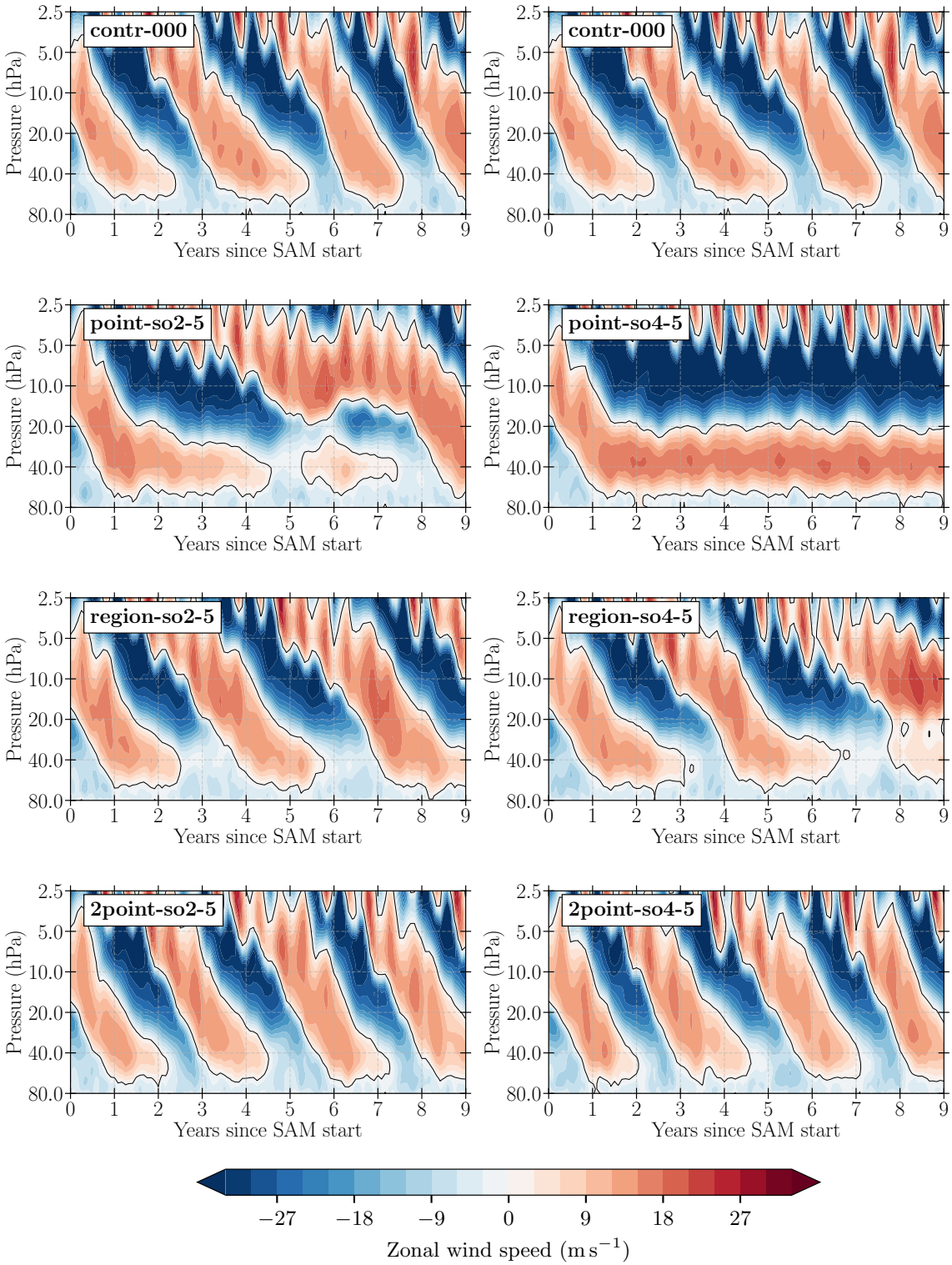

Figure A.5: Like Figure 5.3, but for injections with an injection rate of 5 Tg(S) yr^{-1}.

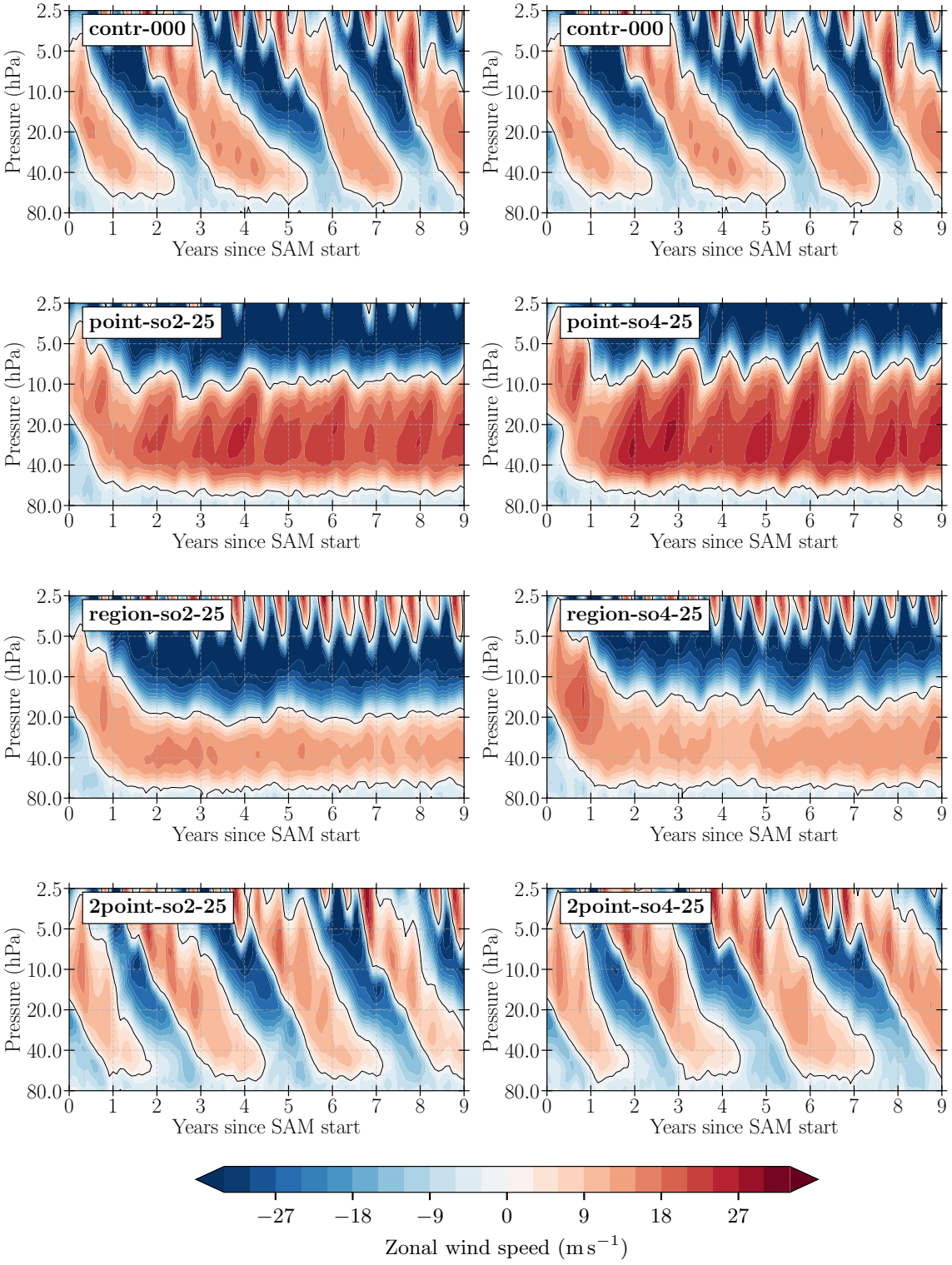

Figure A.6: Like Figure 5.3, but for injections with an injection rate of 25 Tg(S) yr^{-1}.

A4: Temperature gradient and curvature

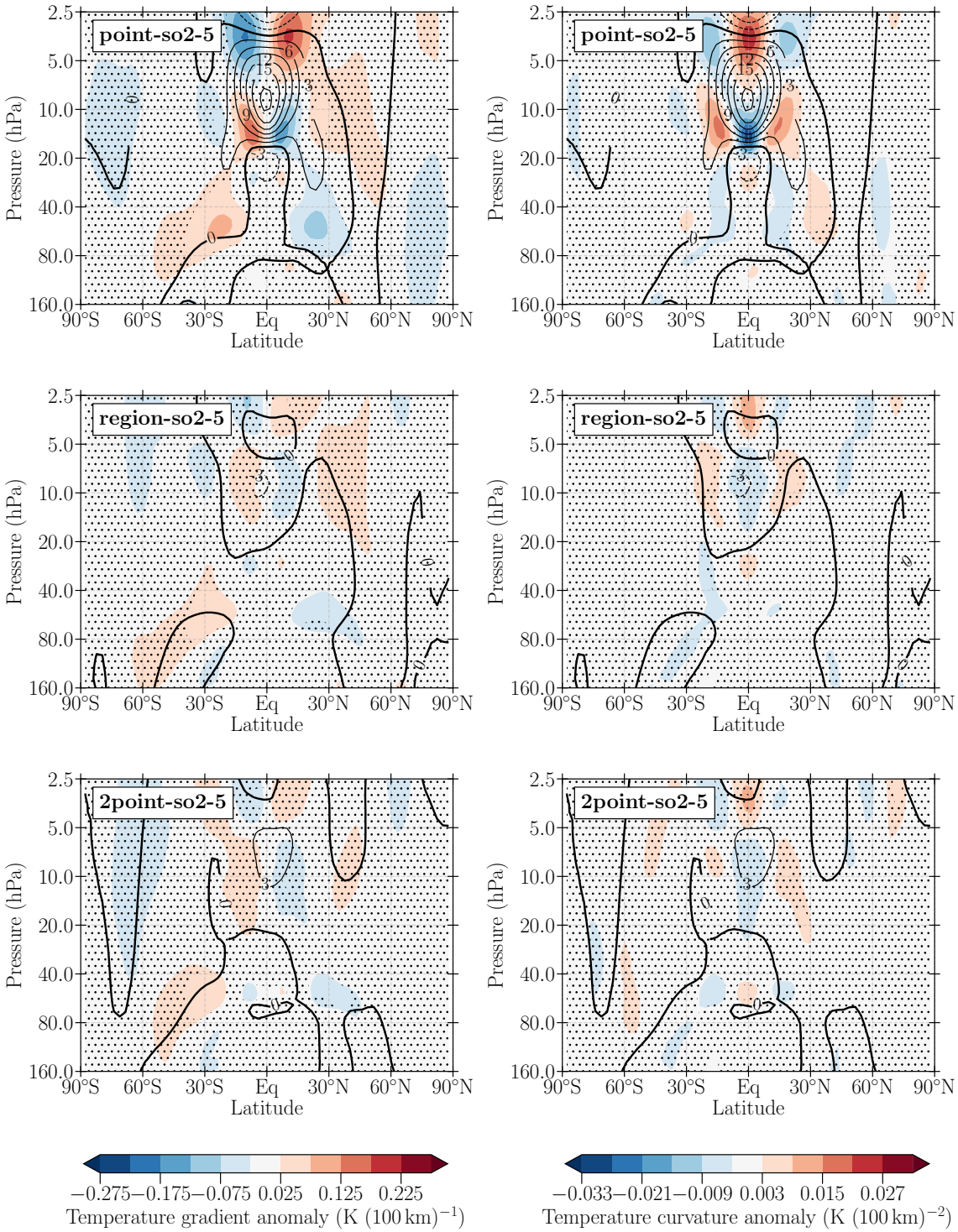

(a) $\Delta\overline{T}_{\mathrm{y}}$ **(b)** $\Delta\overline{T}_{\mathrm{yy}}$

Figure A.7: Like Figure 5.4, but for injections of SO_2 with an injection rate of 5 Tg(S) yr^{-1}.

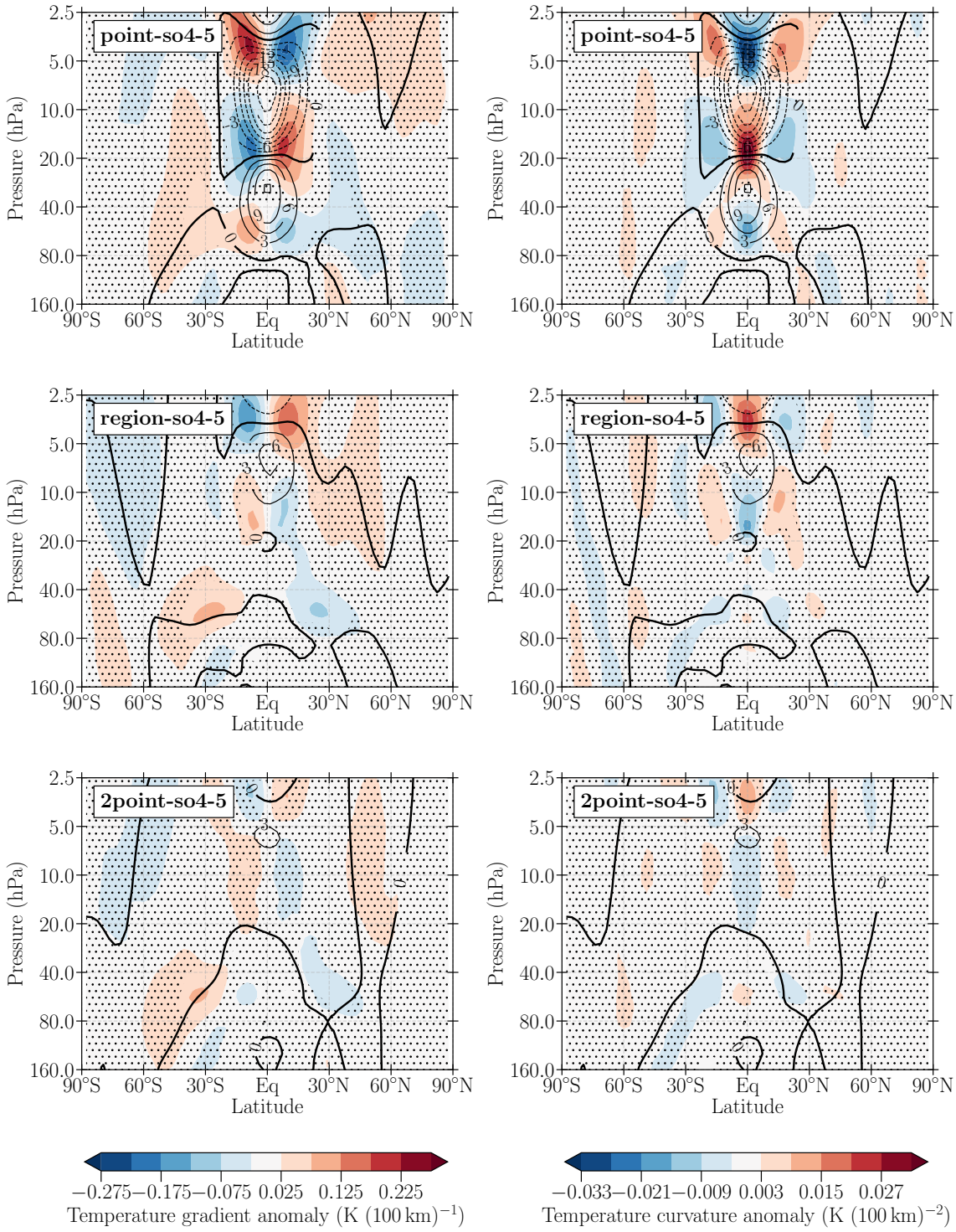

(a) $\Delta\overline{T}_{\mathrm{y}}$ **(b)** $\Delta\overline{T}_{\mathrm{yy}}$

Figure A.8: Like Figure 5.4, but for injections of H_2SO_4 with an injection rate of $5\,\mathrm{Tg(S)\,yr^{-1}}$.

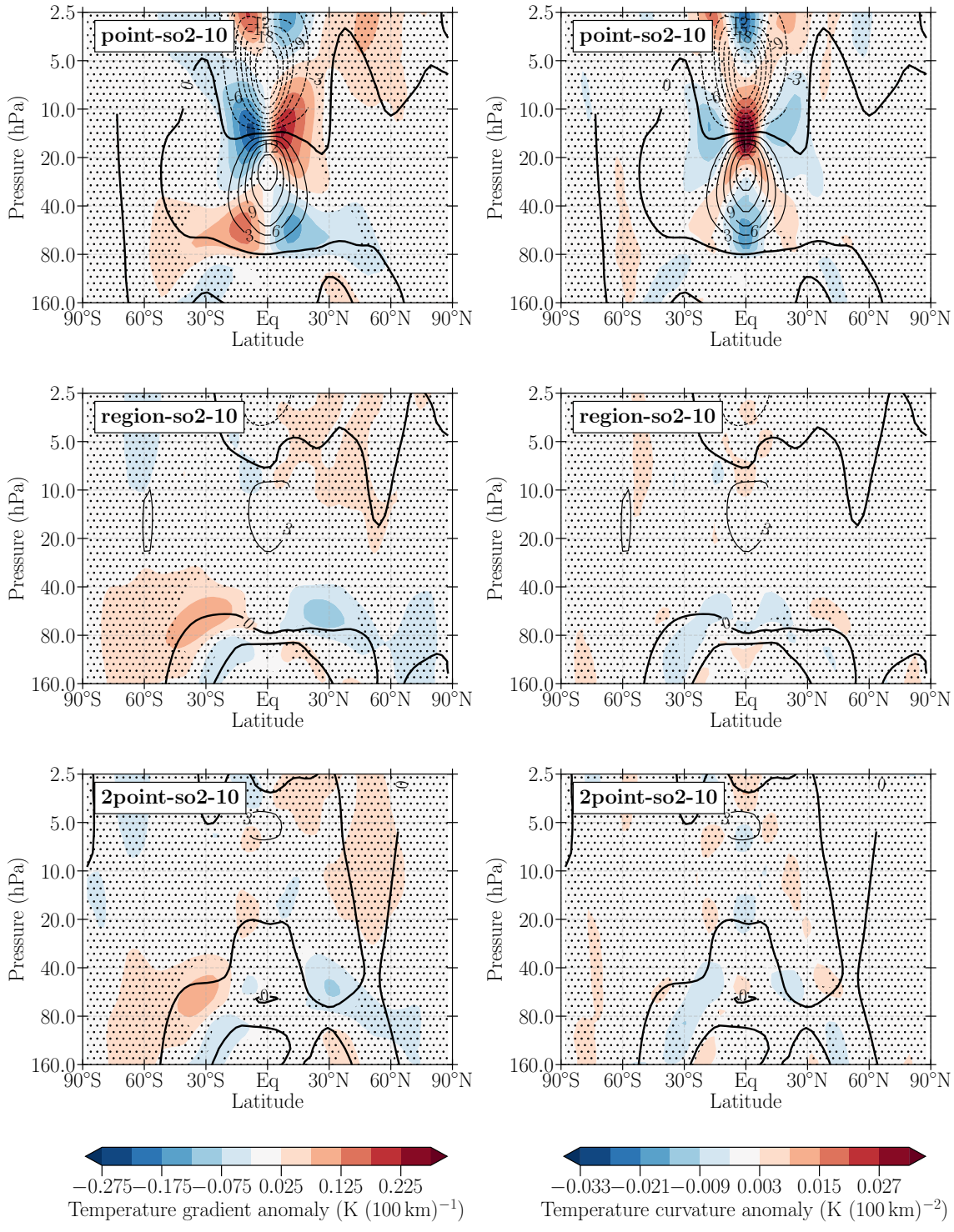

(a) $\Delta\overline{T}_{\mathrm{y}}$ **(b)** $\Delta\overline{T}_{\mathrm{yy}}$

Figure A.9: Like Figure 5.4, but for injections of SO_2 with an injection rate of $10\,\mathrm{Tg(S)\,yr^{-1}}$.

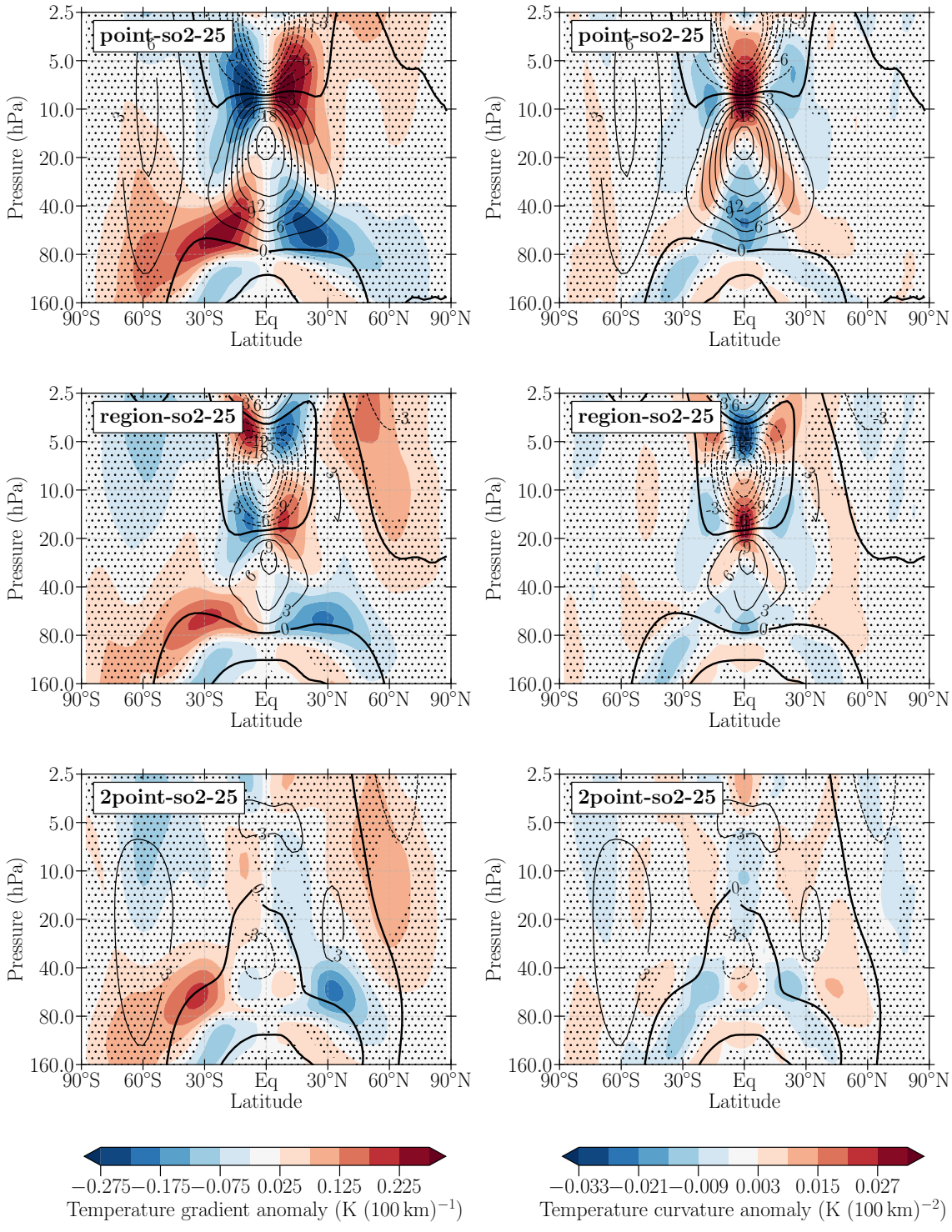

(a) $\Delta\overline{T}_{\mathrm{y}}$ **(b)** $\Delta\overline{T}_{\mathrm{yy}}$

Figure A.10: Like Figure 5.4, but for injections of SO_2 with an injection rate of 25 Tg(S) yr^{-1}.

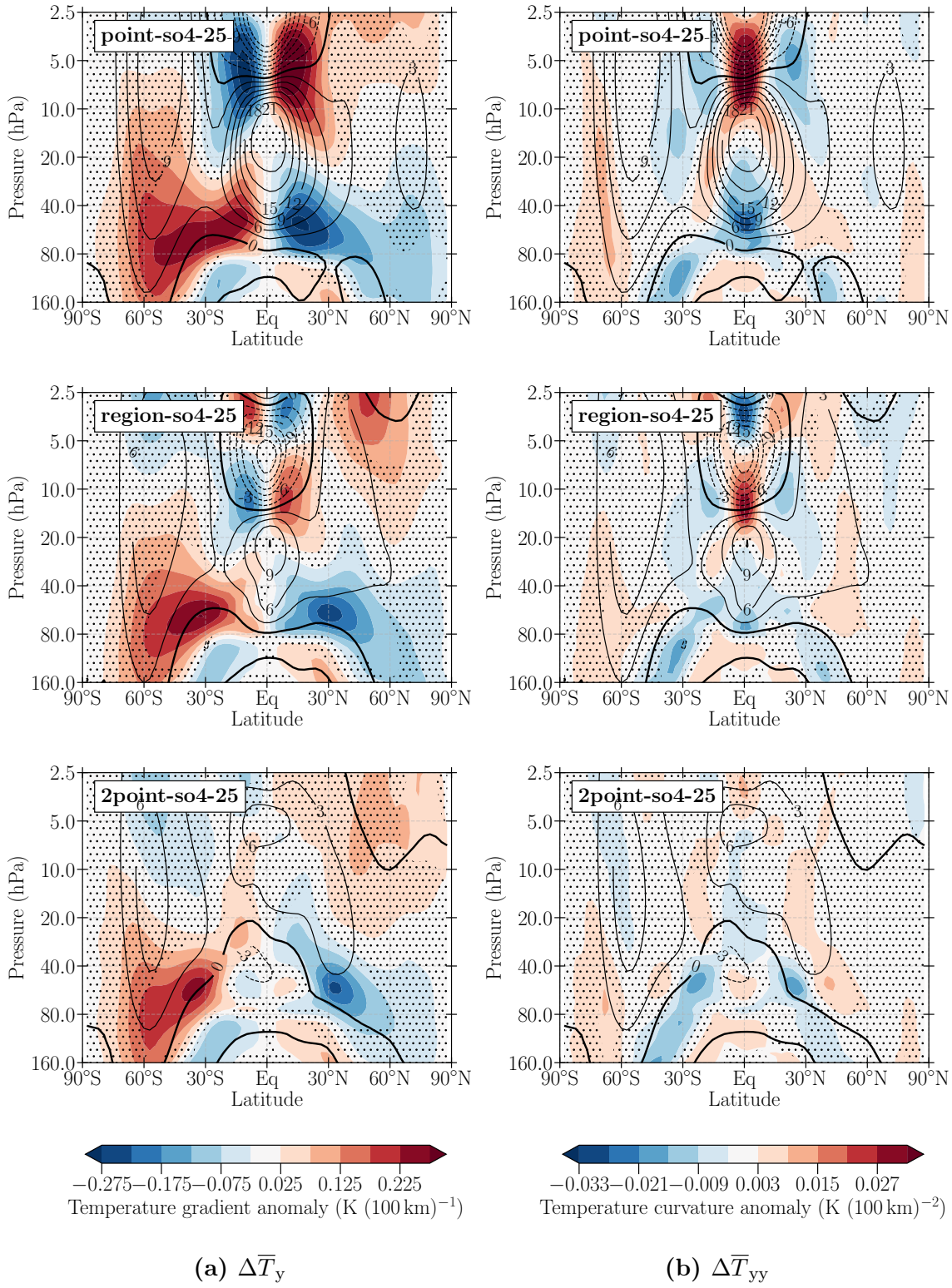

(a) $\Delta\overline{T}_{\mathrm{y}}$ **(b)** $\Delta\overline{T}_{\mathrm{yy}}$

Figure A.11: Like Figure 5.4, but for injections of H_2SO_4 with an injection rate of 25 Tg(S) yr^{-1}.

A5: Residual vertical velocity

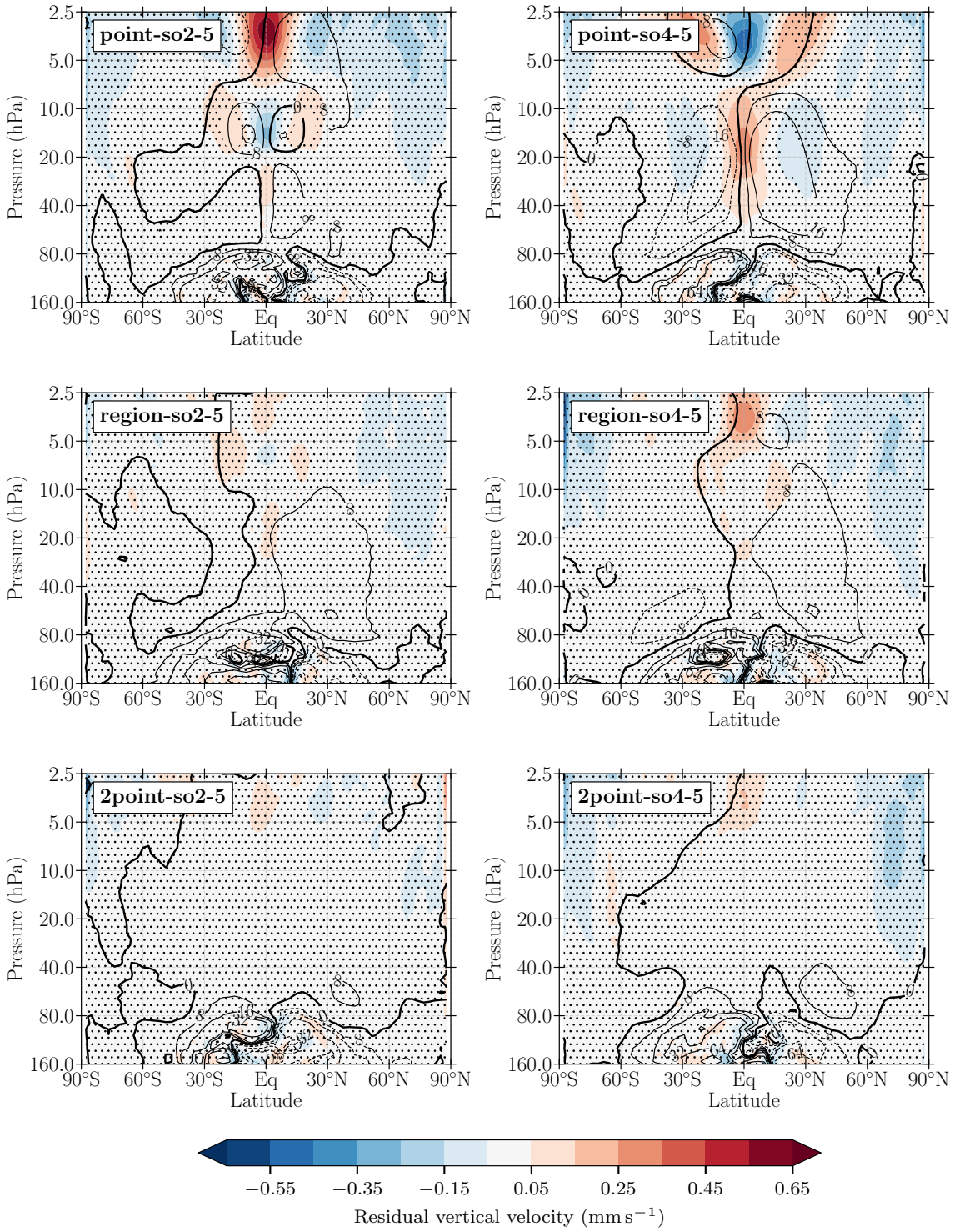

Figure A.12: Like Figure 5.7, but for injections with an injection rate of 5 Tg(S) yr^{-1}.

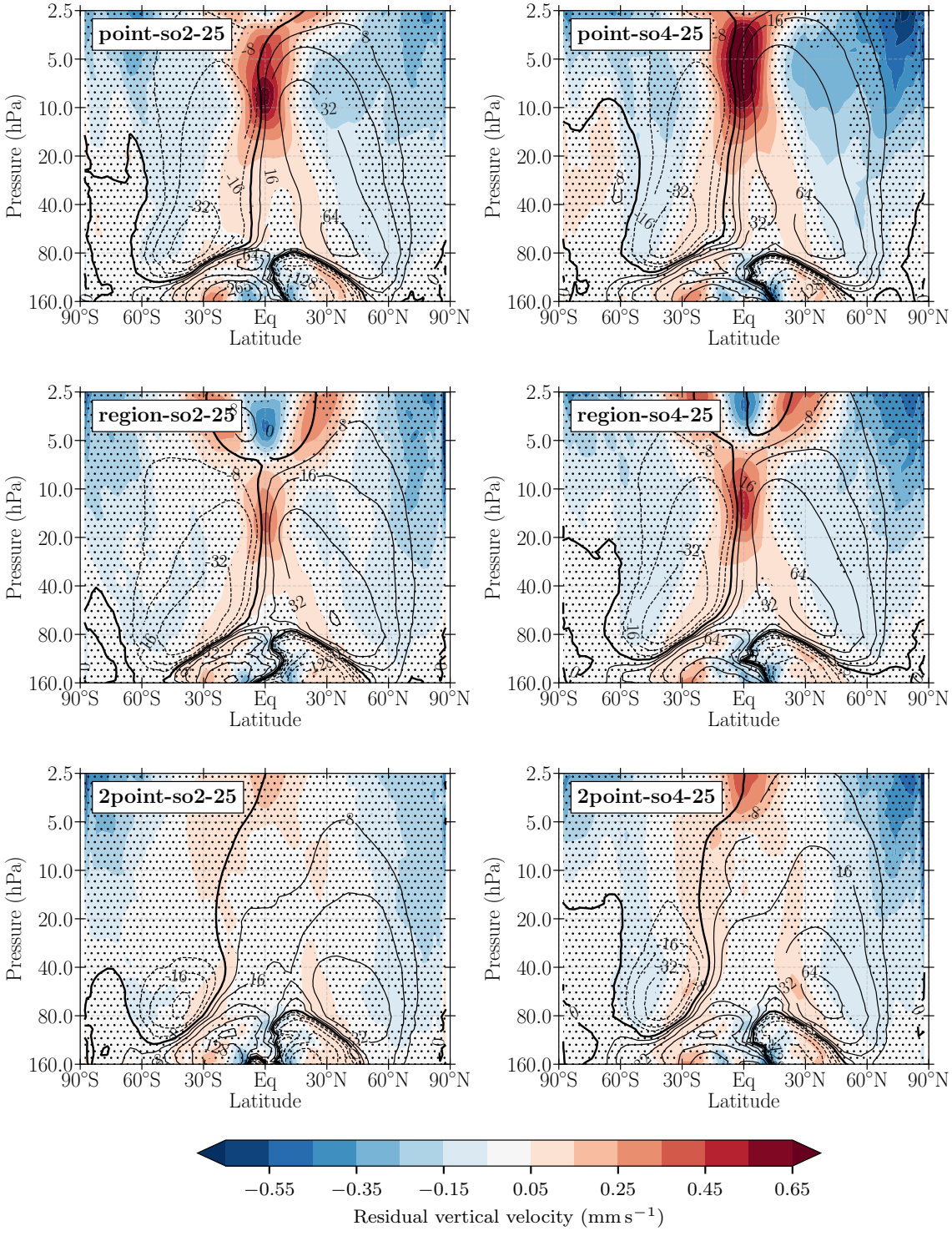

Figure A.13: Like Figure 5.7, but for injections with an injection rate of 25 Tg(S) yr^{-1}.

A6: Net vertical velocity

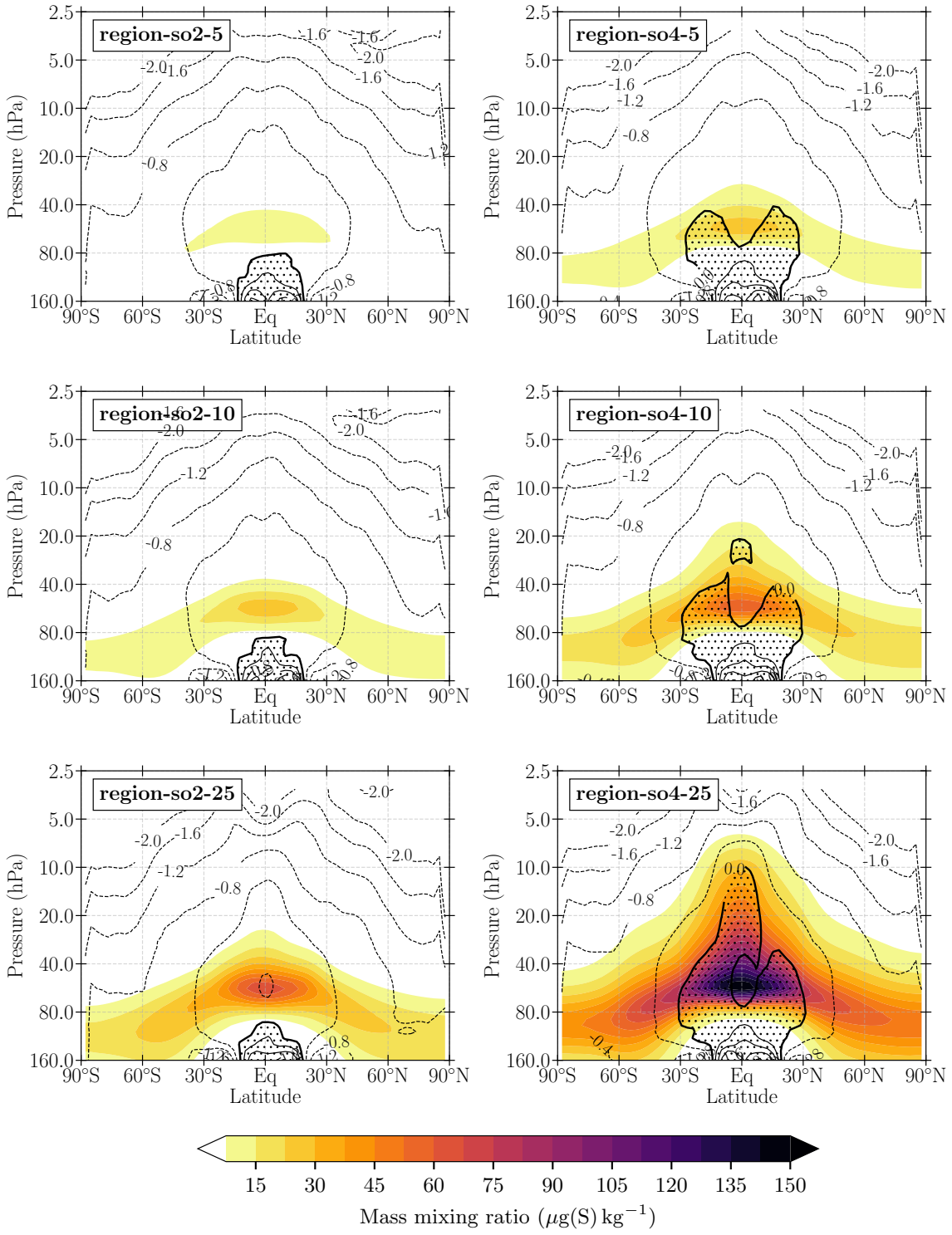

Figure A.14: Like Figure 5.10, but for the region injections.

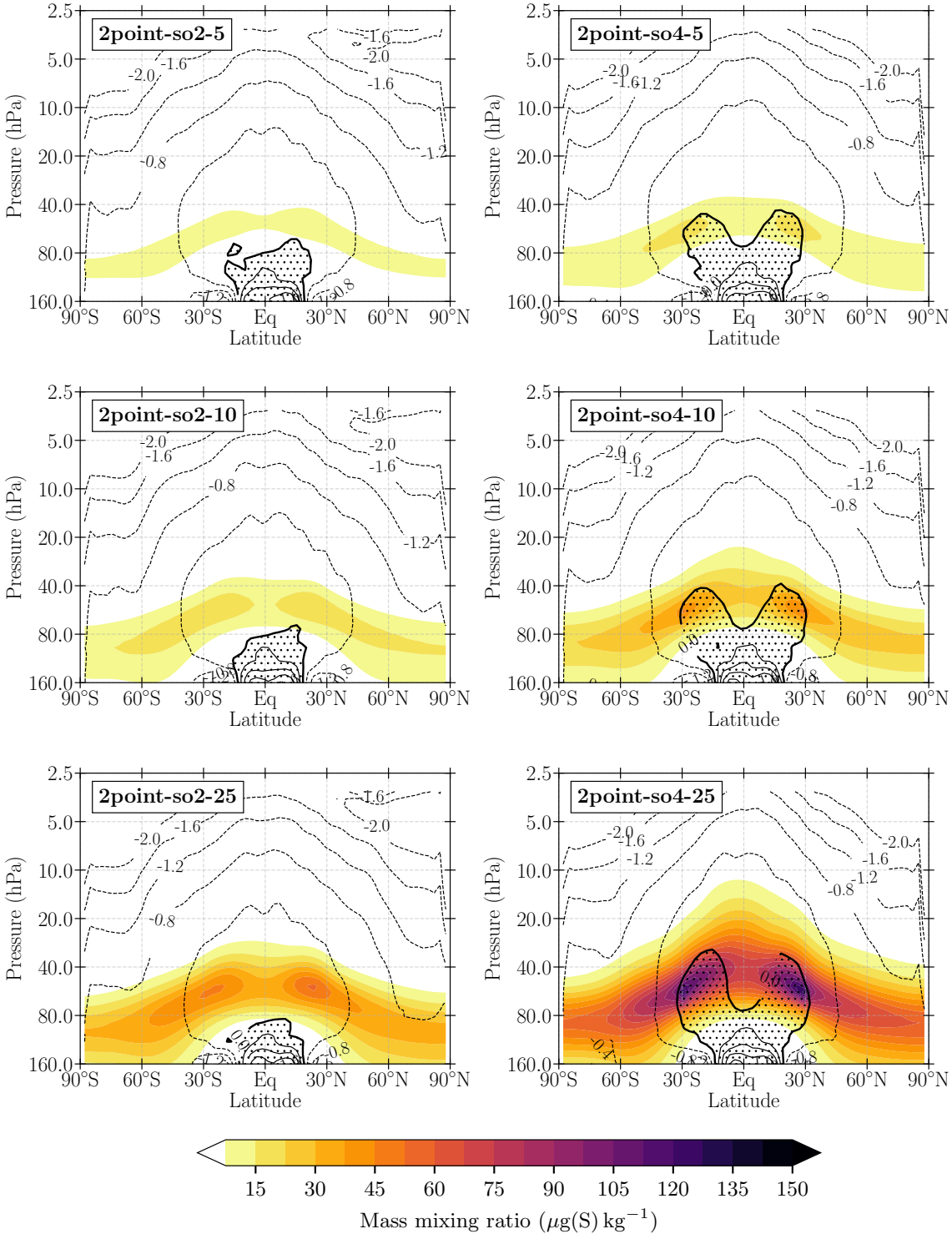

Figure A.15: Like Figure 5.10, but for the 2point injections.

Versicherung an Eides statt

Hiermit versichere ich an Eides statt, dass ich die vorliegende Arbeit im Studiengang M. Sc. Meteorologie selbstständig verfasst und keine anderen als die angegebenen Hilfsmittel – insbesondere keine im Quellenverzeichnis nicht benannten Internet-Quellen – benutzt habe. Alle Stellen, die wörtlich oder sinngemäß aus Veröffentlichungen entnommen wurden, sind als solche kenntlich gemacht. Ich versichere weiterhin, dass ich die Arbeit vorher nicht in einem anderen Prüfungsverfahren eingereicht habe und die eingereichte schriftliche Fassung der auf dem elektronischen Speichermedium entspricht.
Weiterhin stimme ich einer Ausstellung dieser Arbeit in der Fachbibliothek ausdrücklich zu.

Ort, Datum Name